

**DATA PROCESSING AND ESTIMATION TECHNIQUES
FOR UNCERTAINTY MINIMIZATION IN DYNAMIC
COMPRESSION EXPERIMENTS**

By

AMIT RAV

ENGG01201004025

Bhabha Atomic Research Center,

Mumbai – 400 085,

INDIA

*A thesis submitted to the
Board of Studies in Engineering Sciences*

*In partial fulfillment of requirements
for the Degree of*

DOCTOR OF PHILOSOPHY

of

HOMI BHABHA NATIONAL INSTITUTE



December, 2017

Homi Bhabha National Institute

Recommendations of the Viva Voce Committee

As members of the Viva Voce Committee, we certify that we have read the dissertation prepared by Amit Rav entitled "Data Processing and Estimation Techniques for Uncertainty Minimization in Dynamic Compression Experiments" and recommend that it may be accepted as fulfilling the thesis requirement for the award of Degree of Doctor of Philosophy.

Chairman – Prof. S. Mukhopadhyay



Date: 12/4/19

Guide / Convener – Prof. K. D. Joshi



Date: 12/4/19

Examiner – Prof. Rajan Jha



Date: 12/4/19

Member 1- Prof. Anita Topkar



Date: 12/4/19

Member 2- Prof. Namita Maiti



Date: 12-4-19

Member 3- Prof. S. R. Shimjith



Date: 12.4.19

Final approval and acceptance of this thesis is contingent upon the candidate's submission of the final copies of the thesis to HBNI.

I/We hereby certify that I/we have read this thesis prepared under my/our direction and recommend that it may be accepted as fulfilling the thesis requirement.

Date: 12/4/19

Place: Mumbai



Guide

STATEMENT BY AUTHOR

This dissertation has been submitted in partial fulfillment of requirements for an advanced degree at Homi Bhabha National Institute (HBNI) and is deposited in the Library to be made available to borrowers under rules of the HBNI.

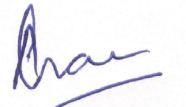
Brief quotations from this dissertation are allowable without special permission, provided that accurate acknowledgement of source is made. Requests for permission for extended quotation from or reproduction of this manuscript in whole or in part may be granted by the Competent Authority of HBNI when in his or her judgment the proposed use of the material is in the interests of scholarship. In all other instances, however, permission must be obtained from the author.



Amit Rav

DECLARATION

I, hereby declare that the investigation presented in the thesis has been carried out by me. The work is original and has not been submitted earlier as a whole or in part for a degree / diploma at this or any other Institution / University.



Amit Rav

List of Publications arising from the thesis

Journal

1. "Velocity interferometer signal se-noising using modified Wiener filter", Amit Rav, K.D. Joshi, Kallol Roy and T.C. Kaushik, *Meas. Sci. Technol.*, **2017**, 28(5).
<https://doi.org/10.1088/1361-6501/aa5d49>.
2. "Characterization of a signal recording system for accurate velocity estimation using VISAR", Amit Rav, K. D. Joshi, Kulbhusan Singh and T. C. Kaushik, *Meas. Sci. Technol.*, **2018**, 29(2).
<https://doi.org/10.1088/1361-6501/aa9cd4>

Conferences

1. "Time resolved radiation pyrometer for transient temperature measurement," A. S. Rav, A. K. Saxena, K. D. Joshi, T. C. Kaushik, and S. C. Gupta, *AIP Conf. Proc.*, **2011**, 1349, 451
2. "Simulation, modeling & verification of velocity interferometer in high strain rate experiments", Amit Rav, Amit Sur, Gaurav Pandey, K.D. Joshi, Satish C Gupta and Kallol Roy, *Annual IEEE India Conference (INDICON)*, **2014**, 10.1109/INDICON.2014.7030434



Amit Rav

I dedicate this thesis to my parents
Late Shri. Suraj Narayan Rav & Late Smt. Sona Devi

ACKNOWLEDGEMENTS

I express my deep sense of gratitude to my guide Dr. K.D. Joshi, for his keen interest, invaluable guidance and constant encouragement. I owe him a lot for imparting the knowledge of shock physics and experimental methods for determination of various shock parameters. I would like to thank Dr. Manmohan Bhatia, Dr. Kallol Roy and Dr. D. N. Badodkar for their support and encouragement during the tenure of my work.

Mere words are grossly insufficient to convey my profound gratitude to Dr. S. Mukhopadhyay, Dr. Anoop Bharacharjee and Dr. A.P. Tiwari, who has provided an expert advice and moral support throughout this work. Special thanks to the members of my doctoral committee Dr. Anita Topkar, Dr. Namita Maiti and Dr. S. R. Shimjith, for their critical comments and suggestions.

I am also indebted to Dr. T.C. Kaushik for encouraging me to pursue the work with dedication. My special thanks to my colleagues and friends, Dr. Alok Saxena, Mr. Gaurav Pandey, Mr. Amit Sur, Mr. S.P. Nayak, Mr. R.K. Mittal and Mr. M. Kalra for their valuable discussions and support. My special thanks to Mr. P.C. Das, Mr. A.B. Kalsarpe, Mrs. Archana Pundhir, Mr. Kulbhushan Singh, Mr. S.S. Wakode and Mr. L.P. Nemade, who provided necessary technical help for carrying out the experimental work.

Finally, a special recognition goes to all my family members especially to my wife (Mrs. Preeti Rav), children (Ms. Kanak Rav & Mast. Aayansh Rav), parents in-law (Smt Kanchan and Late Shri Ramkishan) and brothers (Shri Arun Rav & Shri Anup Rav) for their support, encouragement and patience during the tenure of this work.

CONTENTS

	Page No.
ABSTRACT	VII
LIST OF FIGURE	IX
LIST OF TABLE	XV
LIST OF ABBRIVATIONS	XVII
LIST OF SYMBOLS	XIX
Chapter 1: Introduction	
1.1 Motivation.....	1
1.2 Preface.....	3
1.3 Basics of Shock Waves.....	5
1.4 Dynamic Compression Generation Techniques.....	7
1.4.1 Explosives.....	8
1.4.2 Powder Gun/Propellant Gun.....	9
1.4.3 Two Stage Light Gas Gun.....	9
1.4.4 Single Stage Compressed Gas Gun.....	10
1.4.5 Electromagnetic Accelerators.....	11
1.4.6 High Power Lasers.....	13
1.5 Shock Diagnostic.....	15
1.5.1 Contact Type Measurement Techniques.....	15
1.5.1.1 Shock Arrival Sensors.....	15
1.5.1.2 Stress Sensors.....	17
1.5.2 Non Contact Type Measurement Techniques.....	18
1.5.2.1 Laser Velocity Interferometers.....	19

1.5.2.2 Radiation Pyrometer.....	22
1.5.3 Special Measurement Techniques.....	23
1.6 Requirement of Measurement System.....	23
1.7 Thesis Layout.....	25
 Chapter 2: Literature Survey	
2.1 Introduction.....	29
2.2 Radiation Pyrometer (RP) for Time Resolved Measurement of Transient Temperature.....	30
2.3 Characterization of Signal Recording System for VISAR.....	35
2.4 Signal De-noising specific to VISAR.....	38
2.5 Development of VISAR Model and Inverse Filtering.....	41
 Chapter 3: Development of Radiation Pyrometer (RP) and its Parameter Estimation	
3.1 Introduction.....	45
3.2 Theory of Radiation Temperature Measurement.....	47
3.3 Theory of Shock Temperature.....	48
3.4 Instrument Design for RP.....	50
3.4.1 Radiation Collection from the Target.....	51
3.4.2 Distribution of Light in Different Channels.....	52
3.4.3 Wavelength Selection.....	52
3.4.4 Detection of Radiation Intensity.....	53
3.4.5 Recording of Data.....	53
3.5 Calibration of RP Instrument.....	54
3.6 Development of Code for Estimation of Temperature and Emissivity.....	55
3.6.1 Theory of Least Square Method for Parameter Estimation.....	56

3.6.2	The Levenberg-Marquardt Method.....	61
3.6.3	Code Development.....	62
3.6.4	Uncertainty Calculation.....	65
3.7	Experimental Validation.....	66
3.7.1	Validation using Standard Radiation Source.....	66
3.7.2	Time Resolved Temperature Measurement of Electrically Exploding Wire.....	67
3.8	Summary.....	71

**Chapter 4: Characterization of Signal Recording System
used in VISAR**

4.1	Introduction.....	73
4.2	VISAR and its Signal Recording System	74
4.3	VISAR Output and Effect of SRS on Output Signal.....	76
4.4	Experimental Setup and Measurement.....	81
4.4.1	Experimental setup.....	81
4.4.2	Parameter Measurement.....	83
4.5	Data Analysis and Results.....	85
4.5.1	Range of Operation Selection.....	85
4.5.2	Signal Quality Measurement.....	88
4.6	Summary and Conclusions.....	91

**Chapter 5: Development of Modified Wiener Filter based
Signal De-Noising Method for VISAR**

5.1	Introduction.....	95
5.2	Experimental Setup and Data Selection.....	96
5.2.1	Experimental Setup.....	96

5.2.2	Data Selection.....	97
5.3	Requirements of Signal De-noising and Available Methods.....	99
5.3.1	Spectral Subtraction Method	101
5.3.2	Wiener Filter.....	103
5.3.3	Modified Filter Design	105
5.4	Filter Implementation.....	107
5.5	Filter Characterization.....	109
5.5.1	Optimization of Scaling Factor.....	109
5.5.2	Effect of Noise Floor Variation.....	110
5.5.3	Comparison of Proposed Filter with other Commonly Used Filters.....	113
5.5.4	Experimental Signal De-noising.....	114
5.5.5	Improvement in Velocity Measurement.....	116
5.6	Summary.....	117

**Chapter 6: Characterization of VISAR Using LTI Model
and Inverse Solution for Two Delay System**

6.1	Introduction.....	121
6.2	VISAR and its Governing Equations.....	122
6.2.1	Instrument Description.....	122
6.2.2	Governing Equations.....	123
6.3	Linear System: Properties and Solution.....	125
6.3.1	General LTI system and Convolution Sum as Solution.....	125
6.3.2	VISAR as LTI System and its Characteristic.....	127
6.4	Validation of Developed Model.....	130
6.4.1	Flow of Data and Expected Signal.....	130
6.4.2	Experimental Setup for Validating Model with Experimental Data.....	134

6.4.3	Comparison of Simulated and Experimentally Recorded Fringe Pattern	134
6.5	Discussion on VISAR Characteristic.....	137
6.5.1	Different Modes of VISAR Operation.....	138
6.6	Inverse Problem Definition.....	140
6.6.1	Introduction to Inverse Problem.....	143
6.7	Modified Wiener Inverse Filter.....	147
6.7.1	Implementation of Modified Inverse Filter.....	150
6.7.2	Two Delay VISAR Simulation.....	152
6.8	Summary.....	154
Chapter 7:	Summary and Future Scope	157
Appendix A:	Relation between Target Free Surface Velocity and Fringe Count	161
References:		163

ABSTRACT

The examination of material behavior, e.g. phase transitions, melting, vaporization and simple mechanical failures, under rapid loading conditions has been proved to be useful in basic as well as applied science. For example, the tensile fracture strength and yield strength of materials measured under rapid loading conditions plays key role in generating data required for selection and design of materials for a particular application involving high strain rates. Rapid loadings generate shock waves in materials, which eventually produce high transient compressions followed by rapid expansion in materials.

The extremely small time scales of a few nanoseconds to few microseconds involved in shock loading experiments require fast diagnostic techniques for characterization of the material state during compression and expansion. The measurement setup for such experiments requires adequate instrument hardware along with fast data recording system, and efficient signal processing and estimation techniques for extracting meaningful information from the experiment. The major source of uncertainty in the measurement of a physical parameter in these experiments is associated with the instrument design, method of data processing and estimation techniques used. Therefore, the minimization of uncertainty which implies achieving accurate and precise estimate of the physical parameter is not a single step process. It requires optimization at each step starting from instrument design and signal processing to estimation techniques.

This thesis presents, the Signal Recording Systems (SRS), signal processing software and estimation techniques developed for determination of transient temperature rise (caused during shock loading of materials or electrical explosion of metallic wires) employing Radiation Pyrometer (RP) and free surface/particle velocity history using Velocity Interferometer System for Any Reflector (VISAR). As far as the determination of transient temperature is concerned, the uncertainty of as low as ~5% has been obtained in estimating

temperature during experiments. For VISAR, to improve the SNR of the interference signals recorded during shock compression experiments and to identify the linear range of operation of SRS, a procedure has been developed for optimization of SRS with respect to parameters such as aperture opening, laser power and PMT supply voltage. The SRS, so optimized provides good SNR ($>20\text{dB}$) and linearity (within $\sim 5\%$).

Further, for de-noising of the recorded VISAR signals, a Wiener filter based adaptive de-noising algorithm capable of predicting and removing the additive noise present in the signal has been developed. This algorithm estimates the signal power spectrum and noise power spectrum using spectral subtraction method and utilizes the power of Wiener least square theory to remove the noise based on the SNR of the signal. The implementation of the developed filter on the recorded experimental signal has improved the SNR up to $\sim 15\text{dB}$ ($\sim 80\%$ increase) causing an improvement in the accuracy of determined free surface velocity from 2.10% to 0.52% and from 6.25% to 1.00% , in two different experiments.

Additionally, to characterize the VISAR and overcome its shortcoming, a Linear Time Invariant (LTI) model has been developed for it. This model has been studied in frequency as well as time domain and verified with one of the experimental data. A novel method of data handling has also been proposed to solve the inverse problem of estimating free surface/particle velocity using two delay VISAR. It may be noted that the two delay VISAR technique becomes useful when the rise time of the particle/free surface velocity becomes smaller than the delay time of the instrument.

LIST OF FIGURES

1.1	A snapshot of shock front propagating through material with velocity U_s . The parameters with subscript '0' correspond to the unshocked region whereas parameters with subscript '1' correspond to shocked region	5
1.2	Hugoniot representation in P-V Plane.....	6
1.3	Relative position of Hugoniot with other thermodynamic curves.....	7
1.4	Explosive lens, formed by a combination of two explosives.....	8
1.5	Schematic of Two Stage Light Gas Gun System.....	9
1.6	Photograph of Single Stage Compressed Light Gas Gun.....	10
1.7	Shock Arrival Sensors (a) Electrical sensor; (b) Optical Sensor.....	16
2.1	Schematic of radiation pyrometer developed by Boslough <i>et.al.</i> [9].....	32
2.2	Schematic of radiation pyrometer as described by Holmes <i>et.al.</i> [10].....	33
2.3	Schematic of radiation pyrometer developed by Gupta <i>et.al.</i> [11].....	34
2.4	Schematic of VISAR velocity interferometer as described by Barker & Hohenbach [73].....	42
3.1	The Electromagnetic Spectrum.....	47
3.2	The Spectral densities at different temperatures.....	48
3.3	Photograph of RP Instrument.....	50
3.4	Schematic diagram of the RP.....	51
3.5	Light collection system of RP.....	52
3.6(a)	Logical Flow chart of the developed code.....	63
3.6(b)	Steps as pseudo code for estimating parameters.....	64
3.7	Plot of spectral radiance measured with the best fitting gray body curve corresponding to $T=3009K$	67

3.8	Experimental setup for exploding wire.....	68
3.9	The estimated temperature profile of the exploding copper wire along with the measured current during first experiment.....	69
3.10	The estimated temperature profile of the exploding copper wire along with the measured current during second experiment.....	70
4.1(a)	Schematic of Velocity Interferometer.....	75
4.1(b)	Photograph of Signal Recording System.....	76
4.2	(a) Measured signal without fringes; (b) Histogram of selected data with Gaussian distribution; (c) Q-Q plot of measured data samples with samples from standard Gaussian distribution; (d) Autocorrelation of selected data.....	77
4.3	(a) Quadrature Fringe; (b) Estimated Velocity in m/s	80
4.4	Measurement Setup for characterization of signal recording system.....	81
4.5	Measured mean output voltage with respect to input laser power at different CV setting of PMT.....	86
4.6	Gain Variation with respect to CV for three optical input powers.....	88
4.7	SNR Measurement with respect to Input Laser Power at different CV settings.....	89
4.8	SNR Measurement with respect to aperture opening at different Input Laser Power.....	90
4.9	Rise Time and Fall Time variation with respect to Control Voltage.....	91
4.10	Improved signal record after applying present studies.....	93
5.1	Typical Plate Impact Experimental Setup.....	96
5.2	Typical recorded signal of VISAR with data identification.....	98
5.3	Wrapped and Unwrapped Phases (a) Clean Signal (b) Noisy Signal with false phase jump due to noise.....	100

5.4	Block diagram of Spectral Subtraction Method.....	101
5.5	A block diagram representation of Wiener Filter.....	104
5.6	Block diagram representation proposed de-noising tool.....	106
5.7	Variation in RMSE value for SSM only for scaling factor from 1 to 10 and noise floor of 10% and 0.5% (a) Bump Signal (b) Doppler Signal.....	109
5.8	RMSE variation with respect to noise floor (a) Bump signal (b) Doppler Signal.....	111
5.9	Standard Bump Signal (a) Original Signal along with 0 dB SNR (b-e) Noisy signal having 0dB SNR along with de-noised signal using SSM with noise floor values as 10%, 2%, 1% and 0.5% respectively, (f-i) Noisy signal having 0dB SNR along with de-noised signal using SSM+WF with noise floor values as 10%, 2%, 1% and 0.5% respectively	111
5.10	RMSE variation with respect to SNR for different de-noising methods using input as (a) Doppler Signal, (b) Bump Signal.....	113
5.11	Noisy and De-noised experimental signal using SSM+WF with $\alpha = 4$ and $\beta = 0.5\%$ (a) Test 1 and (b) Test 2; For both test signals each sample number corresponds to 0.2 ns real time.....	115
5.12	Original noisy and filtered quadrature fringes for (a) Test 1, (b) Test 2.....	116
5.13	Estimated Velocity profiles using original noisy signal (Red trace) and filtered signal (Blue trace) using proposed filter (SSM+WF) along with measured peak velocity for (a) Test 1, (b) Test 2.....	117
6.1	Schematic of VISAR with experimental setup.....	122
6.2	Black box representation of Linear System.....	126
6.3	Frequency and Phase plot of VISAR Linear Model.....	129

6.4	Steps used in Model Validation.....	131
6.5	(a) Numerically generated velocity data with constant acceleration and deceleration. (b) Displacement history corresponding to generated velocity data, (c) Generated phase profile using Linear Model of the VISAR, (d) Phase information wrapped in periodic $0-2\pi$ sinusoidal fringe pattern, (e) Estimated velocity from the generated fringe pattern using VISAR approximation.....	132
6.6(a)	Signal 1: Numerically simulated displacement history; Signal 2: Twice the Signal 1[2*Signal 1]; Signal 3: Numerically simulated displacement history, independent of Signal 1; Signal 4: Addition of Signal 1 and Signal 3 [Signal 1 + Signal 3].....	133
6.6(b)	Output 1 to Output 4 are phase output of the model corresponding to displacement history from Signal 1 to Signal 4.....	133
6.7(a)	Experimental as well as Simulated Fringe pattern.....	136
6.7(b)	Cross correlation between Experiment and simulated fringe pattern.....	136
6.7(c)	Frequency Spectrum of both signals (Experiment and Simulated).....	136
6.7(d)	Mean Square Coherence between Frequency Spectrum of both signals (Experiment and Simulated).....	136
6.8	(a) Model generated fringe pattern for two different delays; (b) Frequency content of the fringes	137
6.9	Comparison of the spectrum response of VISAR for different delay ' τ '.....	138
6.10(a)	Short Delay Mode, i.e. VISAR instrument delay \ll Rise time of the velocity of target free surface.....	139

6.10(b)	Long Delay Mode, i.e. VISAR instrument delay \gg Rise time of the velocity of target free surface.....	139
6.11	Effect of Instrument delay on measurement.....	141
6.12	Proposed schematic to overcome Instrument Response.....	142
6.13	System Response of two delay VISAR system.....	143
6.14	Inverse problem definition.....	144
6.15	Measurement system with input $x(n)$, system function $h(n)$, additive measurement noise $d(n)$ and measured output with error $y(n)$	148
6.16	Proposed scheme for calculating inverse system response.....	151
6.17	Root Mean Square Error presented for the comparison of the performance of three de-convolution method namely, Modified Inverse WF, Standard Wiener de-convolution and standard de-convolution applied after de-noising using the WF filter.....	152
6.18(a)	Steps for generating simulated VISAR response.....	153
6.18(b)	Signal Processing steps for de-convolution.....	154
6.19	Comparison of estimated velocities using VISAR approximation method using one short delay and two long delay. Also presented is the estimated velocity using modified inverse WF by combining two long delay data along with input velocity signal.....	155

LIST OF TABLES

3.1	Calibration Values for Four Channels of RP using Calibrated QTH Lamp.....	55
3.2	Calculated Error or uncertainty in the static temperature estimation.....	67
4.1	Specification of PMT.....	82
5.1	Percentage Variation in RMSE Value for Noise Floor Variation from 10% to 0.5%.....	110
5.2	RMSE Values for 0 dB SNR at Different Noise Floor from SSM And SSM+WF Methods. Also listed are the % differences in the same for the two methods.....	112
5.3	SNR Improvement for the signals recorded in dynamic compression experiments.....	114
5.4	Uncertainty improvement in free surface velocity estimation.....	117

LIST OF ABBREVIATIONS

AWGN	Additive White Gaussian Noise
CV	Control Voltage
DAC	Diamond Anvil Cell
DFT	Discrete Fourier Transform
DSO	Digital Storage Oscilloscope
EM	Electro-Magnetics
EOS	Equation of State
FPI	Fabry-Perot Interferometer
FPV	Fabry-Perot Velocimeter
FWHM	Full Width Half Maximum
HEL	Hugoniot Elastic Limit
IDFT	Inverse Discrete Fourier Transform
LTI	Linear Time Invariant
MHD	Molecular Hydro-Dynamics
MSE	Mean Square Error
NA	Numerical Aperture
NIST	National Institute of Standards and Technology
ORVIS	Optically Recording Velocity Interferometer System
PDV	Photon Doppler Velocimeter
PDVF	Polyvinylidene Fluoride
PMT	Photon Multiplier Tube
QTH	Quartz Tungsten Halogen

RMSE	Root Mean Square Error
RP	Radiation Pyrometer
RTD	Resistance Temperature Detector
SNR	Signal to Noise Ratio
SRS	Signal Recording System
SSM	Spectral Subtraction Method
SSM+WF	Modified Wiener Filter (Reinforced WF with SSM)
SVD	Singular Value Decomposition
THLS	Tungsten Halogen Light Source
VISAR	Velocity Interferometer System for Any Reflector
WAMI	Wide Angle Michelson Interferometer
WF	Wiener Filter
WIF	Wiener Inverse Filter

LIST OF SYMBOLS

$\%NL_{lf}$	Percentage Non-linearity using linear fit
ρ	Density
$(.)^*$	Complex conjugate of a function
$\overline{ D_k(f) ^b}$	Time averaged spectrum of noise for K segments
$\frac{\partial}{\partial \epsilon}$	Partial derivative with respect to emissivity
$\frac{\partial}{\partial T}$	Partial derivative with respect to Temperature
c_0	Speed of Light
$C_{xy}(f)$	Spectral coherence of two signals
r_{xy}	Correlation of two signals
T_d	Delay between input and output of the LTI Model
ΔV_m	Uncertainty in Measured Voltage
$\Delta \lambda_i$	Uncertainty in Wavelength of i^{th} Channel
ω_0	Radian frequency of the laser source
A_x	Time varying amplitude of first quadrature signal
A_y	Time varying amplitude of second quadrature signal
C_0	Fringe contrast
C_1	First Radiation Constant ($1.191 \times 10^{-16} \text{ Wm}^2 \text{ sr}^{-1}$)
C_2	Second Radiation Constant(0.01439 m. K)
C_p	Specific Heat at constant pressure

C_v	Specific Heat at constant volume
E_{TR}	Phase Transition Energy
$H_{WF}(f)$	System Transfer function of Modified Wiener Filter in frequency domain
$I^0(\lambda_i)$	Functional Value of Spectral Radiance at i^{th} channel
$N_F(t)$	Number of Fractional Fringes
$N_I(t)$	Number of Integral Fringes
P_0	Initial Pressure
P_1	Final Pressure
$P_D(f)$	Power Spectrum of signal $d(n)$
P_H	Hugoniot Pressure
P_S	Pressure Corresponding to Isentropic Compression
$P_X(f)$	Power Spectrum of signal $x(n)$
$P_Y(f)$	Power Spectrum of signal $y(n)$
$P_{xy}(f)$	Cross power spectral density of signal x and y .
R_L	Load Resistance
T_0	Room Temperature
T_H	Hugoniot Temperature
T_S	Isentropic Compression Temperature
T_{cs}	Temperature of Calibration Source
T_i	Initial Temperature

U_s	Shock Velocity
V_{cal}	Measured Voltage at the time of calibration
V_m	Measured Voltage
V_x	First Quadrature Signal of VISAR
V_y	Second Quadrature Signal of VISAR
$\hat{X}(f)$	DFT of estimate of the system input signal
Z_j	Derivative Matrix of j^{th} step of iteration
$f_g(x)$	Output of SRS at laser power x and gain g
$f_g^{lf}(x)$	Result of linear fit data at laser power x and gain g
u_p	Particle Velocity
x_0	Offset of first quadrature signal
y_0	Offset of second quadrature signal
λ_i	Wavelength of i^{th} Channel
χ_j^2	Summation of square of Difference Matrix D for j^{th} step of iteration
$\emptyset(t)$	Phase of the reflected laser source
ΔT_{cs}	Uncertainty in Temperature of Calibration Source
ΔT_m	Uncertainty in measured Temperature
ΔV_{cal}	Uncertainty in Measured Voltage at the time of calibration
$\Delta \varepsilon_m$	Uncertainty in measured Emissivity
ΔA	Update Vector for Temperature and Emissivity

ΔI	Uncertainty in spectral radiance
$h(n)$	Digitized system response of LTI model
l	Time lag during correlation of two signal
Γ	Grunesien Parameter
$\Phi(t)$	Phase of the signal output from interferometer
A	Atomic Number
C	Sound Velocity
D	Difference Matrix of functional value and measured values
$D(f)$	DFT of stationary additive noise signal
ε	Specific Internal Energy
$F(t)$	Total fringe count
$H(f)$	System Transfer function in frequency domain
I	Laser Intensity (W/cm^2)
$I(\lambda_i)$	Measured Value of Spectral Radiance at i^{th} channel
$I(\lambda)$	Spectral Radiance ($Wm^{-2}sr^{-1}$)
S	Entropy
$SNR(f)$	Spectrum of signal to noise ratio
T	Temperature
V	Specific Volume
$X(f)$	DFT of system input signal without noise
$Y(f)$	DFT of system output signal with noise

Z	Ionization Number
a	Scaling factor for amplitude of noise subtraction
b	Exponent of signal in frequency spectrum b=1: Magnitude Spectrum; b=2: Power Spectrum
$d(n)$ or $d(t)$	Digitized or continuous stationary additive noise signal
t	Time
$v(t)$	Velocity of moving target
$x(t)$	Position history of target; Input to VISAR Model
x	Laser power input to SRS
$x(n)$	Digitized system input signal without noise
$y(n)$	Digitized system output signal with noise
$y(t)$	System output
$\mathbb{E}[\]$	Estimation operator for a function
β	Noise floor parameter
δT	Update step for Temperature
$\delta \varepsilon$	Update step for Emissivity
ε	Emissivity
ζ	Scaling Parameter of Levenberg-Marquardt method
λ	Wavelength
μ	Mean of measurement
σ	Standard deviation of measurement

ϵ	Phase error in quadrature
e or $\{E\}$	Measurement error/model noise in system model
S_r	Sum of Square of residues/errors in system model

Chapter 1

Introduction

1.1 Motivation

A measurement is an experimental process to acquire new knowledge about a physical quantity. It can be defined as a set of interrelated or interacting operations that are used to determine or acquire knowledge about the physical quantity to be measured. These interrelated or interacting operations are instrument response (its linearity, repeatability, resolution, calibration etc.), method of data processing (data identification, sorting, denoising etc.) and estimation techniques. Measurement uncertainty/error is defined as the difference between the distorted information and the undistorted information about a measured physical quantity. The minimization of uncertainty/error requires optimization at each step starting from instrument design, signal processing to estimation employing different techniques. The present thesis deals with the development of measurement systems and processes required for characterization of material state under high dynamic compression such as shock loading. The characterization of material state under shock loading includes the determination shock equation of state (EOS) or Hugoniot, shock induced phase transformations (if any) and mechanical failure properties at high strain rates. The investigations of these properties require knowledge of five parameters particle velocity (u_p), shock velocity (U_s), pressure (P), density in compressed state (ρ) and internal energy (\mathcal{E}). The quantities commonly measured in the material under shock loading experiments are impact velocity, shock velocity, time resolved stress profile, temperature profile and free

surface/particle velocity profile. Out of these, the measurements of stress profile, temperature profile and free surface/particle velocity profile provide a continuous time resolved variation in these quantities, whereas, shock velocity and impact velocity are measured as average quantities. The techniques required to measure the time resolved shock induced temperature rise and free surface/particle velocity history are based on non contact methods i.e. the probe or sensor for these measurements are not in physical contact with the sample. However, the stress profile in the shocked material is measured using contact type method. Aim of the present thesis is to develop (i) instrumentation (**Radiation Pyrometer (RP)**) and estimation method for time resolved temperature measurements under shock loading; (ii) characterization of signal recording system (SRS) and signal processing methods to minimize uncertainties in free surface/particle velocity history measured employing interferometry technique such as **Velocity Interferometer System for Any Reflector (VISAR)** in shock loading experiments.

Technique of temperature measurement using **RP** already exists in literature [1, 2]. It requires emission spectrum of the heated body to be measured and compared against the equivalent black body spectrum at known temperature. The use of this technique in dynamic compression experiments dates back to 1963 [3-7] where thermistor, thermoelectric effect and PMT's have been used as sensing method. The critical requirement for a RP to be able to use in dynamic compression experiments is its response to fast changing (rise time of the order of ~3-5 ns) shock luminescence with the duration of ~ 5-10 μ s. Since its first use, the method of measurement shock luminescence has been modified by researcher as per their experimental configurations [8-10]. The RP for dynamic compression experiments is not a standard catalog product of any manufacturer; rather it has been developed, modified and redesigned by the users as per their requirement. Hence, considering the importance of RP [3-23] in determining thermal equation of state, partition of total energy in shocked system and

melting of materials under shock loading, its development has been carried out in our laboratory and it forms a part of the present thesis.

Another very important and useful measurement tool in dynamic compression experiments is VISAR. Depending upon the configuration of the experiment, it can be used to measure either free surface or particle velocity history of the target [24, 25]. This velocity history contains information about in-situ changes in target material behavior, *e.g.* elastic-plastic transition, phase transition, dynamic fracture (spall) strength along with strain rates [24-27], during shock loading and unloading. The first VISAR has been developed by L.M. Barker [27] in 1965. Since then, this instrument has gone through several modifications. This instrument being not available for export to India from international market, so it has been developed in our laboratory [28] few years back. Since then it is in continuous use as a diagnostic tool in shock wave experiments [28, 29, 30]. For accurate determination of free surface velocity history of target material using this instrument in shock wave experiment, the knowledge of various parameters such as the linearity of the SRS, signal to noise ratio (SNR) of recorded signal and the limitation of instrument is very important. In view of this, the characterization of VISAR system before use in particular experiment is essential. A part of this thesis deals with characterization of VISAR set up to minimize the measurement uncertainties.

1.2 Preface

The study of materials under dynamic compression capable producing extreme conditions of pressure and temperature has long been a topic of interest but it significantly marked its position in scientific literature during 1950-1960 with the advent of devices based on chemical and nuclear energies. Such studies are of interest not only in applied sciences but also in fundamental physics pertaining to understanding of the state of matter in astrophysical

bodies and interior of the earth. Many interesting phenomenon like phase transition, shock melting, metallization of insulators etc. are found to take place under extreme conditions of pressure and temperature in these experiments. Apart from this, the shock wave studies of materials provide information on equation of state over a wide thermodynamic range which serve as key input to various hydrodynamic codes used to simulate material behavior under rapid loading conditions.

In laboratory environment high pressures can be achieved by various experimental techniques. Based on the application of compression force and response of material, these schemes may be broadly categorized as static and dynamic. For generating static compressions in materials anvils of hard material such as diamond anvil cell (DAC) is commonly used. The process of compression using this device generates the pressure-strain data along isotherm. The pressures of order of ~ 750 GPa [31] have been achieved so far in materials using this technique. In contrast, the dynamic pressures are normally created by sudden deposition of high energy over small time durations. Considering the way of creating pulsed energy these methods may broadly be categorized as (i) Explosives (ii) Gas guns (iii) Electromagnetic launchers and (iv) Lasers and particle beams [32-34]. By suitably designing the experiment, one can not only generate intense shocks in the materials but also can produce the shock-less quasi-isentropic compressions [35]. The present thesis being focused on devising the tools for minimization of uncertainty in the measurement of parameters like shock temperature and free surface/particle velocity carried out during shock/dynamic compression studies, discussion will be limited to shock wave methods only and details about other techniques may be found in cited references.

1.3 Basics of Shock Waves

A shock wave is essentially a large amplitude disturbance propagating supersonically through a medium across which, the flow variables such as density (ρ), pressure (P), internal energy (E), particle velocity (u_p) etc. vary in a nearly discontinuous manner, clearly distinguishing between the shocked and unshocked region [36, 37]. Figure 1.1, represents the snapshot of shock front propagating in a material with shock velocity of U_s . This is in sharp contrast to subsonic sound waves, where all thermodynamic quantities vary continuously through the medium.

For a steady shock wave the conservation of mass, momentum and energy across the discontinuity can be written as a set of differential equations [36, 37], which lead directly to the Rankine-Hugoniot relationships between the specific volume V , the stress (shock pressure) P , the particle velocity u_p the shock velocity U_s and the specific internal energy \mathcal{E} :

$$\rho_0 U_s = \rho_1 (U_s - u_p) \quad (\text{Mass Conservation}) \quad (1.2)$$

$$P_1 - P_0 = \rho_0 U_s u_p \quad (\text{Momentum Conservation}) \quad (1.3)$$

$$\mathcal{E}_1 - \mathcal{E}_0 = \frac{1}{2} (P_1 + P_0) (V_0 - V_1) \quad (\text{Energy Conservation}) \quad (1.4)$$

The Rankine Hugoniot or simply Hugoniot is defined as the locus of all the equilibrium states reached from a given initial state in a series of experiments. Three

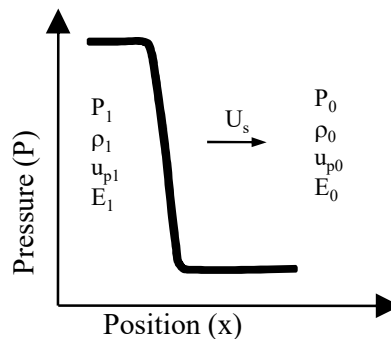


Figure 1.1: A snapshot of shock front propagating through material with velocity U_s . The parameters with subscript ‘0’ correspond to the unshocked region whereas parameters with subscript ‘1’ correspond to shocked region.

relationship of conservation equations are known as Hugoniot relations and are expressed as:

$$P = H(V, P_0, V_0) \quad (1.5)$$

The curves representing above relation in a two dimensional space are referred as “Rankine-Hugoniot” curves or only “Hugoniot”. It may be noted here that Eq. 1.5 represents a set of curves each starting at different value of initial state (P_0, V_0) . As above equations connect two states across a shock front, therefore Hugoniot is not a thermodynamic path, but it is the locus of all possible final states that can be achieved by the passage of a single steady shock, starting from the same initial state. Under shock compression material follows the path of a straight line joining the initial and final states and known as “Rayleigh line”. A typical Hugoniot curve along with Rayleigh line is shown in Fig.1.2. It is important to note that Hugoniot are not only limited to $P - V$ plane but are also represented in $P - u_p$ plane to directly predict the outcomes of planer impact experiments and wave interactions. As Hugoniot is a material property, in $P - u_p$ plane it can be reflected and translated according to direction of propagation of shock and initial particle velocity respectively.

To complete the discussion on Hugoniot, it is important to compare it with other thermodynamic curves. The relative positions of Hugoniot, isentrope and isotherm are shown in Fig.1.3. The area under the curve represents the change in internal energy of material under

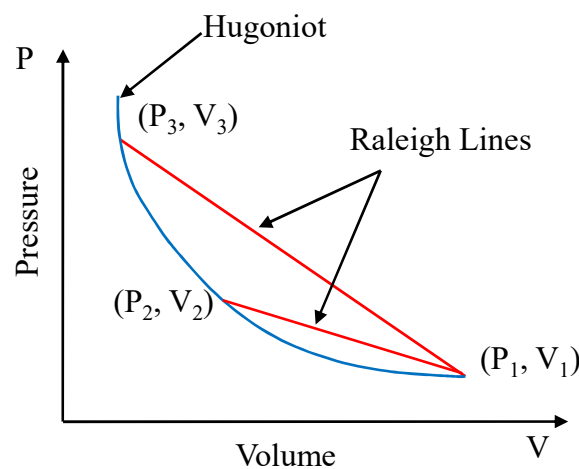


Figure 1.2: Hugoniot representation in P-V Plane

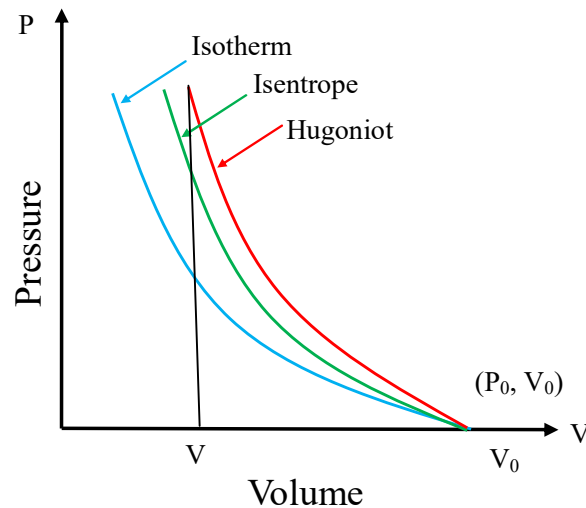


Figure 1.3: Relative position of Hugoniot with other thermodynamic curves.

compression. The total internal energy consists of cold energy (potential energy) due to columbic interactions as well as thermal energy due to vibrations of atoms and electronic excitations. As in isothermal process the increase in internal energy is only due to cold energy part in contrast to isentrope where the thermal parts also contribute, hence isentrope lies above the isotherm. The isentropic processes are reversible in nature but in Hugoniot energy also goes in plastic form leading to increase in entropy and temperature. The irreversible heating makes the Hugoniot to lie above the isentrope.

1.4 Dynamic Compression Generation Techniques

High dynamic pressures including shock loading can be achieved either by planar impact of a flyer plate or by direct deposition of pulsed energy in material under study. Following devices are commonly used for this purpose: (i) Explosives (chemical, nuclear, shaped charges etc.) (ii) Gas guns (single stage, double stage and compressed gas gun) (iii) Electromagnetic launchers (rail gun, coil gun, electric gun and Z-accelerator) and (iv) Lasers and particle beams. A brief description of these devices is presented below:

1.4.1 Explosives

As shock is an inherent property of explosives, these have long been used in shock research. The common experimental methodologies are either to keep explosive in contact or to use it for acceleration of a planar projectile. To induce a planar shock front in a material kept in its contact of an explosive plane wave shaper (lens) is used apart from main explosive pad. A typical experimental assembly using explosive based method for generating shock in material of interest is shown in Fig. 1.4. As displayed in figure, explosive lens consists of a cone of explosive of lower detonation velocity with another explosive of higher detonation velocity surrounding it. The cone angle is decided such that once initiated at top the detonation front reaches on flat surface simultaneously. Pressures up to 45 GPa [39, 40] in near triangular temporal profile, have been achieved by such lenses. To enhance the pressure up to few hundreds of GPa and to generate square shaped pressure pulses, instead of placing target plate in contact of the explosive pad it is kept at certain distance from the explosive pad and planar shock is induced in it by impact of a flyer plate accelerated by the explosive assembly. Flyer plate velocities of ~ 6 km/s have been achieved by this way [41]. A lot many approaches have been implemented to achieve much higher flyer velocities; in one such

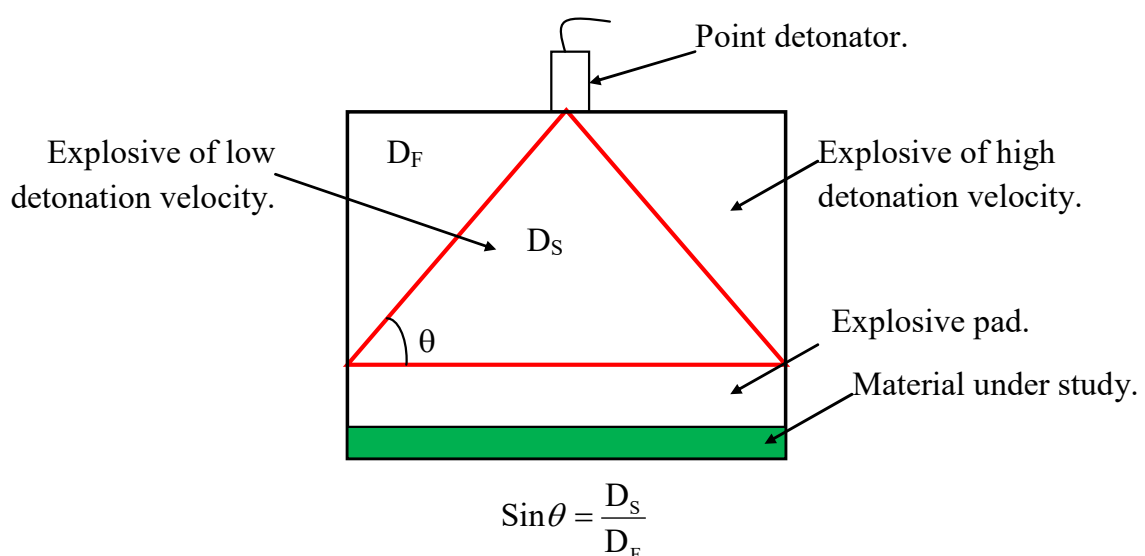


Figure 1.4: Explosive lens, formed by a combination of two explosives.

approach cascaded systems have been used to create overdriven shock fronts to achieve velocities more than 10 km/s [42]. The handlings of explosives require special facilities, therefore such technologies are limited to few laboratories only.

1.4.2 Powder Gun/ Propellant Gun:

The concept of propellant gun is conceived from military field guns and rocket launchers to accelerate a projectile by burning propellants behind it. The burning of propellant generates high pressure gases which accelerate the projectile in a barrel. As the energy supplied by the propellant is used not only in acceleration of projectile but also goes as kinetic energy of burnt gases, these guns can accelerate projectile to a velocity of around 2.3 km/s and are used for shock studies up to 100 GPa pressure [43].

1.4.3 Two Stage Light Gas Gun:

Due to heavy mass of burn gaseous products (~ 30 g/mole [43]), it is difficult to achieve higher velocities in powder guns. Another factor that affects the final velocity is the speed of sound, which decides the communication limit between the projectile and breach where pressure is generated, which is low for gases of high molecular weight. To overcome these issues a concept of two stage light gas gun is invoked. Schematic of two stage light gas

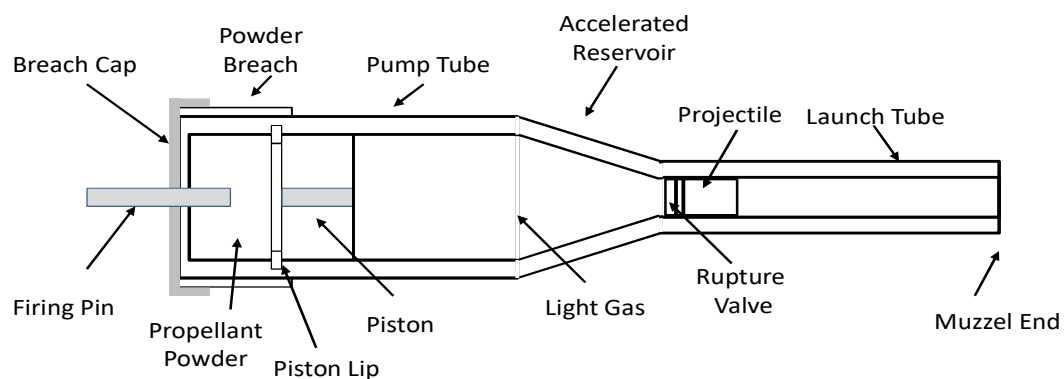


Figure 1.5: Schematic of Two Stage Light Gas Gun System

gun is presented in Fig. 1.5. Here in first stage a piston is accelerated by a powder gun, which dynamically compresses the light gas (helium or hydrogen), filled inside its barrel to high pressures. In the central region a valve sealed conical transition is provided between first stage and smaller diameter second stage barrel containing the projectile at its breech. As the piston compresses the gas a limit is reached when the valve between two stages ruptures and the gas rushes into the second stage barrel to accelerate the projectile. The front of the piston is made of a deformable plastic to still compress the gas till it stops in the conical region after significant deformation. Velocities up to 8 km/s have been achieved on 16-20 gm projectiles by compressing the hydrogen gas up to 0.7-1 GPa pressure [43]. To still enhance the projectile velocity, a third stage is augmented to isentropically launch titanium alloy disks up to 16 km/s [44].

1.4.4 Single Stage Compressed Gas Gun

This is another type of gun where instead of using propellants, gases like air or helium are compressed up to 300-400 bar and used to drive the projectile. Mechanical pumps are used for compression and a valve is ruptured to accelerate the projectile by sudden release of compressed gas. These guns are designed for shock compression studies at relatively low



Figure 1.6: Photograph of Single Stage Compressed Light Gas Gun

pressures (a few tens of GPa) without any stringent laboratory requirements. Velocities around 0.4 km/s and 1 km/s, respectively, can be achieved by using air and helium as driving gases [45]. Fig. 1.6 presents the photograph of the existing single stage light gas gun facility present in our lab.

1.4.5 Electromagnetic Accelerators

As the name implies this category of launchers utilizes electromagnetic forces to accelerate projectiles to very high velocities. In principle there is no theoretical limit for such launchers and recently a record velocity of 45 km/s [46] has been reported on 900 μm thick aluminum projectiles using magnetic forces at Sandia (Z- machine). Some of the devices flyer accelerators based on the electromagnetic forces are rail gun, electric gun and magnetic accelerators.

The rail gun consists of two parallel metal rails connected to a pulsed power source mostly a capacitor bank. The rails are electrically connected to each other by a movable armature followed by a non-conducting projectile. When the pulsed power source induces a large current in this arrangement, a Lorentz force acts over both rails as well as on armature. Rails are fixed but armature is free to move hence it accelerates over the rails to high velocities along with projectile. The major problem in rail gun is its poor energy efficiency (<50%), which is decided by residual energy stored in the magnetic flux associated with rails, resistive losses in rails-armature contacts, frictional losses at the projectile-rail contacts, and air drag forces. To improve its efficiency various modifications have been proposed, like projectile pre-launching [47], using plasma/ hybrid armatures [48], and distributed energy rail guns etc.[49]. But still the practically achievable flyer velocity is reported to be around 5-7 km/s [50] on a few gram projectiles. Considering the practical limitations, present research

interest now is shifted towards launching few kg projectiles to a velocity of 2-3 km/s for defense applications [51, 52].

The electric gun utilizes the electrical explosion of a thin metallic foil by fast current discharge to drive the projectile. The fast and high currents are generated by pulsed power capacitor banks. Due to rapid Joule heating, the energy density in thin foils may reach up to 20-30 kJ/gm, which is much higher than the explosive energy density. This leads to very high thermodynamic pressures, which are used to accelerate a thin dielectric projectile (flyer) placed in close vicinity of the exploding foil. The important aspects of electric gun system is its capability of accelerating flyers to high velocities for shock research up to 0.5 TPa [53] and its operational simplicity. Additionally only a small quantity of target material is required which make this technique suitable for shock studies on precious and toxic materials. Velocities up to 18 km/s are reported in literature on 43 mg Kapton flyer [54].

Conceptually the magnetic accelerator technique is similar to rail gun, where strong magnetic pressure is used to drive the flyers to high velocities, except the amplitude of current pulse is much higher and duration is much shorter. This technique requires fast pulse power sources like Z-machine [55] at Sandia, which can deliver a well shaped current pulse reaching up to 20 MA in 200 ns time in a short circuit load. The load consists of two closely spaced parallel metal plates having suitable size grooves in anode plate. When the large current passes through the load, field of several Mega-Gauss is generated in between the plates, resulting in 100's of GPa pressure over the anode plate. Due to such high pressures the thin portion of anode plate gets detached and moves inside the groove as a flyer. With accurate MHD simulations two requirements are fulfilled, one is to keep the stress uniform over the grooved anode plate by suitable load design and other is to achieve shockless loading by proper shaping of current pulse. These two conditions ensure that during loading the flyer remains planar without any significant temperature rise. Some portion of flyer plate still gets

ablated due to penetration of magnetic field with time leading to joule heating; therefore the usable portion of flyer is lesser than its initial thickness.

The main attractive feature of magnetically driven systems is their capability to launch flyers to very velocities which are not achievable in other schemes. In addition to impact studies these systems are also useful for quasi isentropic compression studies of materials up to hundreds GPa of pressures [56].

1.4.6 High Power Lasers

High power lasers play a significant role in shock research, they are used in various schemes like direct drive, indirect hohlraum drive and laser driven flyers to create extreme thermodynamic conditions in laboratory environment. In direct drive, a high energy laser pulse is focused on a solid target, which rapidly heats it up and generates expanding plasma in backward direction (laser direction). To conserve the momentum a forward moving shock is induced in the material and an analytical expression for the pressure may be written as [57]:

$$P(\text{kbar}) = 230.A^{7/16}.Z^{-9/16}.\lambda^{-1/4}.t^{-1/8}(I/10^{12})^{3/4} \quad (1.9)$$

Where ‘I’ is the laser intensity in W/cm^2 , ‘ λ ’ is its wavelength in μm , ‘t’ is the pulse duration in nanoseconds. ‘A’ and ‘Z’ are the atomic number and the ionization number of the target material respectively. The generated pressures may be enhanced by placing a transparent confining medium in front of the target material, which impedes the expansion of ablated plasma. However the energy deposited in the target is limited by the breakdown strength of transparent confining medium, which is governed by the properties of confining media, laser wavelength and pulse duration.

Though laser ablation methods may generate pressures in TPa regime [58], but accuracy of equation of state data is mainly restricted by the two major factors. One is the

non-uniformity of laser beam over the target surface leading to non-planar shock fronts and other is the preheating of the target before shock arrival by fast moving hot electrons or hard X-rays generated in expanding plasma. To overcome the non planarity issue indirect drive scheme are used [59]. In this scheme, the laser beams are focused inside a small cavity (known as hohlraum), through small holes, and its interaction with cavity walls leads to generation of thermal X-rays. These soft X-rays are used to produce shock waves in the target kept inside the cavity. These schemes are more popular in fusion research due to radiation summarization and reduced sensitivity to hydrodynamic instabilities [60, 61].

The other possible scheme to generate planar shock fronts is to accelerate flyer plates by laser energy deposition on a multilayer attached to a thin flyer-foil arrangement. Results reported on Trident laser facility [62] shows a typical flyer planarity of 3-10 mrad up to a flyer velocity of 7 km/s. Using indirect drive scheme, soft X-rays were also used to drive a flyer plate and to demonstrate the generation of planar shocks up to 0.75 Gbar [59]. Other than Hugoniot measurements laser with temporal ramp shaped pulses are also used to achieve quasi-isentropic compression [62]. To generate very high pressures and to achieve conditions for inertial confinement fusion various high energy laser facilities like Trident (LANL, USA), Argus (LLL, USA), UMI 35 (USSR), Delphin (USSR), Rutherford (UK), LiMeil (France), Osaka (Japan), Shiva (LLL), Nova (LLL), and NIF (LLNL, USA) are developed worldwide.

In addition to lasers the beams of electrons, protons or heavy ions are also used for shock generation. The advantages of particle beams over lasers are longer pulse duration; better homogeneity and absence of target preheat by fast electrons [63]. Moreover heavy ion beams can generate dense plasmas near to solid density which are useful for inertial confinement fusion research [64].

1.5 Shock Diagnostics

Diagnostic techniques play an important role in determining the physical parameters during dynamic compression experiments. The measurement uncertainty in the measured parameters depends upon the accuracy and precision of these diagnostic techniques. As duration of these experiments lies from few nanosecond to microsecond, therefore special sensing techniques are employed for measurement of parameters like pressure, particle velocity and pressure induced rise in temperature. These techniques can be broadly classified into two categories namely contact techniques and non contact techniques. Commonly measured parameters using contact techniques are impact velocity, shock velocity and stress profile, whereas the parameters measured using non contact techniques are free surface/particle velocity history and temperature profile.

1.5.1 Contact Type Measurement Techniques

Contact type measurement techniques involve physical contact between target material and the sensors. It requires special arrangements to be made in the target to fit these sensors. Quantities that can be measured using these sensors are impact velocity, shock velocity and pressure/stress profile. Sensors used for these measurements are shock arrival sensors (electrical and optical) and piezo-resistive gauges.

1.5.1.1 Shock Arrival Sensors

These types of sensors work on detection of shock wave arrival either by the movement of free surface, or by the ionization of compressed gas or by luminescence of shocked surfaces. The common types of sensors are electrical pins, ionization pins and fiber optic pins. The electrical pin consists of two coaxially insulated electrically charged metal electrodes. When a conducting moving surface touches the pin, the electrodes get discharged

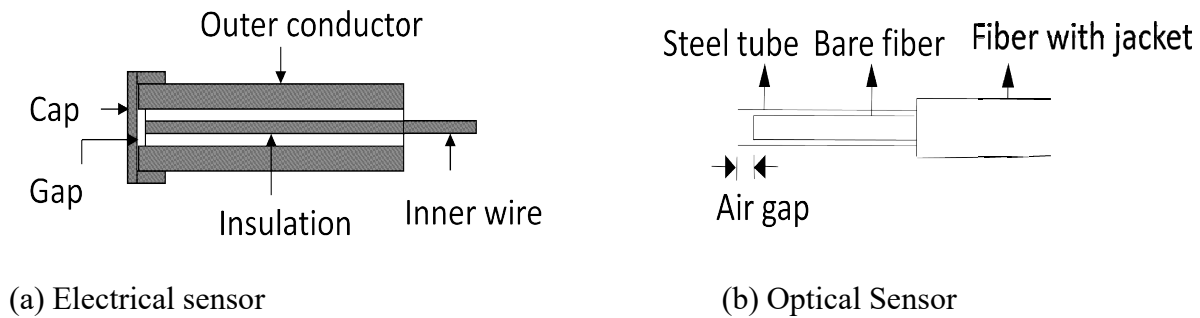


Figure 1.7: Shock Arrival Sensors

and current flows across a resistor placed in the charging circuit, which generates a voltage spike across it. The timing of voltage spikes for the pins placed at known distances is recorded on an oscilloscope and is used to determine the velocity of shock wave. More sophisticated form of electrical pins is self-shorting pins [65, 66] which can be used to detect the shock arrival time, even in the case when moving surface is not conducting one and shielding is required against pre-shortening by ionized gases moving ahead of the shocked surfaces. As displayed in Fig. 1.7(a), in self shorting pin, a metal cap is placed near the open ends of charged electrical pins at a very small gap ($\sim 50 \mu\text{m}$); on the arrival of shock the cap moves at the free surface velocity of its material and closes the gap. By placing these pins at different known depths of the target material one can determine the velocity of shock wave through target material.

In many applications where pulsed power sources are involved, the electrical pins become prone to electromagnetic noise. In such situations the use of optical fibers is quite helpful, as pins based on optical techniques do not require any electrical biasing or special electromagnetic shielding. In one type of such fiber optic pins [67], a micro balloon filled with argon gas is attached to one end of an optical fiber. When this micro-balloon interacts with the shock wave, a light flash is generated and gets recorded in the oscilloscope through a photo detector. This method is quite sensitive, fast and immune to EM interference but requires special techniques to manufacture the micro-balloons. In some probes [57 and the

references cited therein], quartz or high density glasses are also used, which generate high shock luminescence under compression. At high pressures, the arrival of shock wave also generates a weak luminescence due to ionization of air present in the vicinity of free surface. These weak optical signals may be measured using fast and sensitive photodiodes. Figure 1.7(b) shows schematic drawing of optical type shock arrival sensor.

1.5.1.2 Stress Sensors

Pressure is an important thermodynamic parameter when studying material behavior under compression or expansion [68]. The in-situ measurement of shock pressure in the target material in shock wave experiments is carried out using special shock sensors based on piezoresistive or piezoelectric properties. For measurement of stress profile in the target material, these sensors in the form of thin foils are normally embedded inside the target. The piezoresistive materials like Manganin, carbon, ytterbium, lithium are commonly used for stress measurements up to 100 GPa, whereas piezoelectric materials like X-cut quartz, lithium niobate and Poly vinylidene fluoride (PVDF) are used for measurements up to 25 GPa. Manganin, an alloy of copper (84%), manganese (12%) and nickel (4%) having reduced sensitivity of resistivity to temperature is the most widely used piezoresistive sensor since 1960's for stress profile measurement in shock wave experiment. The gauge elements are designed in various geometrical configurations from thin foils or wires of Manganin and embedded in the target material [69]. A constant current is fed to the gauge and temporal profile of voltage developed across it is measured during shock loading. The stress profile is computed using the well calibrated data of gauge resistivity with stress. In practical situations, when loading is not purely uniaxial, a strain gauge is also placed to compensate the strain effects [70]. Though these gauges are quite popular in shock community, but their

calibration at high pressures and estimation of gauge hysteresis is a difficult task. The other issue is the finite thickness of gauge element, which limits its response time.

For low pressure measurements piezoelectric sensors like x-cut quartz (~ 3 GPa) are quite common, these are either placed in contact with the target or impacted directly. Being a piezoelectric material, it generates a current when its two opposite surfaces are subjected to different stress levels. It is quite useful for low stress measurements because of its large signal output (10 V/GPa in 50 Ω), precise characterization and inherent fast response less than a ns. To make it work at higher pressures, a high impedance buffer material of known Hugoniot like tungsten carbide is placed in between the quartz and target surface [70]. In parallel to x-cut quartz, lithium niobate is also used for stress measurements up to 1.8 GPa.

The gauges based on PVDF have also gained lot of interest, as these are inexpensive and can measure stresses up to 35 GPa with nanosecond response time [71]. These gauges can also yield large signals with typical sensitivity of 23 pC/N. A lot of efforts have been made to develop PVDF films for shock applications so that gauges made by this material remain easily reproducible [72].

1.5.2 Non Contact Type Measurement Techniques

These are mainly optics based techniques and measure either reflected laser light from the target surface using velocity interferometers or shock luminescence/emission spectrum of the target employing RP. Advantage of these techniques is that they do not disturb the initial condition of the sample and mainly provide the complete history of the measurement. Brief discussion on these techniques is presented below.

1.5.2.1 Laser Velocity Interferometers

The inherent sensitivity, fast response and high accuracy of optical techniques make them very useful for shock diagnostics. With the advent of lasers, many interferometric methods have been developed to measure the velocity of fast moving surfaces. These methods are based on measuring the Doppler shift in the light reflected from a moving surface, which may be the projectile, target or both. As the response time of these methods may go less than a nanosecond, various phenomena such as, the phase transitions occurring at high pressures and spall fractures occurring under tension followed by compression, may only be detected by such techniques. Considering the vast variety of such interferometers, a brief overview covering some of them are given here and details may be found in cited references.

The first laser interferometer known as ‘Displacement interferometer’ was developed by Barker & Hollenbach [27] in 1965. In this system a Michelson interferometer was used to measure the Doppler shift in the light reflected from the moving surface, which acts as one of the mirrors of interferometer. The movement of surface causes fringe shift, which is detected by a photomultiplier tube and the fringe frequency is proportional to the displacement. Due to limited frequency response of existing detectors and recording systems, the practical velocity limit of this instrument was limited to 0.2 km/s [27]. To overcome such limitation, Barker & Hollenbach made a significant improvement and developed another system known as ‘velocity interferometer’ [73]. In this system the Doppler shifted light [74] is used as a source to Michelson interferometer with delay in one of the legs. Hence, both the interfering lights are now Doppler shifted but with different amount. Further, it may be noted that when surface is moving with constant velocity, both light beams have the same wavelength and their beat frequency is zero. Now with this modification, the number of fringes shifted becomes proportional to the specimen velocity and not to its displacement. The limitation of

this instrument is that it requires the mirror like reflecting surface which gets destroyed when shock reaches on the surface.

The problems related to velocity interferometer were solved by Barker & Hollenbach in their subsequently developed system, widely known as VISAR [75]. This system can work even with the light signal scattered from diffused surfaces. The intensity of light reflected from a diffused surface is quite insensitive to small rotations and tilt occurring in the reflecting surface. At the same time, the light reflected from a diffused surface lacks the spatial coherence and hence to obtain good interference fringes the path difference between two legs of Michelson interferometer should be nearly equal. To obtain fringes from the Doppler shifted light there should be a time delay in the two interfering light signals. The concept of Wide Angle Michelson Interferometer [76] (WAMI) has been invoked to meet these two apparently mutually exclusive requirements. WAMI is similar to Michelson interferometer except one of the two mirrors is replaced by an etalon, which is polished at one side to behave as a mirror. The apparent position of mirrorized rear surface of the transparent etalon is closer to the beam splitter than its actual position, hence meets the criterion of equal length in two legs at the same time the delay is created by the motion of light in the high refractive index material of etalon. The concept of WAMI was invoked by Barker & Hollenbach in their VISAR and a transparent etalon was placed between the beam splitter and mirror of Michelson interferometer instead of rear surface mirrorized etalon.

The other important feature that has been incorporated in VISAR for improving its accuracy is to monitor the two fringe signals that are 90° out of phase. These signals are obtained in quadrature by the method of Bouricious and Clifford [77]. Recording of two 90° out of phase signals provides good velocity resolution and can differentiate between acceleration and deceleration. A further improvement in the VISAR system has been done by Hemsing [78] to make this instrument more efficient in presence of self generated light at the

target. To improve the rise time another system based on the same principle as the VISAR and known as Optically Recording Velocity Interferometer System (ORVIS) [79] has been developed. In this instrument, the motion of interference fringes is recorded on high-speed electronic streak camera instead on a photomultiplier tube and time response of ~ 300 ps have been reported.

In parallel to VISAR many researchers have worked on Fabry-Perot interferometer (FPI) to measure the Doppler shift in the light reflected from the specimen surface. It is a multi-beam interferometer and the fringe diameter depends on the wavelength of the incident light. In 1968, Johnson and Burgees [80] reported the use of Fabry-Perot velocimeter (FPV) to measure the free surface velocity. They recorded the transmission of Fabry-Perot interferometer on a photodiode to measure the change in the wavelength of light reflected from the test surface. This work was further carried out by Durand and Laharrague [81], who measured the evolution of Fabry-Perot interference fringes on a streak camera. The similar system was also reported to be developed by Chau et al. [82] in which, they used a cylindrical lens before Fabry-Perot interferometer and convergence of interference fringes in the form of dots for better optimization of reflected light was achieved. In 1983 Seitz and Stacy [83] have reported an experimental comparison of image intensified rotating mirror camera with the electronic streak camera.

In recent years, new interferometric techniques [84, 85] based on telecommunication fiber optic components have emerged as compact and alignment free solution for free surface velocity/particle velocity history measurements in shock wave experiments. In these systems an optical coupler is used to mix the Doppler shifted light with the original laser light and to generate a beat effect. The beat frequency is recorded using fast photodiode and electronic digitizers. As the free surface velocity information is decoded from the beat frequency analysis, therefore this system can work at low laser powers. In different configuration this

heterodyne technique is known as Photon Doppler Velocimeter (PDV) [85] or All Fiber Displacement Interferometer [86], or in another VISAR like configuration this is also named as All Fiber Velocimeter [84].

1.5.2.2 Radiation Pyrometer (RP)

As already mentioned RP is used to measure the shock induced temperature rise in materials subjected to dynamic compression. The temperature is an important parameter to determine the equation of state of any shock compressed material. The measurement of temperature is frequently used to detect the melting under shock compression. The RP works on the principal of Planck's radiation law, which states that, the spectral radiance (radiation power emitted per unit area per unit solid angle) from a grey body at temp T and wavelength λ is given by:

$$I(\lambda) = \varepsilon C_1 \lambda^{-5} [\exp(C_2/\lambda T) - 1]^{-1} \quad (1.10)$$

Where C_1 and C_2 are constants while ' ε ' is the emissivity of the radiating surface. By measuring the radiance at multiple wavelengths it is possible to numerically fit the Planck's law to deduce the temperature of shocked surface. In practical systems, the radiation collected from the shocked surface is divided in different parts using beam splitters and narrow band optical filters [6-8, 11]. The output of each filter is focused on respective photodiode to measure the signals proportional to the radiance at the wavelength passed from the filter. The important task in the measurement of shock temperature is to protect the measured shock luminescence from getting corrupted due to presence of background light during experiment. Apart from this, the calibration of the instrument which is carried out using standard radiance source or black body source of known temperature is also an important step before employing it in experiment.

1.5.3 Special Measurement Techniques

Apart from the above discussed measurements, it is possible to probe the state of the matter under shock loading by performing the other in-situ measurements such as flash X-ray radiography [87] to record the dynamic movement of surfaces as well to indentify fractures. In-situ x-ray diffraction [88] can be used to determine kinetics of phase transition. Electromagnetic induction based gauges [89] can be utilized for Particle velocity measurements.

1.6 Requirement of Measurement System

From the preceding discussions it is evident that the determination of parameters like stress profile, free surface/particle velocity history and shock induced temperature profile requires dedicated measurement systems which includes instrument design, data/signal processing and estimation methods. Requirements of measurement system varies depending on the type of parameter to be measured e.g. stress profile measurement requires (i) Manganin gauge to be inserted between target plates and energized with constant current power supply during experiment, (ii) high bandwidth recording system with sufficient resolution to resolve amplitude of gauge response and (iii) estimation of pressure profile from the recorded voltage waveform.

The instrument design of a measurement system needs to incorporate sufficient dynamic range and bandwidth to accommodate change in behavior of the measured parameter. For example, the rise time of the shock pressure pulse in a typical experiment could be of order of few tens of nanoseconds. In order to record this accurately the manganin gauge should linearly follow this fast change in pressure, constant current source should remain stable and the recording systems bandwidth should be high enough (order of few tens of MHz with sampling rate > 1 GS/s) to be able to record this rise time. Similarly, the rise

time of free surface velocity in a typical shock compression experiment could also be of the order of few tens of nanoseconds. Now if depending upon the velocity per fringe constant, the VISAR instrument generates 2-3 fringes during this time, then the period of each sinusoidal fringe may be of a few nanoseconds. This puts a requirement of order of a GHz or more on the bandwidth of the recording system. Similar bandwidth requirement holds for the recording system of RP employed for measurement of shock temperature profile.

Similarly for data/signal processing and estimation method the requirement varies depending on the quality of signal recorded during experiment and physical parameter to be measured. As the dynamic compression experiments are single shot experiments and require lot of efforts, every recorded data/signal is very important and should be utilized optimally to extract information contained in it. Hence signal de-noising techniques without loss of information during data/signal processing become very important part of measurement system. Similarly the selection of the appropriate estimation method to extract the hidden information about the physical parameter from the recorded signal is also crucial. For example in case of VISAR, phase of the recorded signal contains information about the velocity history whereas in case RP spectral intensities need to be fitted to non linear Planck's distribution for determination of temperature profile. To extract accurate velocity profile from phase and temperature profile from spectral intensities selection of adequate estimation method plays key role.

In present thesis the work is carried out to minimize uncertainty in the measurement of time resolved shock temperature and free surface/particle velocity by improving measurement system in all direction starting from instrument design, data/signal processing and estimation method. In summary, the main contributions of the thesis include:

- (i) The development and calibration of RP (including optics and signal recording hardware) for measurement of transient temperature rise occurring during shock loading or any other phenomenon of rapid energy deposition.
- (ii) The development of non-linear least squares estimation based method/algorithm for estimation of temperature and emissivity from recorded luminescence data in shock loading experiment.
- (iii) The optimization of SRS parameters such as aperture opening, laser power and PMT supply voltage of VISAR to improve the SNR of the signals recorded during dynamic compression experiments and to identify the linear range of operation of SRS.
- (iv) The development and implementation of modified Wiener filter based novel de-noising algorithm for enhancing the accuracy of estimation of free surface/particle velocity of target subjected to shock loading.
- (v) The development and characterization of Linear Time Invariant (LTI) model of VISAR in time as well as frequency domain.
- (vi) Proposing a novel method of data handling to solve the inverse problem of estimating free surface/particle velocity using two delay VISAR.

1.7 Thesis Layout

The present thesis is organized in seven chapters. Basics of shock physics and introductory concepts of various shock generating techniques as well as diagnostics have already been discussed in this chapter (Chapter-1). Chapter 2 will be presenting the literature survey carried out on topics related to the problems taken up to form this thesis. The literature survey provides the status on the availability of the solutions in the open literature and issues those are open to resolve.

The third chapter of the thesis presents the development of the multi channel RP system capable of providing information about the time resolved temperature profile of the material due to heating during shock propagation. The instrument is based on the in-situ measurement of shock luminescence of the heated target material during the experiment. This chapter, also reports the process of calibration of the RP carried out using National Institute of Standards and Technology (NIST) traceable equipments. The estimation of temperature is carried out using non-linear least square error minimization between measured spectral points and the corresponding spectral points from the Planck's distribution. Apart from temperature, emissivity of the target surface also gets estimated using present analysis method. As the Gauss-Newton method for non-linear error minimization does not hold good for the cases where one estimate is very far away from the previous estimate (which are generally the case in the shock loading experiments), Levenberg-Marquardt method is utilized to overcome this problem. The results on the measurement of temperature profile of the exploding foil in some of the experiments using the developed RP are also part of this chapter.

As discussed earlier, another important parameter needed for characterization of shock loaded material is particle/free surface velocity history measured using VISAR. The subsequent chapters (chapter 4 to chapter 6) deal with the characterization of SRS, signal processing methods and modeling of VISAR to improve accuracy of the measurement. Chapter 4, discusses the design, characterization and implementation of the SRS for VISAR system existing in our laboratory is presented. The work includes the measurement of linearity with respect to parameters such as PMT gain and optical input power. Important objective of this optimization was to find out the region of operation of the SRS used in the VISAR instrument.

Chapter five deals with methodology developed for handling and pre-processing of the data recorded by the VISAR instrument. It contains methods of reading experimental

data file presented in the comma separated format (CSV) and selecting required data for signal pre processing based on the information available about the experimental setup. A novel proposed de-noising method based on the modified Wiener filter has also been discussed in this chapter. The improvement in the accuracy and precision of measured free surface velocity history in experiments by using developed de-noising method has been reported.

Output of a modeled instrument corresponding to the defined input signal provides the results that are useful for having deep insight of the instrument response and helps in improving the understanding about it. For the same purpose, Linear Time Invariant (LTI) model of the VISAR instrument based on the first principle has been developed and is presented in Chapter six. This VISAR model has been characterized in frequency domain by calculating its frequency and phase response. Further the linearity of model is verified using additivity and homogeneity property of the LTI system. To benchmark this model, a free surface velocity profile generated through simulations for a given experimental configuration has been used as input to the model and an expected fringe record has been obtained as output. Further, an experiment has been conducted with the identical configuration and interference fringe record has been generated. The closeness of the model generated fringe record and experimentally produced fringe record is established using cross correlation between the two signals in time as well as frequency domain.

To enhance the dynamic range of the instrument and overcome its limitation, it is proposed that instead of single optical delay the instrument should have two delays. The problem with two delay system is that no standard method is reported for combining the data for determination of the velocity profile. This chapter presents the novel method of inverse filtering for determining velocity profile from the VISAR data recorded from two different delays. This method of inverse filtering is based on the Wiener inverse filter and combines

data of two delay VISAR system to generate displacement/velocity history of the moving target surface.

Finally, chapter seven of the thesis summarizes the work presented in the preceding chapters. Also, the limitations of the presently developed methodology for minimizing uncertainty in the measurement of parameters during shock compression experiments have been discussed. This chapter also contains future scopes of the further developments to mitigate these limitations.

Chapter 2

Literature Survey

2.1 Introduction

Error or uncertainty minimization in a measurement system or in a process is a multistep procedure. The measurement system/process involves steps like instrument design, data/signal processing and estimation method. In general, the functions and requirements of these three steps are common for all measurement system. Instrument design involves selection of suitable sensor, understanding of its response to the change in physical parameter and linear recording of that response. An instrument with good design generates a response to a physical parameter which is linear (amplitude and time response) with sufficient dynamic response (amplitude and time response). Data/signal processing is the step which can be applied to the recorded signal for improving the signal quality. It may be possible that despite the sufficient care taken in instrument design, the recorded signal may not have sufficient SNR for further analysis and estimation of the desired parameter. In some cases, only selected portion of recorded data is required to be analyzed and/or the data from multiple channels of instruments needed to be sorted together for estimation. Activities of improving SNR, data selection and data sorting are carried out during data/signal processing step of measurement system/process. Application of estimation techniques on the processed data yields the physical parameter for which measurement system is designed. For example, temperature and emissivity are the estimated physical parameters after applying non linear least square estimation technique on the processed shock luminescence data.

Now as already mentioned in previous chapter, the aim of the present thesis was to (i) design and develop the RP for time resolved measurement of temperature rise during rapid deposition of energy in dynamic compression experiments and exploding wire experiments; (ii) formulate a suitable analysis technique for post processing of the recorded luminescence data to estimate temperature profile; (iii) minimize the uncertainty by improving signal recording and processing methods in the free surface/particle velocity history derived from the time resolved measurement of Doppler shift employing VISAR instrument; and (iv) modeling the VISAR instrument for overcoming the limitation, if any, for dynamic compression experiments. In order to develop hardware for RP and recording system of VISAR and to formulate the methodology for signal processing and estimation technique, a survey of worldwide available open literature has been carried out. The following sections describe the systems and methodologies reported in the literature in this direction. Also, wherever possible, a comparison of the developed systems with those reported in the literature has been provided.

2.2 Radiation Pyrometer (RP) for Time Resolved Measurement of Transient Temperature

The word 'Pyrometer' comes from the Greek word 'pyro' means fire and 'meter' means measure. In principle the pyrometer technique came into existence to measure temperature of furnaces, where, accessing the surface of the heated body is difficult. The early developed RP used thermal detectors like resistance wire, flat strip thermocouple, flat bead thermocouple, bimetallic strips etc. [1, 2]. The early devices based on these mentioned sensors used Stefan Boltzmann radiation law and Lambert cosine law to calculate the total temperature of the heated surface of the target. The major drawback of these devices is the slow response time which makes them inadequate for measurement of fast changing

temperature such as that during shock loading of the materials and electrical explosion of foils. The reason for this is the inherently slow process of conduction of heat in the thermocouples. Despite the slow response of above mentioned instruments, some researcher have attempted to measure shock temperature using thermister and bi-metallic strips in past [3-7].

The basic structure of the RP is divided in three parts namely collection and transport of shock luminescence, selection of wavelength and conversion of optical signal into electrical signal [8-10]. Each part of the RP has its role and the components in each part need to be modified depending on the temperature regime to be accessed. For example, for low temperatures, all the parts of RP including optical to electrical converters (Mercury Cadmium Telluride detectors) should have good response in infrared region ($\sim 1 - 5 \mu\text{m}$) as the wavelengths of the emitted radiation falls in this range. The RP to be used in dynamic compression experiments is not a standard catalog product of any manufacturer; rather it has been developed, modified and redesigned by the users as per their requirement. Considering this fact, for dynamic compression facility existing in our lab a RP has been developed.

In principle, researchers have devised three major configurations for the RP's to be used in dynamic compression experiments. As shown in Fig. 2.1, Boslough *et.al.* [9] have developed a RP based on the free space optics where, shock luminescence from the target chamber is collected through objective lens and mirrors. This luminescence is then divided into four channels using beam splitters. Interference filters are then used to select a desired wavelength from the collected shock luminescence. Further, focusing lenses are used for converging the collected radiation at selected wavelength on to the calibrated detectors. The advantages of this setup are that the collected radiance data is equally distributed in all channels and the entire photo detectors look at the same area of the of radiance data, using

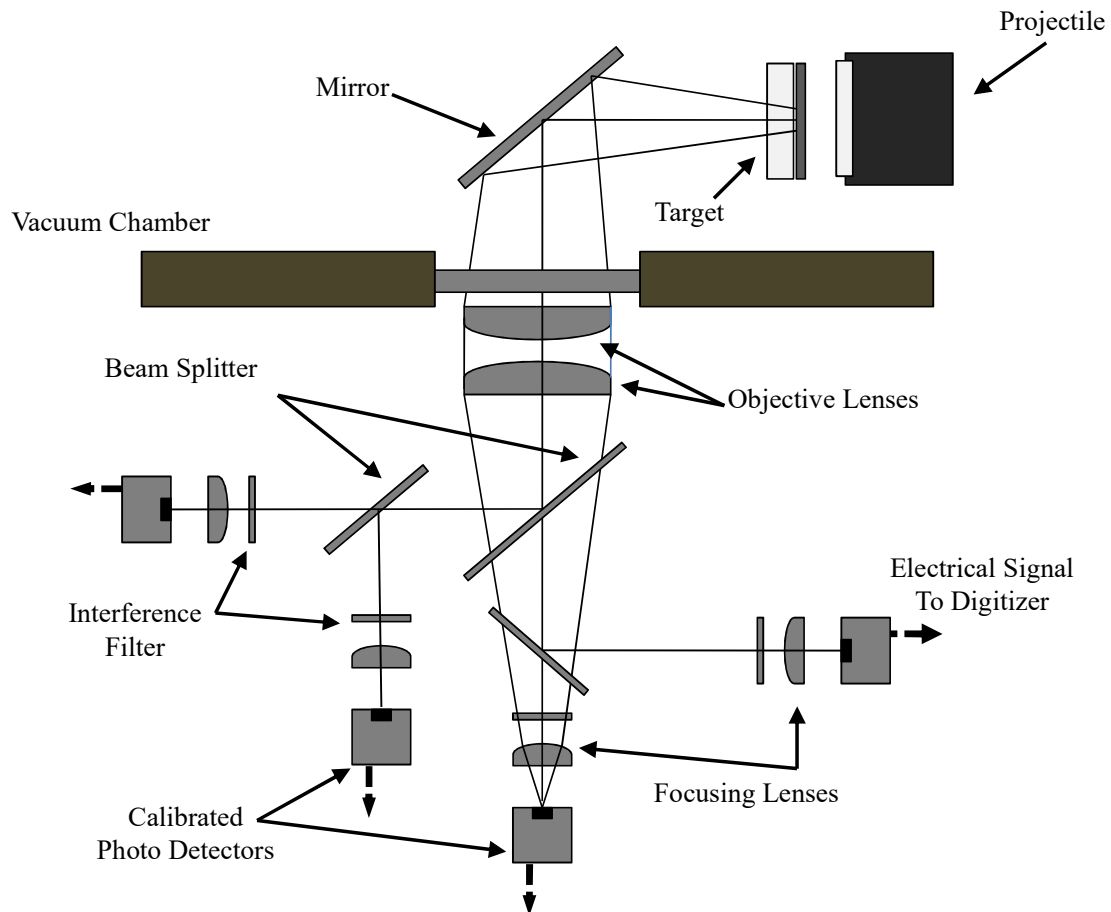


Figure 2.1: Schematic of RP developed by Boslough *et.al.* [9]

target surface. But the collection mirror and objective lens often becomes difficult, as the components of RP are required to be placed just outside the target chamber of the shock loading facility. It is further noted that the depth of field of the objective lenses are fixed hence as the target moves, the detectors may go out of focus leading a reduction in collection efficiency during experiment.

With the advancement in the fiber optic techniques in 1995, Holmes [10] developed a new optical design of RP (Fig. 2.2), where, fibers are used to collect and transport light from target surface to the filter assembly and then on to the detectors (PMT's in this case). As shown in Fig. 2.2, a fiber bundle having number of fibers equivalent to the number of channels is used. The common end of the fiber bundle is placed near the target whereas the individual branch ends are aligned with the wavelength selection filters and detectors i.e.

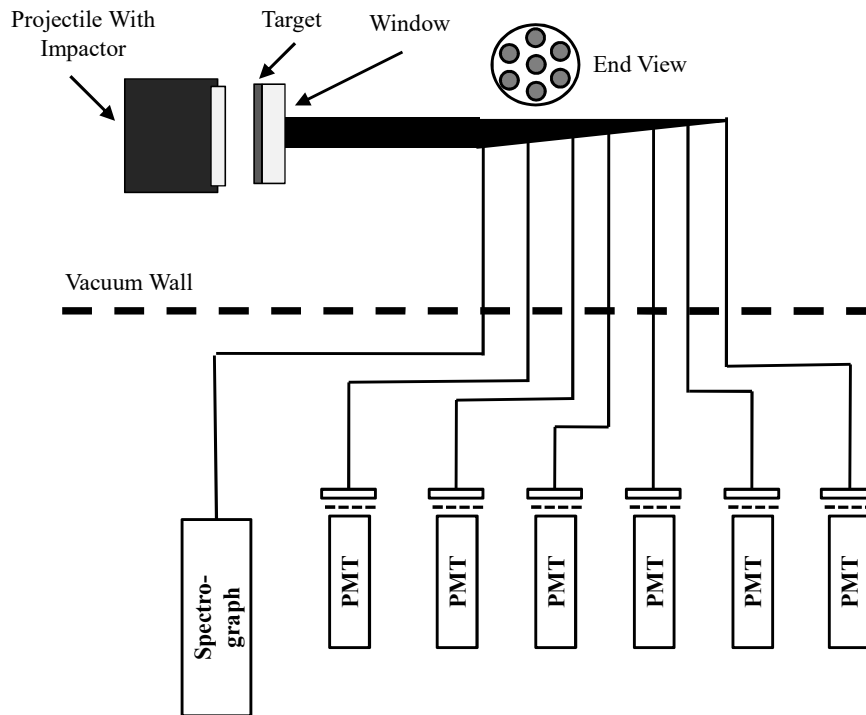


Figure 2.2: Schematic of RP as described by Holmes *et.al.* [10]

individual fibers are used to carry shock luminescence data from one of the point of the target surface to corresponding filter and detector assembly. Since optical fibers are used to carry the information the detector assemblies need not to be in line of sight of the target. Also beam splitters are not required for dividing light into many channels. Further the problem of depth of focus is also eliminated in such design. The drawback of this system is that each fiber is looking at different point on the target surface which may pose difficulty in correct estimation of temperature in case of non uniform distribution of the temperature on the surface.

To address the issue of error in temperature estimation due to collection of shock luminescence from different part of the target surface another design using optical fiber bundles is reported by Gupta *et.al.* [11]. Schematic of the shock luminescence collection setup used by Gupta *et al.* [11] is presented in Fig. 2.3. In this setup reflecting mirror and lens are used to focus the shock luminescence on to the common end of the randomized fiber bundle. This fiber bundle consists of many small diameter fibers typically of the order of 50 μm . Further this bundle of fiber is divided into branches at the other end to create the

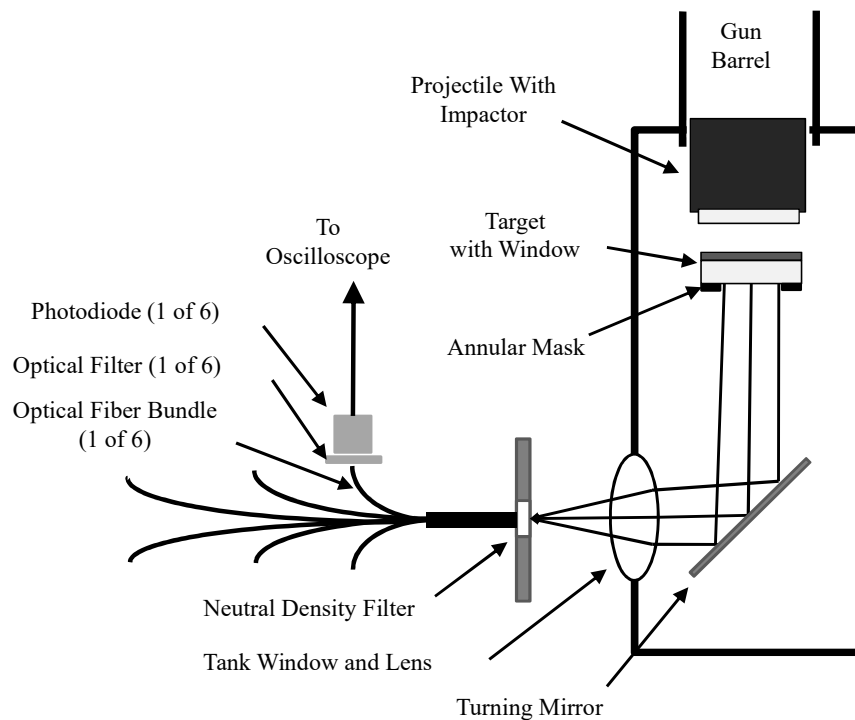


Figure 2.3: Schematic of RP developed by Gupta *et al.*[11].

channels of the RP. The advantage of having such arrangement is that all the RP channels are looking at approximately the equal amount of shock luminescence if focused using lens and distribution of branches are uniform. Further the use of fiber bundle eliminates the requirement of placing optical components such as filters and detectors, in line of site of target chamber, only common end of fiber bundle needed to be placed near the target chamber. Since the mirror and lens assembly is used for collecting and focusing of shock luminescence data the problem of depth of focus is still present.

Having reviewed the available literature on this instrument, a RP has been developed for the measurement of shock induced temperature rise in dynamic compression experiments at BARC. As discussed in subsequent chapter, this in-house developed RP uses a single optical fiber mounted in front of the target for collecting shock luminescence data from the target surface. On the other end of the fiber the collected radiation is divided into four different channels using beam splitters and filter assembly before getting detected by photo

detectors. This design overcomes the issue due to the limitation of depth of field, non uniformity of temperature distribution and line of sight requirement by use of single optical fiber and beam splitter assembly. As far as the estimation of temperature and emissivity is concerned, non linear least square estimation technique is applied by most of the researchers [3-23]. The presently developed RP, however, uses a modified non linear least square estimation based on Levenberg-Marquardt algorithm for all time convergence to estimate the temperature and emissivity.

2.3 Characterization of Signal Recording System of VISAR

As mentioned earlier the linearity of instrument response is important for measurement of physical parameter without any artefact. In case of VISAR, the SRS consists of PMT's which convert the optical modulations generated due to interference between the Doppler shifted laser lights from the moving target surface. VISAR is first developed and used in late sixties at Sandia Laboratories [24, 27, 68, 73]. The equation for velocity estimation at any given time using VISAR is given as:

$$v(t) = VPF \times F(t) \quad (2.1)$$

where $v(t)$ is the estimated velocity, VPF , the velocity per fringe is the instrument constant based on its optical design and $F(t)$ is the fringe count. Barker [75], the founder of this instrument, has discussed about various factors such as index of refraction, laser light wavelength, dispersion in elements, distance travelled by light and calibration of window material, which can influence the accuracy of the measurement of free surface/particle velocity of the moving target. According to the report by Barker [75], the overall uncertainty in the calculation of the velocity per fringe constant due to these factors could range from ~ 0.5 % to 1%. Further the uncertainty in estimating fringe count $F(t)$ depends on the linearity of the recording system and noise on the recorded data. For example, it has been reported

[75] that around 6% uncertainty in signal amplitude leads to ± 0.02 fringe uncertainty in counting fractional fringe. It is further mentioned that the counting of complete fringe has almost zero error. Hence, once the optical design of the VISAR is complete the overall velocity measurement uncertainty of VISAR depends on linearity and accuracy of its recording system consisting of PMT and high bandwidth oscilloscopes [75].

PMT is very sensitive optical detector where photon falling on the cathode generates photoelectrons. These photoelectrons are amplified inside the tube using the process of secondary emission through multiple dynodes. The amplified electron current corresponding to photons falling on cathode is collected at anode terminal. Output current of PMT i.e. anode current is generally assumed to be linear with respect to the input optical intensity and anode current is zero when there is no input light. PMT in general, also has large dynamic range of operation corresponding to the input optical signal provided the dark current or background current is kept very low, not more than a few nano-amperes. The major sources of error while doing measurement using PMT are (i) saturation effect (ii) presence of after pulse and (iii) dark current. Fenster *et al.* [90] have discussed the methods of determining linearity and fatigue in the photomultipliers. Hartman *et al.* [91] have studied the response of photomultiplier tube in the saturation region as a function of ambient background light intensity, photocathode illumination area, magnetic field orientation and ambient temperature using high-speed pulsed light sources. Land *et al.* [92], however, performed the theoretical studies to find the factors which affect the onset of nonlinear response of a photomultiplier to the light intensity incident on the photocathode, when dynode voltages are provided by a linear resistance chain. The percentage deviation from linearity of the anode current has been reported to be independent of the number of dynodes and the gain per stage [92]. Similarly, Riley *et al.* [93] and Coates *et al.* [94] studied the presence of after pulse for high intensity

optical input and reported that some amount of anode current remains for larger time (\sim few μ s).

Tripathi *et al.* [95] have extensively studied the large number of PMT's from different suppliers before being used as the surface detectors for Pierre Auger Observatory. They have developed specialized instrumentation to accurately measure the PMT characteristics such as gain, dark current, single photoelectron spectrum, dark pulse rate, after pulse ratio, quantum efficiency and linearity while being used in the set up. In another application Brice *et al.* [96], have studied PMTs to be used as the detector for the MiniBooNE experiments at Fermi National Accelerator Laboratory. They tested the PMTs for dark charge and timing resolution, double pulsing rate and desired operating voltage for each tube, so that the tubes could be sorted for optimal placement in the detector. In yet another application, Abbasi *et al.* [97] have carried out the laboratory characterization and calibration of over 5000 PMT's before deployment in detector system of the South Pole IceCube neutrino observatory. Characterization included the parameterization for single photoelectron charge spectrum and saturation behavior. Also, the investigations pertaining to time resolution, late pulses and after pulses have been carried out in that study.

All these above mentioned investigations on characterization of PMTs deployed in detection setup for different applications indicate that though the behaviors of PMTs are well characterized at manufacturer's end yet they are recalibrated and re-characterized again before being used in a particular application. To my knowledge, such studies are not available in open literature for the PMTs used as detectors in VISAR setup. Therefore, a procedure has been developed for characterization of PMT in VISAR setup existing at our laboratory and it has been utilized to determine the linear range of operation in this setup for shock experiments on different materials.

2.4 Signal De-noising specific to VISAR

Once the signals are recorded in a dynamic compression experiment using VISAR setup, the next step is the processing of data for improvement in the signal quality. The accuracy and precision of the VISAR depends not only on the good optical design, linear optical to electrical conversion and recording system but also on the quality of the recorded signal. The phase of the recorded signal contains the information about the particle/free surface velocity history of the shock loaded target. Phase of the signal changes from 0 to 2π for a single fringe (one complete cycle of sinusoidal signal), but for multiple integral as well as fractional fringes the phase again goes to 0 after reaching 2π . Identification of this phase jump indicates the completion of one cycle and start of new fringe. Hence it is very important to identify these phase jumps for counting correct number of fringes. Phase unwrapping algorithms are developed to detect phase jumps and convert them in accurate total number of fringes.

Itoh [98] has presented one of the pioneer works in the development of phase unwrapping algorithm. He showed that the actual phase sequence that can be retrieved from its original (wrapped) signal is the cascade of three simple operations i.e. differentiating, wrapping and integrating. He also pointed out that the presence of noise can disturb the ideal conditions required for unwrapping process. Similar observations have also been recorded in the work of Sur *et al.* [99], Gangopadhyay *et al.* [100] and Ying [101]. In the references [99-101], it is pointed out that the presence of noise can lead to false phase jump in the unwrapped phase leading to erroneous estimation of the phase and velocity of the moving surface. Hence improving signal quality by de-noising becomes essential for estimating correct phase from the recorded signal.

De-noising of a signal corrupted by additive noise having separable spectrum for signal and noise, is carried out using linear filters like low pass, high pass and band pass

filters [102]. However, for signals where noise and signal spectrums are non-separable, it is difficult to completely separate the signal from the noise. Nevertheless, the effect of noise can be reduced by estimating signal and noise spectrum from available means of signal processing. Three commonly used techniques for de-noising are Fourier coefficient thresholding, wavelet shrinkage and spectral subtraction. The technique of Fourier coefficient thresholding requires calculation of Fourier transform of the noisy signal. The spectral components of signal are then selected based on the predetermined thresholding criteria. The scheme of the Fourier coefficient thresholding can be represented as

$$P_{\hat{x}}(f) = \begin{cases} P_x(f) & P_x(f) > TH \\ 0 & \text{Otherwise} \end{cases} \quad (2.2a)$$

$$P_{\hat{a}}(f) = \begin{cases} P_x(f) & P_x(f) \leq TH \\ 0 & \text{Otherwise} \end{cases} \quad (2.2b)$$

Where, $P_{\hat{x}}(f)$ is the estimated de-noised signal power spectrum, $P_{\hat{a}}(f)$ is the estimated noise power spectrum using noisy signal power spectrum $P_x(f)$ and threshold value TH . The threshold value can be estimated based on some optimized percentage of the maximum and minimum power of the noisy signal power spectrum and can be given as

$$TH = \left((P_{x,max} - P_{x,min}) \times p / 100 \right) + P_{x,min} \quad (2.3)$$

where p is some division ratio (or percentage) of maximum signal power for optimized de-noising of the signal. Such method for signal de-noising is used by researchers in image processing [103, 104].

Another class of de-noising method is called wavelet shrinkage method. In this method the signal is decomposed in various sub-bands of time-frequency representation using wavelet transform. Common types of mother wavelet used are Daubechies (db), coiflets, symlets, bio-orthogonal, reverse bio-orthogonal etc. These are again divided into sub-types of wavelet. The important aspect of wavelet de-noising is the selection of threshold. The threshold type can be soft or hard. Threshold selection rules that can be applied are ‘rigsure’

using the principle of Stein's Unbiased Risk, 'heursure' using the heuristic version of the first option, 'sqtwolog' using the universal threshold $\sqrt{2 * \log(.)}$, and 'minimaxi' using minimax thresholding. Rescaling using a single estimation of level noise based on first-level coefficients is expressed as 'sln' and rescaling using level-dependent estimation of noise is expressed as 'mln'. The implementation of the scheme requires selection of mother wavelet, selection of the number of level for decomposition and method of selecting threshold. Authors of the ref. [105-108] have used the method of wavelet analysis for estimating noise spectrums and de-noising of 1-D (signal de-noising) as well as 2-D (image de-noising) data.

Spectral subtraction based on the subtraction of noise estimate from the noisy signal spectrum, is another very popular and one of the oldest methods of de-noising. The scheme of spectral subtraction can be expressed as:

$$|\hat{X}(f)|^b = \begin{cases} |X(f)|^b - a\overline{|D(f)|^b} \\ \beta\overline{|D(f)|^b}, \text{ if } |X(f)|^b - a\overline{|D(f)|^b} < \beta\overline{|D(f)|^b} \end{cases} \quad (2.4)$$

The $\hat{X}(f)$ is de-noised signal power spectrum, $X(f)$ is the noisy signal spectrum and $D(f)$ is the noise spectrum estimate. This estimate of noise is obtained from the period when no change in physical parameter to be measured is present and recorded data captures the measurement channels characteristic (e.g. detector response, channel noise, recording system noise etc.). Averaging this signal over a period of time generates a fair idea of the noise characteristic of the signal recording channel and can be utilized for spectral subtraction. The exponent b is selected for either spectral subtraction ($b = 1$) or power spectral spectrum subtraction ($b = 2$). The other two parameters are scaling parameter (a) and noise floor (β). The method of spectral subtraction is used in speech enhancement and image processing [109 – 113].

For all these thresholding based techniques the quality of reconstruction depends on the selection of threshold. Larger threshold will remove the useful signal components from

the reconstructed signal whereas the smaller threshold will leave noise components unaltered in the reconstructed signal. Another class of linear adaptive filters which works on the criteria of minimizing the mean square error for wide sense stationary signals is Wiener filter. This filter is widely used in applications pertaining to image processing [103, 104, 108] and speech enhancement [107]. This thesis presents the design and characterization of a modified Wiener filter developed for de-noising of VISAR signals. This filter has been applied successfully to de-noise the VISAR signals reordered in shock wave experiments.

2.5 Development of VISAR Model and Inverse Filtering

Theory behind the working principle of VISAR and methods of data reduction/estimation has been established by various researchers in past [73, 75, 114, 115]. The Fig. 2.4 displays a typical schematic of the VISAR developed by Barker & Hollenbach [73].

The well known relationship between fringe count and target surface velocity is given by Eq. 2.1. As mentioned in earlier section, the velocity per fringe VPF constant of the equipment is derived from its optical design. It has two components, first is the wavelength λ of the un-shifted laser source and second is the time delay τ , which is the time lag between the two interfering beams calculated on the basis of the optical properties of the etalon. The expression relating these quantities is given as:

$$VPF = \lambda / 2\tau \quad (2.5)$$

For a given length of etalon the amount of optical delay τ , can be calculated as

$$\tau = \left(\frac{2h}{c}\right) \left(n - \frac{1}{n}\right) \quad (2.6)$$

where, the h is the length of the etalon, n is the index of refraction and c is the speed of light. For a given laser source, amount of optical delay decides the VPF of the VISAR

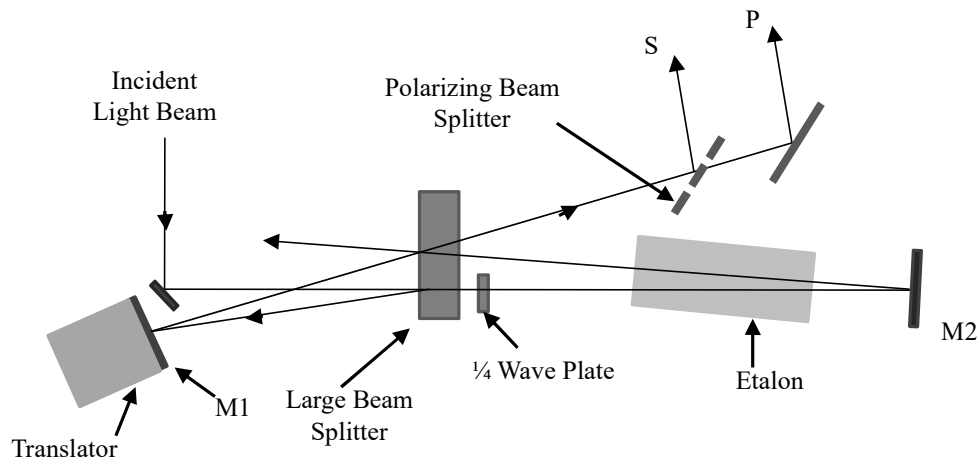


Figure 2.4: Schematic of VISAR velocity interferometer as described by Barker & Hollenbach [73]

which intern governs the sensitivity of the instrument. Larger the value of optical delay τ the more will be the number of fringes generated for a given free surface velocity of the target. Apart from this, it has also been reported [75] that the VISAR is insensitive to the velocities which produce the phase change of 2π or integer multiple of 2π in a time exactly equal to the optical delay τ . Such behaviour of VISAR is very interesting and plays important role in design of a VISAR set up for use in a particular experiment.

Dolan [115] has provided a detailed analysis of VISAR instrument as an interferometer. The commonly used method of data reduction/estimation is ‘method of VISAR approximation’ given by Eq. 2.1. Dolan [115] has also reported that the VISAR analysis can be done as a forward problem where phase is directly related to the displacement history of the moving target. For data reduction and estimation of velocity/position history of the moving target surface using analysis of forward problem requires solving the inverse of forward problem. The inverse of the forward problem is practically difficult to apply specially in case of the noise present in the recorded data [115].

To have better understanding of the instrument and provide probable solution to some of the limitations, the forward problem has been modeled as a Linear Time Invariant (LTI)

model and characterized in time as well as frequency domain. The development of such model is useful in explaining different theories of VISAR motioned above. The advantage of such model is that the response of instrument with respect to its different parameters such as optical delay, VPF and input velocity (or displacement history) can be studied. The major observations of the model response to these variables are discussed in Chapter 6 of this thesis. One of the important observation about VISAR model is that, it has periodic zeros in its response at frequencies that are integer multiple of $1/\tau$. This is the cause for the reported [74, 114, 115] limitation of VISAR instrument in determining velocity history of the moving target with velocity rise time of the order of instrument delay. Under such circumstances VISAR approximation method of data reduction does not work well. For solution to this limitation, Erskine [116] has proposed a method of two delay VISAR and its data reduction method in frequency domain. This thesis reports a new method of inverse filtering based on Wiener filter for the data reduction by combining the phase data of the two delay VISAR.

Chapter 3

Development of Radiation Pyrometer (RP) and its Parameter Estimation

3.1 Introduction

Dynamic (shock or isentropic) compression of materials generates not only very high pressures but also high temperatures in the materials. As already mentioned in chapter 1, the Hugoniot of a material can be characterized by five shock parameters namely, pressure, density, particle velocity, shock velocity and the shock induced temperature rise. All of these parameters, except the shock induced temperature rise can be inferred by measuring any two of the rest of the parameters in conjunction with shock jump conditions (Equ. 1.2 to 1.4 in Chapter 1). However, for determination of complete thermodynamic state of the shock compressed material, the knowledge of the shock induced temperature rise is essential. Therefore, measurement of shock induced temperature rise is important. The knowledge of temperature rise under shock loading gives insight into the partition of the total energy in the shocked system and provides additional information on the complete equation of state, solid-solid phase transition and melting of shock compressed materials[3-23].

Temperature is generally measured by observing some temperature dependent physical phenomena, e.g. change in resistance, volumetric expansion, development of vapour pressure and spectral characteristic etc. Depending on the nature of contact between the medium of interest and the device, the temperature measurement techniques are classified as invasive, semi-invasive and non-invasive. Invasive techniques use the transducer in direct

contact with the medium of interest, for example, a thermocouple immersed in a liquid in a glass. In semi-invasive techniques, the surface of interest is treated in some way to enable remote observation, for instance the use of thermochromic liquid crystals, which change colour with temperature. On the other hand, techniques like RP are non contact type where medium of interest is observed remotely.

A typical dynamic compression experiment lasts for about few micro-seconds and changes in pressure and temperature occurs in time scale of the order of a few tens of nano-seconds or smaller. The conventional invasive methods of temperature measurement (thermocouples, resistance temperature detector or RTD etc) require the sensor to be thermally equilibrated with the medium of interest through conduction of heat. The process of attaining thermal equilibrium between sensor and the medium is much slower than the rate at which the temperature increases in the shock compressed medium, so such invasive methods cannot be used for measurement of temperature under such conditions. On the other hand, a RP, measures the intensities of electromagnetic radiation emitted by the shock heated object using photo-detectors with response time of about a few nanoseconds. Since the radiation pyrometry is a non contact technique, it is specifically useful for measurement of temperature in the processes where contamination/intrusion has to be avoided.

In present chapter, basic concepts of the RP and shock temperature are discussed. Details of the RP instrument developed by us for recording radiation intensities at various wavelengths are presented. Along with that the procedure for RP calibration and parameter estimation method for retrieving temperature and emissivity is presented. The developed instrument is finally used for measurement of transient temperature rise in different situations.

3.2 Theory of Radiation Temperature Measurement

Pyrometers use the fact that all objects above absolute zero Kelvin radiate thermal energy. This thermal energy, which is the measure of the average atomic kinetic energy, is radiated in the form of electromagnetic radiation. The thermal radiation consists of electromagnetic radiation of wavelength band between $0.1 \mu\text{m}$ and $100 \mu\text{m}$ in electromagnetic spectrum (Fig. 3.1). The band of wavelength emitted will depend on the temperature. As the temperature rises, the intensities of thermal radiation increase and the band of emitted spectrum shifts to smaller wavelength. This is manifested as a common experience that higher the temperature the brighter the object appears.

A relationship between the intensity of radiation at a particular wavelength λ and absolute temperature T is governed by Planck's law [117]. The radiant flux density $I(\lambda)$ as power of electromagnetic radiation per unit of wavelength (λ) is presented in Equ. 1.10. The value of radiation constants C_1 and C_2 are given as $1.191 \times 10^{-16} \text{ W}\cdot\text{m}^2/\text{sr}$ and $0.01439 \text{ m}\cdot\text{K}$, respectively. Emissivity measured on a scale from 0 to 1 is the ratio of electromagnetic flux that is emanated from the source to the flux emanated from the black body source at the same temperature.

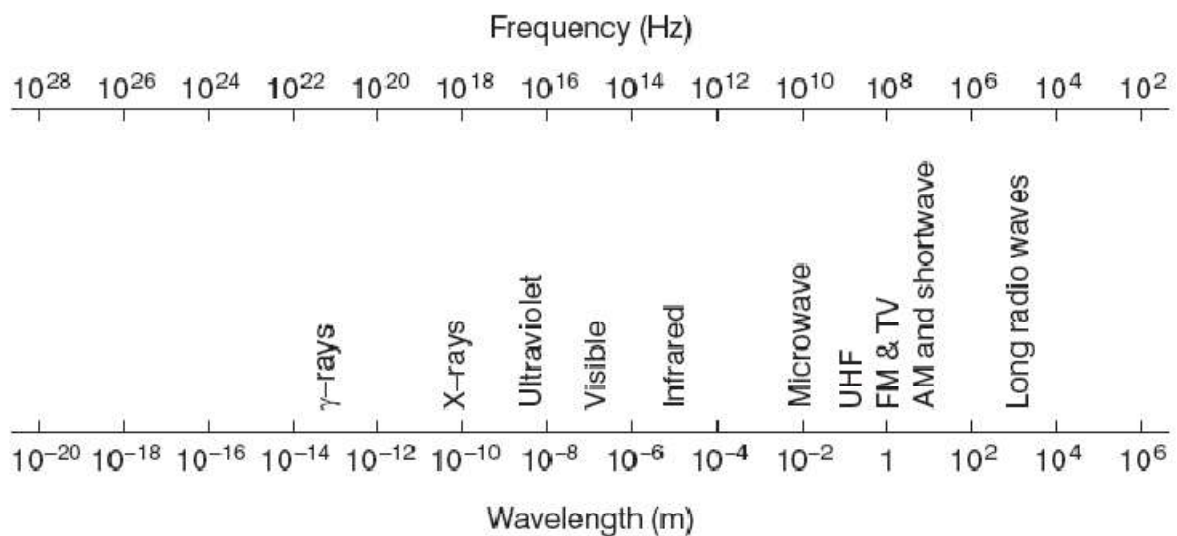


Figure 3.1: The Electromagnetic Spectrum

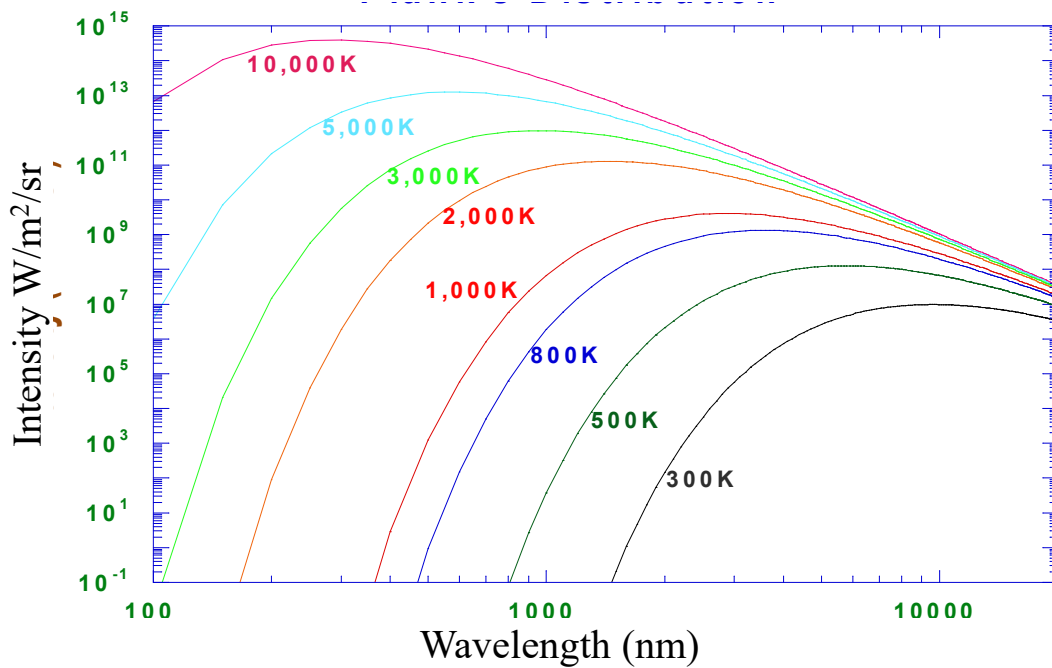


Figure 3.2: The Spectral densities at different temperatures

Once the radiation intensities $I(\lambda)$ at different wavelengths are measured, the temperature T and emissivity ε can be estimated by fitting the Planck's law (Equ. 1.10) to the measured intensities at different wavelengths. Spectral densities for different temperatures for perfect blackbody ($\varepsilon = 1$) are shown in Fig. 3.2.

3.3 Theory of Shock Temperature

The determination of temperature of shock compressed material is quite challenging [3-5]. Kromer [6] first reported shock-temperature measurements in transparent materials such as alkali halides and water. The techniques employed by Kromer et.al. [6] used to view the explosively shocked material through the transparent un-shocked sample and measure the radiation versus time at a series of wavelengths to obtain black and grey body temperatures.

The techniques for measurement of shock temperature developed by Layzenga and Ahrens [13] employing four to six channel photodiode systems integrated with light gas guns were used to study a series of transparent materials, including forsterite, and crystalline &

fused quartz. In the ideal experiment, the observed temperature is related to the spectral radiance from the metal-window interface, provided the shock transmitted into the window does not produce opacity at the shock front and the temperature behind the shock front in the window remains substantially below the temperature of shocked metal film. The relation of the radiative interface temperature to the initial Hugoniot temperature in the metal is dependent upon the shock temperatures in the window, the state in the metal film, which, because of the mechanical impedance mismatch between the metal film and the window is at a different pressure than the initial Hugoniot state. For many condensed media, the Mie-Gruneisen equation of state based on a finite difference formulation of the Gruneisen parameter, can be used to describe shock and post shock temperatures. The temperature along the isentrope [118] is given by

$$T_S = T_i \exp \left[- \int_{V_a}^{V_b} \left(\frac{\Gamma}{V} \right) dV \right] \quad (3.2)$$

where T_i is the initial temperature. For the principal isentrope centered at room temperature, $T_i = T_0$, $V_a = V_0$, initial volume and $V_b = V$, compressed volume. For the calculation of post shock temperature, T_i becomes T_H , the Hugoniot temperature V_a becomes V_H the volume of the shock state and $V_b = V_{00}'$, the post shock volume corresponding to the post shock temperature. For shock compression up to a volume V , P_S (the pressure along isentrope) is first obtain by using equation,

$$P_1 / 2(V_{00} - V_1) = - \int_{V_0}^{V_1} P dV + V_1 / \Gamma (P_1 - P_S) + E_{TR} \quad (3.3)$$

Then T_S , the isentropic compression temperature at volume V , may be calculated by using Equ. 3.2. Finally using definition of Grunesien parameter the shock temperature T_H can be obtained using expression:

$$\frac{V}{\Gamma} (P_H - P_S) = \int_{T_S}^{T_H} C_V dT \quad (3.4)$$

It is useful to determine both the shock temperature and post shock temperature as they provide complementary information for the thermal equation of state i.e., Γ as well as C_v . In case of molecular fluids such as water, a formulation based on the near constancy of C_P at constant pressure is used. The post shock temperatures are very sensitive to the models used to specify the Γ and its volume dependence in Grunesien equation of state. In contrast, the absolute values of shock temperatures are sensitive to the phase transition energy E_{TR} (Equ. 3.3), where the slope of T_H versus pressure curves is sensitive to specific heat. As mentioned earlier, shock temperature in an experiment can be determined by recording the radiation using transparent media and analyzing the same.

3.4 Instrument Design for RP

The actual photograph and schematic of the instrument developed as part of this thesis work is displayed in Fig. 3.3 and 3.4, respectively. The design and implementation of functionality for each part of the RP instrument is as follows.

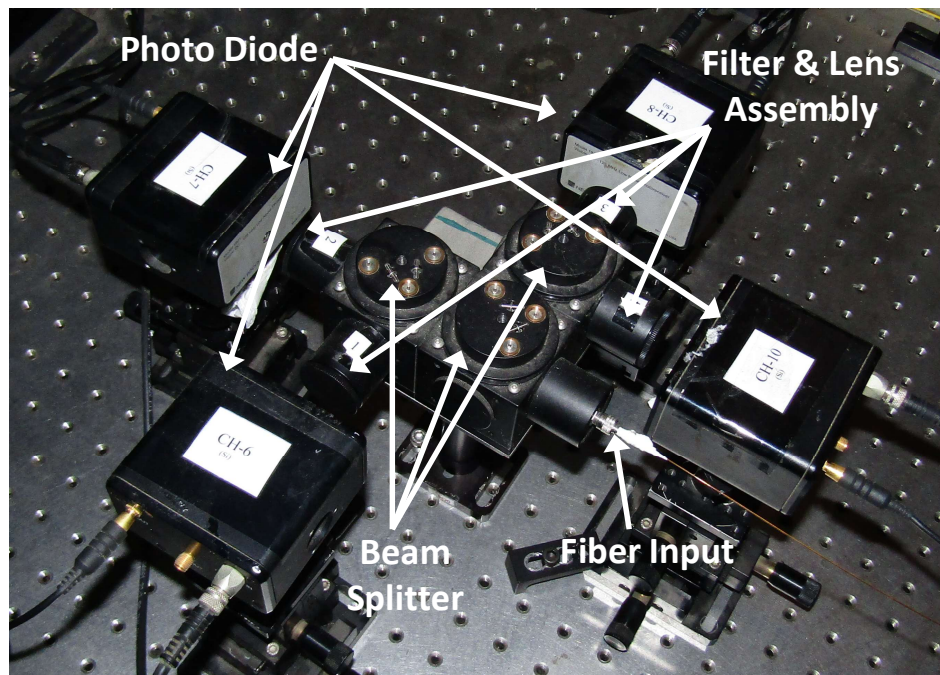


Figure 3.3: Photograph of RP Instrument

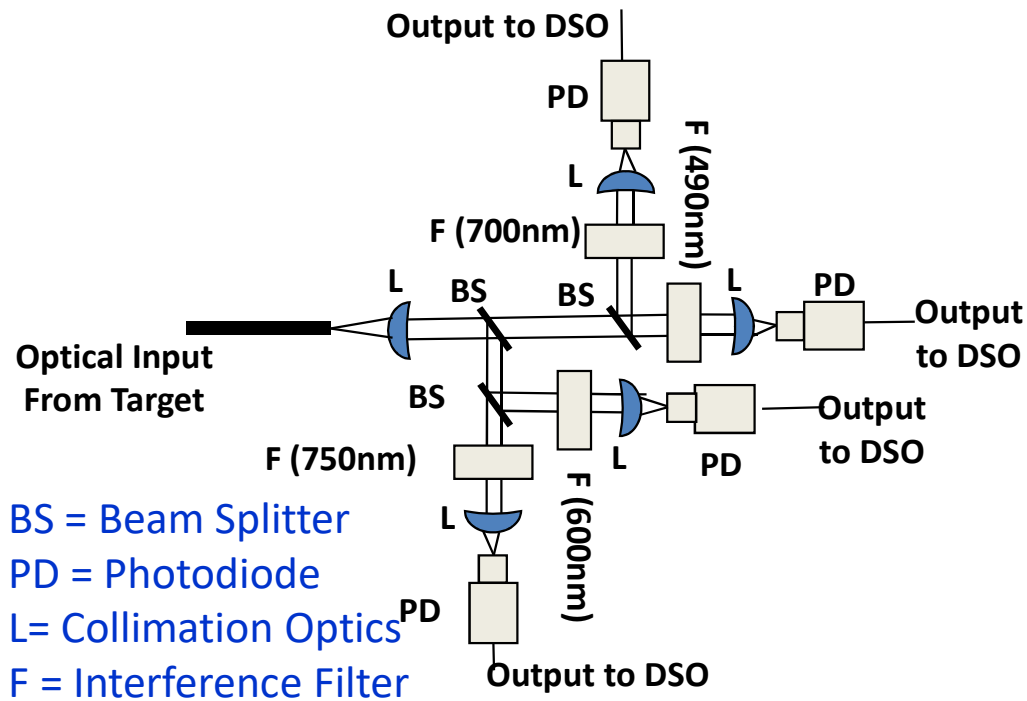


Figure 3.4: Schematic diagram of the RP

3.4.1 Radiation Collection from the Target

The radiation collection system (Fig. 3.5) is the part of instrument, which collects radiation from the target object, couples it into the fiber, and transports the collected radiation to the instrument where it gets detected. The fiber used in the RP for radiation collection from the target is all silica glass fiber (both core and clad of the fiber are made up of silica glass) having 600 μm diameter and 0.22 numerical aperture (NA). It is required that the viewing area of the RP should be as small as possible and constant throughout the experiment. For effective coupling of the radiation from the target to the fiber, a collimating lens of 15 mm focal length and 12.5 mm diameter is used. The effective NA of the radiation collection system (fiber along with the collimating lens) is about 0.01. The area of the target covered by the radiation collection system at distance of 10 cm from the target is about 165 mm^2 (ϕ 14.5 mm) which without radiation collection system could be about 1,662 mm^2 (ϕ 46 mm).

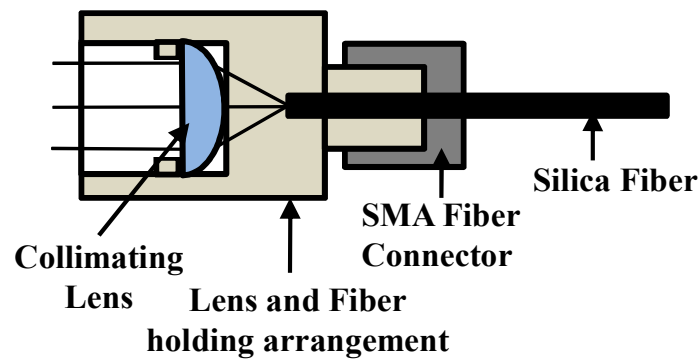


Figure 3.5: Light collection system of RP

3.4.2 Distribution of Light in Different Channels

The distribution of collected radiation in various channels in the instrument is carried out by using beam splitters. The radiation collected from the target is received at the other end of the fiber and is collimated using a lens (ϕ 12.5 mm & FL 15 mm) inside the RP instrument. This collimated beam of radiation is divided in two parts using first beam splitter (ϕ 25mm) having 50/50 transmission and reflection ratio. The transmitted and reflected radiation is further divided by passing each of these through similar kind of beam splitters. In this way the input radiation is divided into almost four equal parts. The angle of all three beam splitters are so adjusted that the reflected and transmitted light falls on the respective wavelength selection system.

3.4.3 Wavelength Selection

Wavelength selection is one of the important aspects of RP. The narrower is the wavelength band better is the estimation of the temperature using Planck's distribution. Ideally single wavelength is required for intensity collection and signal recording hence interference filters which are having very narrow wavelength band is used for wavelength selection. As shown in the Fig. 3.3, the selection of the four wavelengths for measurements is carried out by passing the each part of the collected radiation through the narrow band

interference filter of different central wavelengths. Each interference filter consists of multiple layers of evaporated coatings on the substrate such that the optical property of the filter results from wavelength interference rather than absorption. The bandwidth of the filter depends on the number of cavities and the coating thickness. The interference filters used for the wavelength selection have full width half maximum (FWHM) bandwidth of 10 nm with about ~50% transmission at the central wavelength.

3.4.4 Detection of Radiation Intensity

The detection system converts the radiation falling on it, in to an equivalent electrical signal, and this system mainly determines the transient time response of the instrument. The detection system consists of focusing lens and the photo-receiver. The focusing lens (Plano-convex lens having effective focal length of 15 mm and diameter of about 12.5 mm) focuses the filtered radiation on to the active area of the photo-receiver. The photo receiver has a silicon PIN photo-diode and an amplifier. The photo diode has detector area of 0.5 mm^2 and spectral range of 300 nm – 1050 nm, for converting filtered radiation into an electrical signal. The amplifier has a bandwidth of 125 MHz and trans-impedance gain of 40 V/mA for increasing the signal level of the photo-diode output. This detection system is capable of measuring transient change in radiation intensity of the order of ~3 ns.

3.4.5 Recording of Data

The equivalent electrical signal generated by the photo receiver is recorded on the fast digital storage oscilloscope having analog bandwidth of 1 GHz and sampling rate of 5 GS/s with a total recording time of 2 ms at highest resolution. To avoid the loss of information, the recording speed of the oscilloscope was chosen to be faster than the response time of the photo-receiver. The oscilloscope used has the facility of recording the data in ASCII text

format or comma separate text format apart from its standard format of recording in “.isf” format.

3.5 Calibration of RP Instrument

Calibration is the process by which the known measurement (the standard value or instrument) are compared with the measurements using the developed instrument. The process of calibration is useful for determining accuracy of instrument and it also determines the traceability of the measurement. In case of RP, the calibration factor is determined by comparing the output of each optical channel, in terms of voltage, with respect to known radiance input to the pyrometer, using standard radiation source. The shock experiments are destructive in nature and optical probe that used for collecting shock radiance and transport to pyrometer, get destroyed in each experiment, hence the calibration procedure is performed just before each experiment.

Calibration of the RP instrument provides the information about the response of each optical channel corresponding to the radiance of calibrating source including losses in optical path due to reflection and transmission in different optical components such as, collimating lens, beam splitters, interference filters and response of photo detectors. For the RP, the calibration determines the factor which indicates the amount of radiance at the input of the system required to generate unit output voltage. Unit of calibration factor for the system is given as radiance per unit volts, i.e., watt per square meter per unit wavelength per unit solid angle per unit volts ($\text{Wm}^{-2}\text{nm}^{-1}\text{sr}^{-1}\text{V}^{-1}$). For the calibration of the RP, a standard radiation source with well characterized output radiance is used.

In present case, the standard source used is 250 W/24 V Quartz Tungsten Halogen (QTH) lamp from M/s. Sciencetech. The QTH lamp along with its housing and power supply is calibrated by M/s. Optikon Corporation using standards traceable to the National Institute

Table 3.1: Calibration Values for Four Channels of RP using Calibrated QTH Lamp

Channel	1	2	3	4
Wavelength (nm)	532±5	600±5	700±6	750±6.5
Light Intensity (W/sr/m²)	1.309 x 10 ¹²	1.717 x 10 ¹²	2.107 x 10 ¹²	2.205 x 10 ¹²
Output Signal (V)	0.0424	0.0248	0.103	0.0472
Calibration Value (W/sr/m²/V)	3.087 x 10 ¹³	6.923 x 10 ¹³	2.045 x 10 ¹³	4.671 x 10 ¹³

of Standards and Technology (NIST). The lamp is supplied with the measured radiance data from 380 nm to 1068 nm in the interval of 4 nm with a colour temperature of 3528 K.

During calibration process, the image of entire QTH lamp filament was made to fall completely within the active area of the photodiodes in each channel. The continuous radiation of the lamp is chopped and the voltage values have been obtained from the oscilloscope record. Calibration is carried out in presence of the same components as used in actual experiments. The calibration factor of each channel has been calculated by dividing the spectral radiant intensity of the calibrated QTH lamp by the recorded voltage signal of each channel. Table 3.1 shows the calculated calibration factors for the aligned RP. It should be noted that the calibration value thus provided in table 3.1 is for particular setup and may change upon changing the setup for different experimental configuration.

3.6 Development of Code for Estimation of Temperature and Emissivity

The measured $I(\lambda)$ at various wavelengths along with the knowledge of the value of C_1 and C_2 , can be used to estimate the best fit values of the unknown parameters, *i.e.*

temperature and emissivity, in Planck's law. The present instrument is developed for the measurements of the radiance at four different wavelengths. These measurements generate four pair of measured intensity-wavelength data. The non linear least square fit of these data is used to estimate the value of the unknown temperature and emissivity. In the next section, a general purpose least square method for parameter optimization for a non linear function is developed, and this method is applied to estimate temperature and emissivity by performing least square fit of the radiation intensities to the Planck's law.

3.6.1 Theory of Least Square Method for Parameter Estimation

The fundamental concept of parameter estimation involves the determination of optimal values of parameters (temperature and emissivity in present case) for a numerical model (Planck's radiation law in present case) that predicts dependent variable outputs ($I(\lambda_i)$) of a function, based on observations of independent variable (λ_i) inputs. The least squares criterion [119] (Gauss-Newton method) minimizes the sum of squares of residuals between measured outputs ($I(\lambda_1)$ to $I(\lambda_4)$) and output values of the numerical model ($I^0(\lambda_1)$ to $I^0(\lambda_4)$) that are predicted from the values of independent variables and estimated parameters. In the following discussion least square solution is presented for the system where model parameters that need to be estimated are linearly related to the model output and then approach was presented to convert non linear model (like Planck's law in present case) to the linear one where theory of linear least square can be applied.

One of the important parts of the technique is that the original non linear function is converted to approximate linear function using Taylor series expansion. Least-square theory is then, used to obtain new estimate of the parameters that move in the direction of minimizing squares of residual.

The general least square model for a function is given as:

$$y = a_0x_0 + a_1x_1 + a_2x_2 + \dots + a_mx_m + e \quad (3.5)$$

Where $x_0, x_1, x_2 \dots x_m$ are the observations of independent variables, $a_0, a_1, a_2 \dots a_m$ are parameters to be estimated, on which function is linearly dependent and y is the measured output of the system. Also e is the error vector which represents deviation in the model parameters and measurement data (measurement noise). Since sources of these errors are many, for ease of simplicity of calculations and applying central limit theorem, these errors are assumed to have Gaussian distribution. In matrix notation the Equ. 3.5, can be expressed as

$$\{Y\} = [Z]\{A\} + \{E\} \quad (3.6)$$

Where $[Z]$ is the matrix of the measured values of the independent variables,

$$[Z] = \begin{bmatrix} x_{01} & x_{11} & \dots & x_{m1} \\ x_{02} & x_{12} & \dots & x_{m2} \\ \vdots & \vdots & \vdots & \vdots \\ x_{0n} & x_{1n} & \dots & x_{mn} \end{bmatrix} \quad (3.7a)$$

Where m , is the number of variables in the model and n , is the number of data points in the measurement. The column vector $[Y]$ contains the observed values of the dependent variable, the column vector $[A]$ contains the unknown parameters and column vector $[E]$ contains the random noise or residuals respectively,

$$[Y]^T = [y_1 \ y_2 \ \dots \ y_n] \quad (3.7b)$$

$$[A]^T = [a_0 \ a_1 \ \dots \ a_m] \quad (3.7c)$$

$$[E]^T = [e_1 \ e_2 \ \dots \ e_n] \quad (3.7d)$$

The least square formulation for this model requires minimizing the sum of square of the errors which are also called residuals and is defined as

$$S_r = \sum_{i=1}^n e_i^2 = \sum_{i=1}^n (y_{i,measured} - y_{i,model})^2 = \sum_{i=1}^n (y_i - \sum_{j=0}^m a_j x_{ji})^2 \quad (3.8)$$

This sum of square of residues/errors can be minimized by taking partial derivative with respect to each of the coefficients and setting resulting equation equal to zero. The

outcome of the process of minimization for linear equation provides the optimal value of model parameters ($\{A\}$) such as the error/residue in model and measurement are minimal and can be expressed in matrix form as

$$[[Z]^T [Z]]\{\hat{A}\} = \{[Z]^T [Y]\} \quad (3.9)$$

Matrix inverse can be utilize to solve and estimate the parameter values and solution is given as

$$\{\hat{A}\} = [[Z]^T [Z]]^{-1} \{[Z]^T [Y]\} \quad (3.10)$$

The process from Equ. 3.5 to 3.10 gives the solution for the case where parameter vector $[A]$ is linearly related to the model output vector $[Y]$. For the cases where parameter vector $[A]$ is non linearly related to the model output vector $[Y]$, one of the important step of the lest square technique is that the original non linear function is converted to approximate linear function using Taylor series expansion. Least-square theory is then, used to obtain new estimate of the parameters that move in the direction of minimizing squares of residual.

The nonlinear function can be presented as:

$$y_i = f(x_i; a_0, a_1, a_2 \dots) + e_i \quad \equiv \quad y_i = f(x_i) + e_i \quad (3.11)$$

Where y_i is the measured value of dependent variable; $f(x_i; a_0, a_1, a_2 \dots)$ is the function of the independent variable x_i and nonlinear function of parameter a_0, a_1, a_2 and e_i is the random error in measurements and model approximation. These errors are the result of many underlying process having their own distribution. Since the aim of study is to minimize the overall error due to combined effect of all sources using nonlinear least square method and not to characterize different sources of error with their individual characteristics, these errors are lumped together and assumed to have Gaussian distribution. This assumption is to make calculation easier and enables the applicability of Central Limit Theorem.

In the above equation the measured dependent variable is the intensity, independent variable is wavelength, and function is having a form of Planck's law with non linear

dependence on two parameters (temperature and emissivity) as shown in Equ. 1.10. The Taylor series expansion of Planck's radiation law (a non linear function) curtailed after first derivative can be written as:

$$I^0(\lambda_i)_{j+1} = I^0(\lambda_i)_j + \frac{\partial I^0(\lambda_i)_j}{\partial \varepsilon} \Delta \varepsilon + \frac{\partial I^0(\lambda_i)_j}{\partial T} \Delta T \quad (3.12)$$

Where j is present intensity, $j + 1$ is next prediction, $\Delta \varepsilon$ is $(\varepsilon_{j+1} - \varepsilon_j)$ and ΔT is $(T_{j+1} - T_j)$

Equation 3.11 is the linearised model of the Planck's radiation law with respect to two parameter *i.e.* temperature and emissivity. Equation 3.12 can be combined with Equ. 3.11 to give functional form where least square method can be applied

$$I(\lambda_i) - I^0(\lambda_i)_j = \frac{\partial I(\lambda_i)_j}{\partial \varepsilon} \Delta \varepsilon + \frac{\partial I(\lambda_i)_j}{\partial T} \Delta T \quad (3.13)$$

Where $I(\lambda_i)$ is the measured value of the radiance for different wavelengths and $I^0(\lambda_i)$ is the calculated model output values using Planck's radiation law at different wavelengths. The Equ 3.13 can be compared with the linear mode presented in Equ 3.5 and can be written in matrix form as shown in Equ. 3.6. The matrix form of Equ. 3.13 is given as:

$$\{D\} = [Z_j] \{\Delta A\} \quad (3.14)$$

where:

$$[Z_j] = \begin{bmatrix} \frac{\partial I(\lambda_1)}{\partial \varepsilon} & \frac{\partial I(\lambda_1)}{\partial T} \\ \frac{\partial I(\lambda_2)}{\partial \varepsilon} & \frac{\partial I(\lambda_2)}{\partial T} \\ \vdots & \vdots \\ \frac{\partial I(\lambda_i)}{\partial \varepsilon} & \frac{\partial I(\lambda_i)}{\partial T} \end{bmatrix}$$

$$\{D\} = \begin{Bmatrix} I(\lambda_1) - I^0(\lambda_1) \\ I(\lambda_2) - I^0(\lambda_2) \\ \cdot \\ \cdot \\ \cdot \\ I(\lambda_i) - I^0(\lambda_i) \end{Bmatrix} \quad \text{and} \quad \{\Delta A\} = \begin{Bmatrix} \Delta \varepsilon \\ \Delta T \end{Bmatrix}$$

Applying least square theory to the Equ. 3.14 gives the solution as:

$$[Z_j]^T [Z_j] \{\Delta \hat{A}\} = [Z_j]^T \{D\} \quad \text{or} \quad \{\Delta \hat{A}\} = \left[[Z_j]^T [Z_j] \right]^{-1} \left\{ [Z_j]^T \{D\} \right\} \quad (3.15)$$

The above equation can be solved for the $\{\Delta \hat{A}\}$, which can be employed to compute the refined estimate for the parameter as:

$$\hat{T}_{j+1} = T_j + \Delta \hat{T} \quad \text{and} \quad \hat{\varepsilon}_{j+1} = \varepsilon_j + \Delta \hat{\varepsilon} \quad (3.16)$$

The above procedure is repeated until convergence is achieved. The criteria for convergence chosen for the parameter estimation is minimization of sum of square of residuals/errors between measured outputs ($I(\lambda_1)$ to $I(\lambda_4)$) and output values of the numerical model ($I^0(\lambda_1)$ to $I^0(\lambda_4)$) that are predicted from input observations, i.e. the minimization of $\{D^2\}$. This convergence criteria is also called minimization of chi-square (χ^2). The value of χ^2 is given as:

$$\chi^2 = \{D^2\} = \left\{ [I(\lambda_1) - I^0(\lambda_1)]^2 + [I(\lambda_2) - I^0(\lambda_2)]^2 + \dots + [I(\lambda_i) - I^0(\lambda_i)]^2 \right\} \quad (3.17)$$

The process of parameter estimation is an iterative process. During the process, the parameter to be estimated (temperature and emissivity) are adjusted such that the value of χ_{j+1}^2 , is less than the value of χ_j^2 . When the value of χ^2 is less than the tolerance criteria value, the process of iteration completes and the parameter values corresponding to the iteration is the final result of the least square process.

The difference between linear and non linear least square estimates is that the non linear estimates are computed using iterative optimization where as linear estimates using

least square techniques are compact solutions. The use of iterative procedures requires providing starting values for the unknown parameters before the optimization can be carried out. The starting values should be reasonably close to the actual value otherwise the optimization procedure may not converge. In the next section one such method of Levenberg-Marquardt is described to achieve convergence at all points.

3.6.2 The Levenberg-Marquardt Method

As described in earlier section, in a non linear least square fit, the minimization of error *i.e.* χ^2 , is carried out iteratively. The aim of the iteration is to find the update ($\{\Delta A\}$) for the estimation of parameters *i.e.* temperature and emissivity, which minimizes the error (χ^2). The two of the common methods of generating updates are the Gradient Descent method and the Gauss-Newton method. The gradient descent method is a first-order iterative optimization algorithm for finding the minimum of a function. The local minimum of a function is obtained by taking steps proportional to the negative of the gradient of the function at the current point. This method is slow near the minimum due to its asymptotic rate of convergence. On the other hand Gauss-Newton method which is mainly used to solve non-linear least squares problems has the advantage of second derivative. The solution provided in earlier section (Equ. 3.15) is based on the same method (Gauss-Newton method). The limitation of this method is that the convergence to the solution is slow and many a times it won't converge for cases where initial guess is far from the minimum solution.

To overcome the above limitations the Levenberg-Marquardt method introduces a scaling parameter ζ , which adaptively switches the updates ($\{\Delta \hat{A}\}$) during iteration between gradient descent method and Gauss-Newton method. The update equation for the same is given as

$$[[Z_j]^T [Z_j] + \zeta J] \{\Delta \hat{A}\} = \{[Z_j]^T \{D\}\} \quad (3.18)$$

Where ζ , is the scaling parameter and J is the identity matrix. In the case when the minimum of solution is far, the value of ζ is large and system of update equation (Equ. 3.17) is equivalent to gradient descent method which provide steady and convergent progress toward the solution. On the other hand when solution approaches the minimum, the value of ζ is small and the Levenberg-Marquardt method approaches the Gauss-Newton method, and the solution typically converges rapidly to the local minimum [120-122]. The advantage of Levenberg-Marquardt method is fast and guaranteed convergence.

3.6.3 Code Development

For estimation of the fitted parameters using the general least square method with Levenberg-Marquardt method described above, a computer code has been developed. The code accepts various inputs for forming matrices $[Z_j]$, $\{D_j\}$ and $\{\Delta A\}$. These inputs are number of measurement points (number of wavelengths in measurement), there values (measured spectral radiance) and number of parameters to be estimated. The order of $[Z_j]$ matrix is $m \times n$, where m is the number of channel in the system while, n is the number of parameters to be estimated. For present case the order of $[Z_j]$ matrix is 4×2 . Similarly the order of $\{D_j\}$ is $m \times 1$, where m indicates the same value as in case of $[Z_j]$ and the order of $\{\Delta A\}$ is 2×1 for two parameter estimation.

One of the input to the code is the initial estimates for the two parameters *i.e.* temperature and emissivity. These inputs are used to perform first iteration and from there on the program itself finds out the next iteration value. To find out the next iteration value Equ. 3.18 need to be solved for $\{\Delta A\}$ using initial estimation of parameters. The newly computed values of $\{\Delta A\}$ are combined with the initial estimate of the parameters using Equ. 3.16. These obtained values of parameter estimate are used to calculate χ_{j+1}^2 which is compared with the χ_j^2 values using initial estimate. If the value of $(\chi_{j+1}^2 - \chi_j^2)$ is positive then the newly

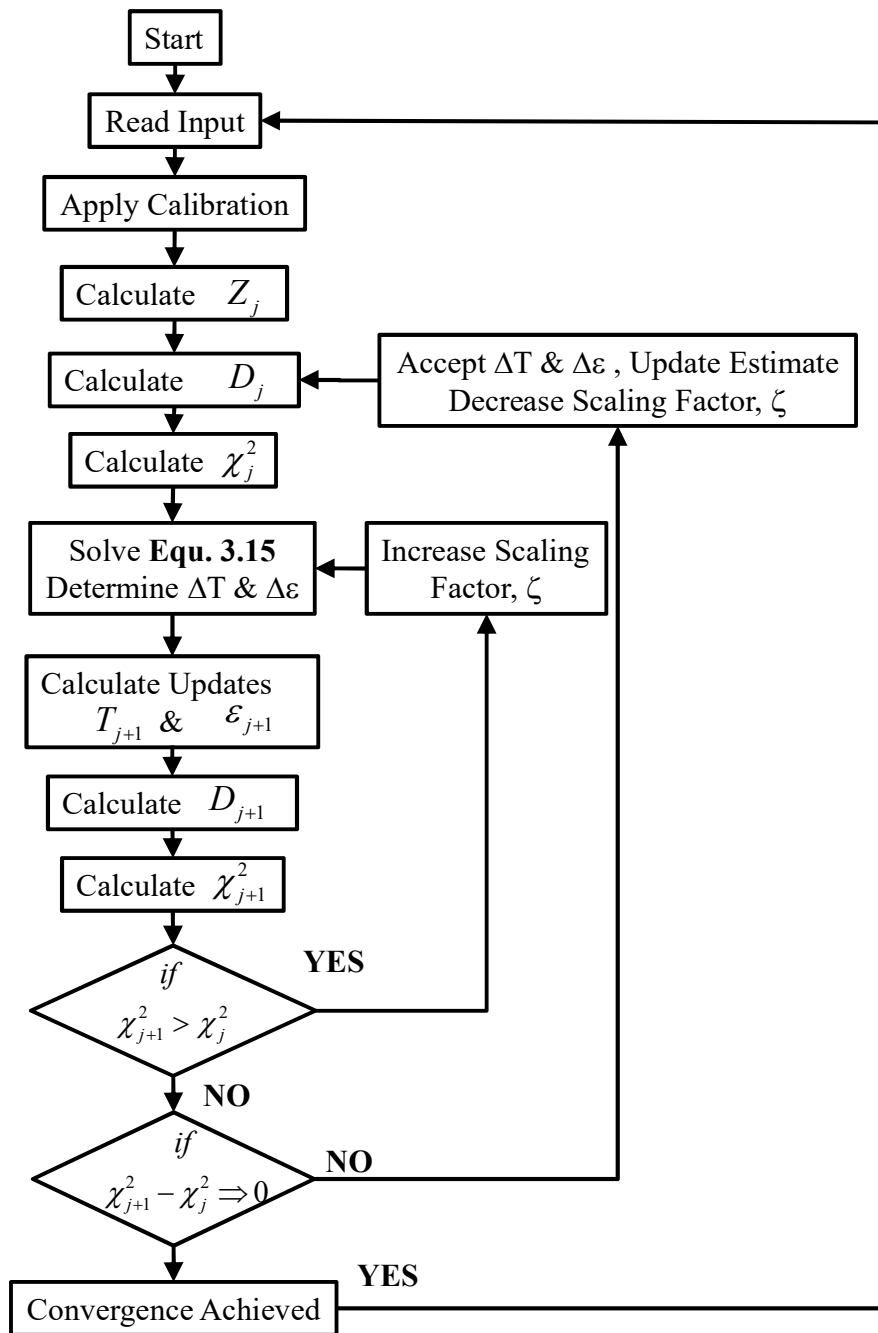


Figure 3.6(a): Logical Flow chart of the developed code

estimated parameters are not updated but the value of scaling factor ζ is increased by a constant factor. New iteration will start with the old estimate but with new value of scaling parameter. On the other hand if the value of $(\chi_{j+1}^2 - \chi_j^2)$ is negative then the newly estimated parameters are updated and they will be treated as new initial estimate for next iteration. Along with that the value of scaling parameter is reduced by constant factor. This iteration

1. Read data
2. Apply calibration
3. Assume initial estimate of temperature T and emissivity ε
4. Calculate the Z_j matrix by using wavelength λ_i and estimates of the temperature T and emissivity ε
5. Calculate vector D_j by using wavelength λ_i and estimates of the temperature T and emissivity ε
6. Calculate vector χ_j^2 by squaring and adding all the elements of the vector D_j
7. Solve the Equ. 3.15 and update for temperature and emissivity as ΔT and $\Delta \varepsilon$
8. Calculate updates in temperature and emissivity as T_{j+1} and ε_{j+1}
9. Calculate vector D_{j+1} by wavelength λ_i and updated estimates of the temperature T_{j+1} and emissivity ε_{j+1}
10. Calculate vector χ_{j+1}^2 by squaring and adding all the elements of the vector D_{j+1}
11. IF vector χ_{j+1}^2 is greater than vector χ_j^2 ,
 THEN increase scaling factor ζ , and repeat calculation from step 7 through 10
12. ELSE IF vector χ_{j+1}^2 is less than vector χ_j^2 ,
 THEN accept updated value of temperature T_{j+1} and emissivity ε_{j+1} , decrease the value of scaling factor ζ , also repeat the iteration from step 4 through 12 till convergence achieved
13. IF difference between vector χ_{j+1}^2 and χ_j^2 is close to zero,
 THEN convergence is achieved and estimate of temperature and emissivity is available as T_{j+1} and ε_{j+1}
14. Go through step 1 to step 13 for next data point

Figure 3.6(b): Steps as pseudo code for estimating parameters

process is repeated until the values of $(\chi_{j+1}^2 - \chi_j^2)$ become close to zero within the acceptable limit. The logical flow chart of the process of iteration is shown in Fig. 3.6(a) corresponding steps of the iteration is presented in Fig. 3.6(b)

3.6.4 Uncertainty Calculation

The uncertainty in the estimation of temperature and emissivity due to system parameters such as error in voltage measurement, bandwidth of filters, variation in temperature of the calibration source etc., have been estimated using procedure given below.

$$\Delta I = \frac{\partial I(\lambda_i)}{\partial T_m} \Delta T_m \quad \text{and} \quad \Delta I = \frac{\partial I(\lambda_i)}{\partial \varepsilon_m} \Delta \varepsilon_m \quad (3.19)$$

Rearranging above equations gives:

$$\Delta T_m = \left(\frac{\partial I(\lambda_i)}{\partial T_m} \right)^{-1} \Delta I \quad \text{and} \quad \Delta \varepsilon_m = \left(\frac{\partial I(\lambda_i)}{\partial \varepsilon_m} \right)^{-1} \Delta I \quad (3.20)$$

Where ΔT_m is the uncertainty in the temperature estimation; $\Delta \varepsilon_m$ is the uncertainty in the emissivity estimation; T_m and ε_m is the estimated temperature and emissivity; ΔI is the uncertainty in the measured intensity; $\partial I(\lambda_i)/\partial T_m$ is the derivative of radiation law at estimated temperature; and $\partial I(\lambda_i)/\partial \varepsilon_m$ is the derivative of radiation law at estimated emissivity;

Analytically the measured intensity is given as:

$$I = \frac{V_m}{V_{cal}} * C_1 \lambda_i^{-5} \left(e^{C_2 / \lambda_i T_{cs}} - 1 \right)^{-1} \quad (3.21)$$

where V_m is the measured voltage during actual temperature measurement; V_{cal} is the voltage measured at the time of calibration; and T_{cs} is the temperature of the calibration source. Using the relation given in Equ. 3.20 the uncertainty in the measured intensity at each channel due to system parameters such as error in voltage measurement, bandwidth of filters, variation in calibration source temperature etc. can be estimated as follows:

$$\Delta I = \frac{\partial I(\lambda_i)}{\partial T_{cs}} \Delta T_{cs} + \frac{\partial I(\lambda_i)}{\partial V_{cal}} \Delta V_{cal} + \frac{\partial I(\lambda_i)}{\partial V_m} \Delta V_m + \frac{\partial I(\lambda_i)}{\partial \lambda_i} \Delta \lambda_i \quad (3.22)$$

The value of ΔI is calculated for each channel at the calibration source temperature using the measured voltage V_m at the respective channel in the actual experiment. The final uncertainty in the estimated temperature and emissivity is calculated using Equ. 3.20, where

the partial derivative of Planck's law is computed at the estimated temperature and emissivity.

3.7 Experimental Validation

The performance of the RP has been validated by measuring the temperature of the standard radiation source, Tungsten Halogen Light Source (THLS). The measurement of steady state temperature using THLS is important for verifying the measurement procedure and the estimation of the possible uncertainties in the measurement. After validation of the instrument, it has been used to carry out time resolved temperature measurement of the electrically exploding wires.

3.7.1 Validation using Standard Radiation Source

The above described RP and computer code has been tested by measuring the temperature of the standard radiation source, Tungsten Halogen Light Source (THLS) whose temperature is well characterized independently. The radiation from the source is collected by the light collection system of the RP and divided into four channel using beam splitters inside the RP. Each channel passed only one of the four wavelengths i.e. one of the 532, 600, 700 or 750 nm and converted the radiation intensity into the equivalent electrical signal using photo-receiver. Output of these receivers has been recorded on the digital storage oscilloscope. The recorded data is analyzed using the developed computer code. The temperature of THLS estimated from measured radiation turns out to be 3009 K as compared to the specified value of 2850 K, in agreement with the specified value within ~5.5%. Table 3.2 shows the uncertainty in the measurement using Equ. 3.20.

As shown in the Table 3.2 the calculated uncertainty in the measured temperature of the light source is ~ 3.1% while that in the emissivity is ~ 24%. Due to the week dependence

Table 3.2: Calculated Error or uncertainty in the static temperature estimation

Parameter	532 nm	600 nm	700 nm	750 nm	Remark	
ΔT_m (°K)	93.39	102.58	94.98	88.98	Average ΔT_m is 94.98	3.1 % of the measured value
$\Delta \varepsilon_m$	0.278	0.271	0.2156	0.189	Average $\Delta \varepsilon_m$ is 0.238	23.8% of the measured value

of spectral radiance on emissivity in Planck's law, the emissivity is poorly constrained by spectral radiance data. However, strong dependence of spectral radiance on temperature leads to relatively small uncertainties in temperature measurement [9]. The quality of the least square fit is shown in the Fig. 3.7. The plot shows four measured spectral radiance from the THLS. It represents the best fitting grey body function with $T = 3009$ K.

3.7.2 Time Resolved Temperature Measurement of Electrically Exploding Wire

Figure 3.8 displays the experimental layout of capacitor bank used for exploding

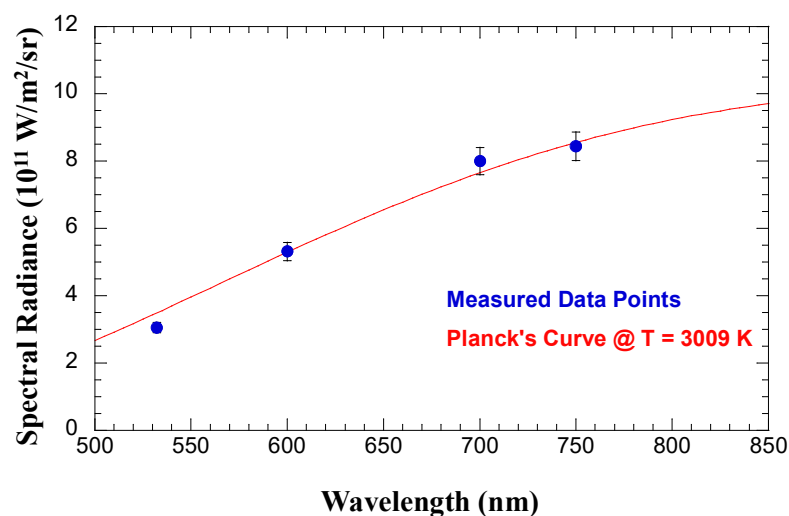


Figure 3.7: Plot of spectral radiance measured with the best fitting gray body curve corresponding to $T=3009$ K

conductors [11]. The capacitor bank used for the experiments has a capacitance of $8\mu\text{F}$ with a capacity of delivering peak current of $\sim 70\text{ kA}$ within 750 ns to the load. In this experiment a current of 4.6 kA generated by this capacitor bank charged up to 3.8 kV is fed in to a thin metallic conductor (copper wire in this case) through transmission line. The total circuit inductance, which involves the inductance of capacitor bank, triggered spark gap switch, and transmission line was maintained as low as possible. A pick-up loop has also been used for the measurement of the current (I) and its time derivative (dI/dt).

On discharge of capacitor through the wire, the wire heats up due to ohmic effect, its resistance goes up and on further heating the wire turns to molten state and then to vapor state. Throughout this heating process the resistance of the wire keeps on increasing. The process occurs so fast that inertia prevents it from expanding. Finally the large current through the dense vaporized material further heats it and this material finally expands explosively. The time at which it expands explosively is called burst time. At this time the current derivative profile shows a sharp dip and the wire material is expected to reach its

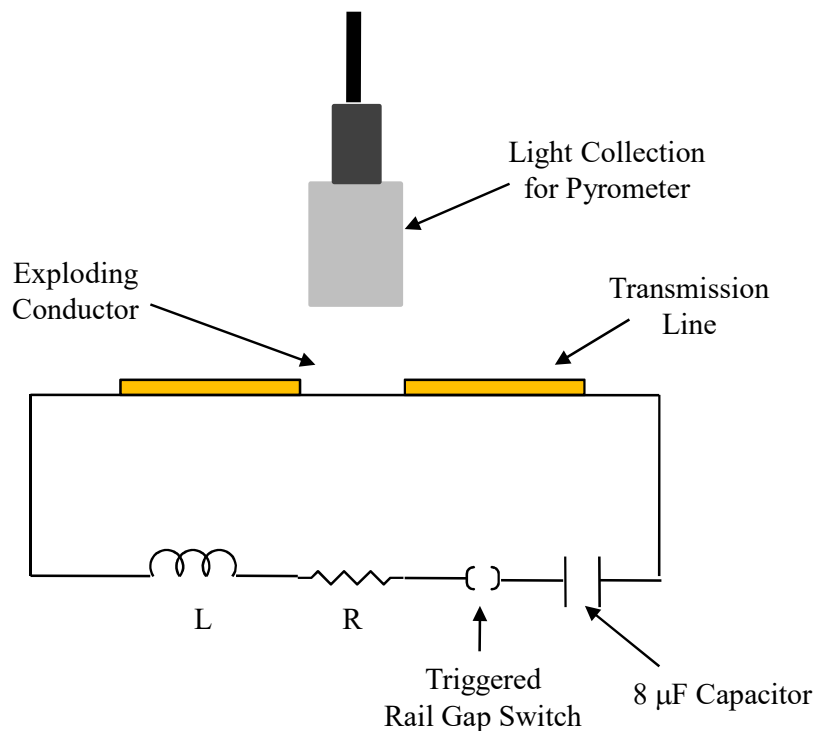


Figure 3.8: Experimental setup for exploding wire

maximum temperature. Once the vaporized material starts expanding, its temperature is expected to fall. As an electrical arc is established through the metallic vapor, the resistance drops and the current increases further, heating the material. This phenomenon is called ‘Re-striking’. The temperature profile after the burst time depends on the competition between the resistive heating of the wire material and its cooling due to expansion.

This experimental setup has been used to study the temperature profile of the electrically exploding wire employing the developed RP. Two experiments were performed using copper wire of length 10 mm and diameter $77\mu\text{m}$. The intensity of radiant energy measured using RP setup at four wavelengths (532, 600, 700 and 750 nm) during experiment were recorded on oscilloscope. The oscilloscope records the data at the sampling rate of 5 GS/s per recording channel for the total duration of few microseconds. This makes the data size of about 5000 data points for one microsecond for one channel (i.e. at one wavelength). These recorded data were analyzed offline using developed code.

The transient temperature profile of the copper wire derived from the measured radiation data at four different wavelengths in first experiment is shown in the Fig. 3.9. Along

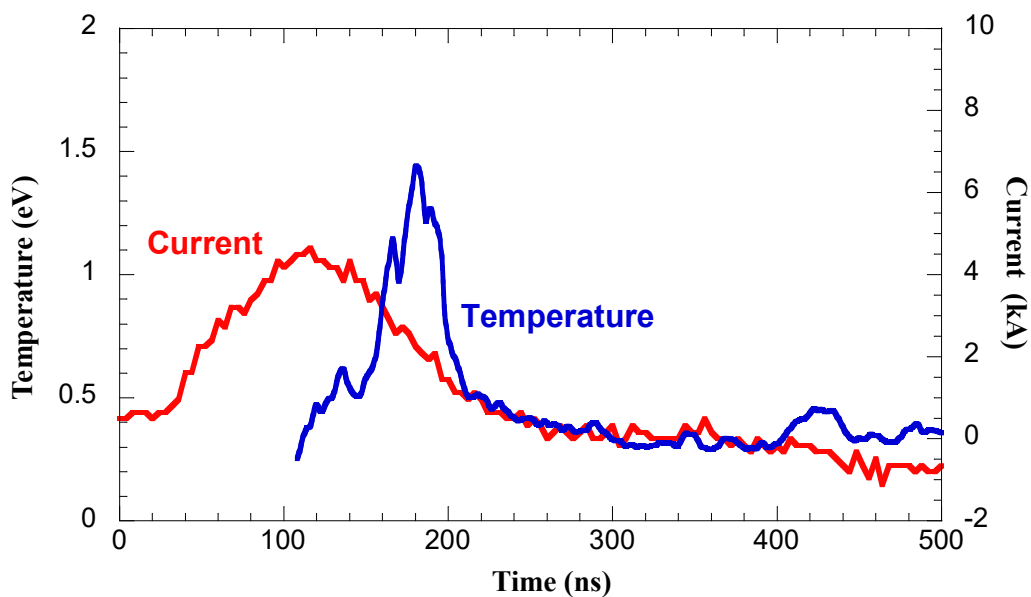


Figure 3.9: The estimated temperature profile of the exploding copper wire along with the measured current during first experiment.

with the temperature profile, the current signal measured using single turn pick-up loop is also presented in the same figure [11]. The current waveform reaches to the burst current of ~ 4.5 kA for the wire around 100 ns after start. Around burst time the temperature starts increasing and reaches to the peak value of ~ 1.5 eV in a time interval of 70 ns after burst. As shown in Fig. 3.9, at ~ 150 ns after burst (or at ~ 250 ns absolute time) the measured temperature profile reaches a stable value of 0.3 eV when current approaches to zero value. This value of peak temperature is comparable with the measured value available from other sources [123].

The current and corresponding temperature profile of the exploding wire in the second experiment is displayed in Fig. 3.10. In line with the previous experiment the current waveform reached burst current of ~ 4.5 kA for the wire around 100 ns after start. Around burst time the temperature starts increasing and reaches the peak value of ~ 1.35 eV in a time interval of 40 ns after burst. In this experiment, an interesting feature of current re-striking has also been observed after ~ 140 ns of start of current. This current re-striking has further increased the otherwise falling temperature of the exploding wire and lead to second peak of

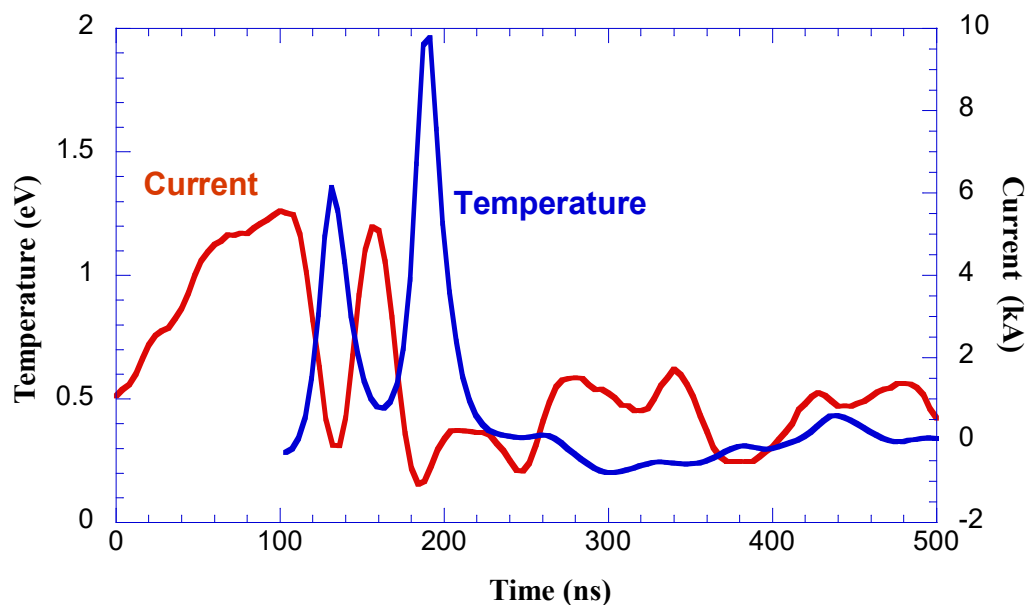


Figure 3.10: The estimated temperature profile of the exploding copper wire along with the measured current during second experiment.

temperature of ~ 1.96 eV at ~ 190 ns from the start of current. The reason for this behavior of the wire could be the instability of the vapour phase of the wire. After the first burst the wire may not have been converted fully to the vapour phase and the energy present in the capacitor bank supplied to the combined mixture of vapour and molten metal forces to start conducting the current again.

The measurement of transient temperature generated in these experiments has been useful in verifying the dynamic range and time response of the RP before it could be used in shock wave experiments. Dynamic range is important to quantify the peak temperature that can be measured in a particular configuration while time response is important for identifying how fast varying temperatures can be measured using the developed RP.

3.8 Summary

RP has been developed for the measurement of transient temperatures (rise time \sim few tens of nanoseconds) generated during dynamic compression or sudden deposition of thermal or electrical energy into the materials. The developed RP equipped with photo-receivers having dynamic bandwidth of 125 MHz has capability of measuring transient temperature with time resolution of about 3 ns. In order to estimate temperature, the instrument records the radiation intensities at four wavelengths. The estimation of temperature and emissivity (grey body assumption) is carried out using developed Levenberg-Marquardt method. It has been demonstrated that present instrument make steady state temperature measurement with an accuracy of $\sim 5\%$. The developed RP has been used for time resolved measurement of temperature having rise time or the fall time of the order of ~ 15 ns. Also, the optical design of the RP is kept compact so as it can be used as portable instrument.



Chapter 4

Characterization of Signal Recording System used in VISAR

4.1 Introduction

As mentioned in earlier chapters also, in shock loading experiments, materials are subjected to high pressures for a very short duration (a few ns to a few μ s) with rise time varying from a fraction of nanosecond to a few tens of nanoseconds depending upon the experimental method. Plate impact is one of the several methods of generating shock pressures in materials [36-39], where one of the continuum measurements used to characterize a state of material is the history of its free surface velocity. The optical interferometric based techniques such as VISAR are frequently used for such measurements [24, 27, 28]. Output of VISAR is in the form of time varying electrical signals which are finally converted to time varying free surface velocity by employing the calibration, signal processing and estimation methods.

To derive in-situ behaviour of physical properties of interest from recorded electrical signals in such experiments, it is desirable that (i) the variation of output of the SRS is linear with respect to the input and (ii) the output of SRS should have sufficient SNR to extract the meaningful information. In view of the importance of knowledge of various characteristics of SRS, it is essential to determine its suitable range of operation prior to use in such applications. To our knowledge, no such procedure for characterization of SRS of VISAR instrument is reported in literature. Therefore, in present chapter, a procedure has been developed to identify relevant parameters ensuring that the SRS used in VISAR system in

shock experiments operates in the linear region with desirable gain and SNR. This generic procedure so developed, for identifying the suitable operating range of SRS for VISAR interferometer could be utilized as guideline in similar systems having different optical components and optical detectors.

4.2 VISAR and its Signal Recording System

VISAR is a modified Michelson interferometer which measures the differential Doppler shift as a function of time, by modulating/beating two light signals reflected from a moving free surface, at two time instants separated by a few nano-seconds [24, 27, 28]. Upon interference, the VISAR generates steady fringe pattern if there is no movement of surface or there is movement with constant velocity else the fringe shifting takes place. These shifts in fringes are converted into measurable sinusoidal electrical signal using SRS which consists of input aperture, imaging optics, photo detector (PMT in present case), load resistance (50 Ω) and high digital storage oscilloscope (DSO). The SRS optically images the fringes on to the PMT. The output current of PMT is converted into an equivalent voltage signal by adding a load resistance in output circuit. The voltage drop across load resistance is recorded on a DSO (bandwidth of 1 GHz and sampling rate of 5 GS/s). VISAR generates two fringe patterns in quadrature which are recorded as two different sinusoidal signal separated by a phase of $\pi/2$ [75]. Each of these signals has in turn two parts one is the constant offset and other is the sinusoidal function (i.e. time dependent amplitude). The constant offset contains information about the initial phase [115]. This constant offset is also the result of background and dark current present during measurement. Further information about the change in velocity of the moving surface is encoded in the phase of the sinusoidal function i.e. second part of the signal. Linear operation of PMT is important to determine accurate phase from the

amplitude (constant offset as well as time varying amplitude) information of the recorded electrical signal and in turn estimation of velocity of the moving surface.

As explained earlier also and repeated here for continuity, PMT as such is a very sensitive optical detector where photons falling on the cathode generate photoelectrons. These photoelectrons are amplified inside the tube through the process of secondary emission in series of dynodes. The amplified electron current corresponding to photons falling on cathode is collected at anode terminal. This output current of PMT i.e. anode current is generally assumed to be linear with respect to the input optical intensity and expected to be zero when there is no input light. PMT in general also has large dynamic range of operation corresponding to the input optical signal provided the dark current and background current is kept low, not more than a few nano-amperes. The major sources of error while doing measurement using a PMT are (i) saturation effect (ii) presence of after pulse and (iii) dark current. Very large optical intensity makes PMT response nonlinear due to saturation effect [90-92]. For high intensity optical pulse PMT also exhibits the after pulse [93, 94], where some amount of anode current remains for larger time (\sim few μ s). The presence of dark current increases the anode current significantly leading to reduction in the dynamic range of a PMT.

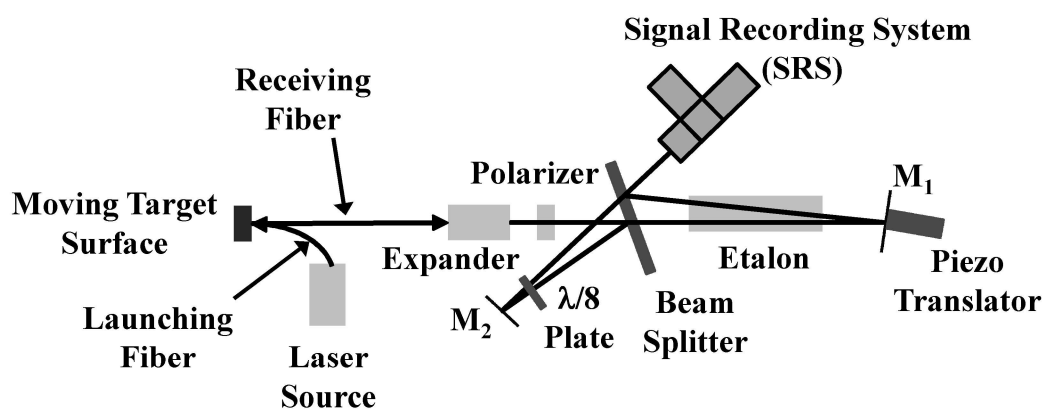


Figure 4.1(a): Schematic of Velocity Interferometer

VISAR signal requires PMT to remain below saturation region with sufficient dynamic range to represent time varying sinusoidal signal linearly. To achieve this desired goal, the complete in-situ optimization of SRS, for coupled optical power and for PMT operating parameters, is essential.

4.3 VISAR Output and Effect of SRS on Output Signal

Schematic of VISAR setup existing in our laboratory [124] is shown in Fig. 4.1(a) and photograph of SRS is shown in Fig. 4.1(b). The output signals of two PMTs are expressed as [115]:

$$V_x = x_0 + A_x \cos \Phi(t) + d(t); \text{ and } V_y = y_0 + A_y \sin(\Phi(t) - \epsilon) + d(t) \quad (4.1)$$

Here x_0, y_0 , respectively, represent the constant amplitude, whereas, A_x, A_y , respectively, correspond to the time dependent amplitude of the two signals. $d(t)$ is the additive white Gaussian noise present in the signal. Typical features of the noise, measured in one of the recorded signal (without any fringe data), showing white Gaussian nature are presented in Fig. 4.2. Figure 4.2(a) represents the output of the SRS recorded on the oscilloscope. It also shows the markers from where the data is selected for verifying white

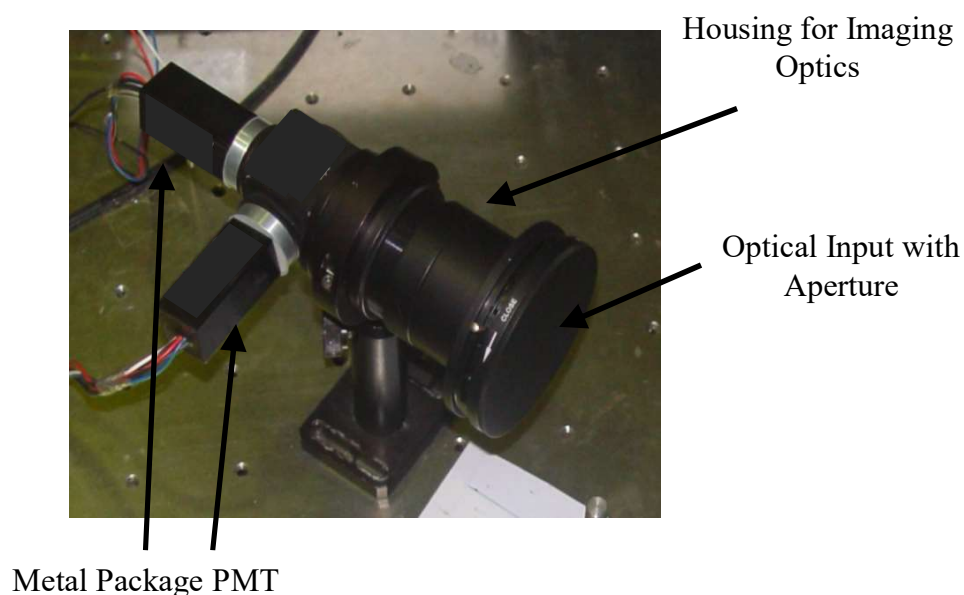


Figure 4.1(b): Photograph of Signal Recording System

Gaussian nature of the noise. The verification of white Gaussian nature of noise is carried out using graphical methods, as elaborated statistical test methods are not the scope of this work. But since the information about noise model is important for further studies, the white Gaussian nature of noise is established using simple and accurate graphical tools. Figure 4.2(b) shows the histogram along with the Gaussian distribution plot. The properties of histogram plot like mean of data samples and Gaussian distribution is same, plot is symmetric about the mean and samples within $\pm 3\sigma$ covers almost 99% of total data samples indicates that the measured data is Gaussian. Fig. 4.2(c) represents the Q-Q (quantile-quantile) plot of the measured data samples. A Q-Q plot is used to compare the shapes of distributions, providing a graphical view of how properties such as location, scale, and skewness are

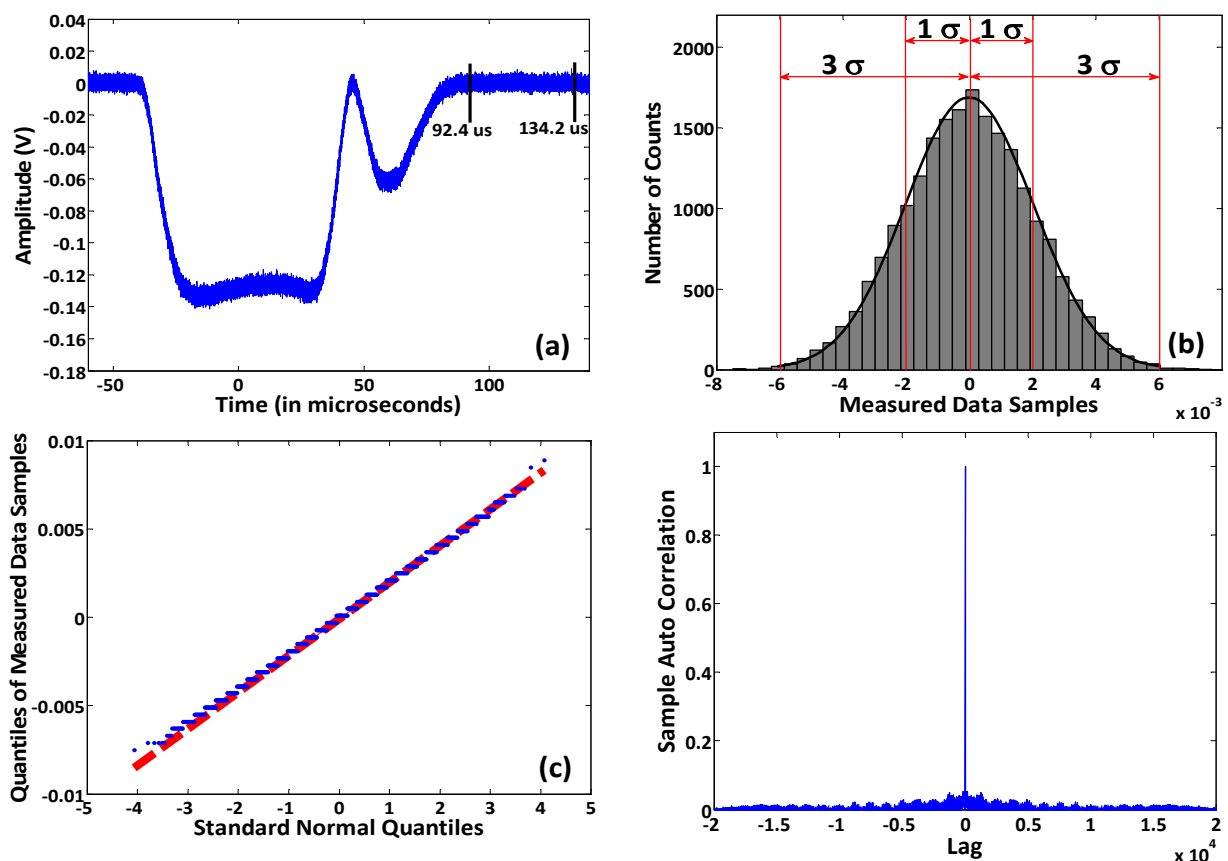


Figure 4.2: (a) Measured signal without fringes; (b) Histogram of selected data with Gaussian distribution; (c) Q-Q plot of measured data samples with samples from standard Gaussian distribution; (d) Autocorrelation of selected data

similar or different in the two distributions. Hence, measure data samples are plotted along with the standard Gaussian (Normal) distribution data in Fig. 4.2(c) for comparing the two distributions. Blue dots in the Fig 4.2(c) are the measured data points whereas red line indicates the samples from the standard Gaussian (Normal) distribution. The non decreasing nature of plot when moving from left to right and data following 45° line indicates that the two data set which are being compared, follows the same distribution. In present case one data set is from measured data samples whereas the second data set is from the standard Gaussian (Normal) distribution. Hence Q-Q plot also indicates that the measured data samples for the noise are from the Gaussian distribution. Figure 4.2(d) represents the autocorrelation of the noise samples. Single peak at zero lag indicates whiteness or randomness present in the noise samples. Hence sequence of figures from Fig 4.2(b) to Fig. 4.2(d) indicates that the noise present in measured data samples follows the white Gaussian distribution. This white Gaussian nature of noise encourages us to use alternate definition of SNR. In present studies SNR is determined by calculating mean of the recorded signal (signal amplitude) and variation (noise part) around that mean value. The SNR is thus calculated as the ratio of mean and variation (standard deviation) of the recorded signal. The standard relation used for the calculation of SNR in dB is:

$$SNR_{dB} = 20 \times \log_{10} \left(\frac{\mu}{\sigma} \right) \quad (4.2)$$

where, μ is the mean value and σ is the standard deviation of the Gaussian distribution of noise.

Further, Equ. 4.1 indicates that the outputs of two detectors are sinusoidal function of $\Phi(t)$ with an offset of x_0 and y_0 , respectively when fringes are generated due to target movement. The constant offsets x_0 and y_0 present in the signals (Equ. 4.1) are due to the non-coherent portion (reflected laser power as well as background light) of the optical signal coupled to SRS whereas the components A_x and A_y are due to coherent portion of the optical

signal. The coherent part of the optical signal determines contrast (also called fringe visibility) of the measured fringes. The fringe contrast may be defined as follows [115]:

$$C_0 = \frac{V_{max} - V_{min}}{V_{max} + V_{min}} = \frac{A_x}{x_0} \text{ or } \frac{A_y}{y_0} \quad (4.3)$$

where $V_{max} = x_0 + A_x$ or $y_0 + A_y$ and $V_{min} = x_0 - A_x$ or $y_0 - A_y$

In ideal case where, coherent and non coherent intensities are equal, the fringe contrast is 1, otherwise in practical cases the amount of coherent light is less than the incoherent light hence the fringe contrast is always less than one. Parametrically the Equ. 4.1 represents the family of ellipses with centre at x_0, y_0 , and V_x, V_y are the points lying on the ellipse. Ideally for equal fringe visibility in two quadrature signals, ellipse is reduced to a circle but in practice it is not possible to achieve this condition, hence one gets ellipse. To estimate $\Phi(t)$ from V_x, V_y , being points on ellipse, the ratio of two signals is calculated as:

$$\widehat{\Phi}(t) = \tan^{-1} \left(\tan \epsilon + \frac{V_y - y_0}{V_x - x_0} \frac{A_x}{A_y} \sec \epsilon \right) \quad (4.4)$$

After estimation of $\widehat{\Phi}(t)$, the velocity of the moving surface can be determined [115] using expressions:

$$v(t - \tau/2) = VPF \times F(t) \quad (4.5a)$$

$$VPF = \frac{\lambda_0}{2\tau}, \text{ and } F(t) = N_I(t) + N_F(t) = \frac{\widehat{\Phi}(t)}{2\pi} \quad (4.5b)$$

where, as already mentioned in previous chapter, $v(t)$ is the velocity as a function of time and VPF and $F(t)$ are velocity per fringe constant and fringe count, respectively. VPF depends on the un-shifted laser wavelength λ_0 and instrument delay τ , whereas, $F(t)$ consist of integral number of fringes $N_I(t)$ and fractional fringe $N_F(t)$. Fig. 4.3(a) displays a typical quadrature fringe signal recorded as the output of the SRS used in VISAR setup in one of the plate impact experiment [29]. The corresponding free surface velocity profile derived from it is also displayed in Fig. 4.3(b).

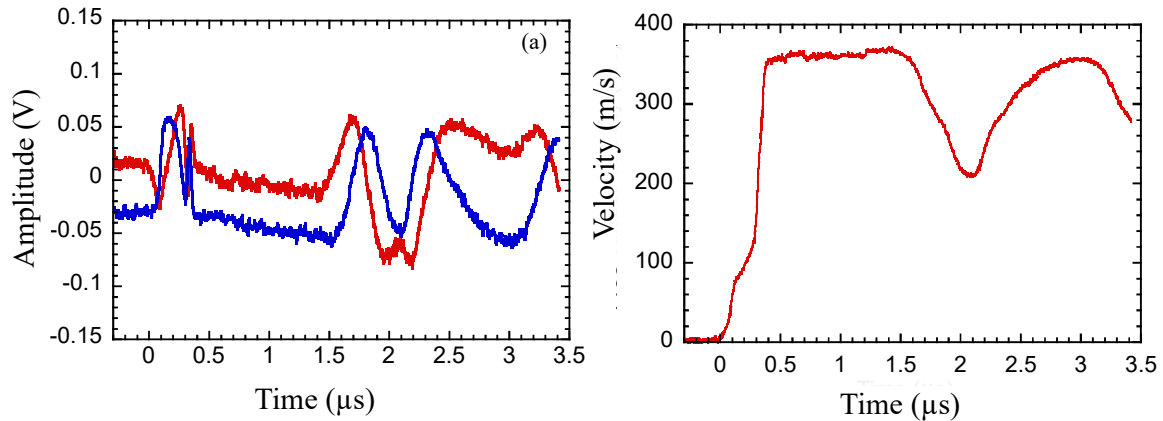


Figure 4.3: (a) Quadrature Fringe; (b) Estimated Velocity in m/s

For accurate determination of phase using Equ. 4.4, it is important to record the signal with high SNR, to avoid false phase jump [99, 100, 124], and large dynamic range (in terms of time as well as amplitude response). When a sensitive detector like PMT is used for recording signal generated using VISAR, the background current corresponding to constant offset reduces dynamic range of PMT in both time as well as amplitude response. If PMT is exposed to this constant offset input for a long time, this (background current) reaches to near saturation region where removal of charges from the anode takes large time and adds to the signal induced noise (thus reducing its SNR) and sluggish time response (compared to fast time dependent amplitude) arising due to Doppler shift in reflected laser light caused by the movement of the target free surface. Apart from reducing the dynamic response (in terms of time), the high average anode current also reduces the margin of operation in linear region (in terms of amplitude response). Although the fringe contrast can be increased by improving the quality (flatness, surface finish etc.) of optical components such as, retardation plate, etalon, mirrors and polarizing beam splitter used in the VISAR, but this is limited by the available manufacturing techniques. Hence, one [95, 96, 97] has to resort to the tools like optimization of coupling of optical power and PMT supply voltage for further improvement in SNR and extending the linear range of operation of SRS.

4.4 Experimental Setup and Measurement

4.4.1 Experimental Setup

A schematic of measurement setup consisting of three parts viz. (I) optical signal generation, (II) VISAR optics and (III) SRS, is shown in Fig. 4.4. For the operation of VISAR a laser source (in present case a diode pumped frequency double solid state single mode CW laser having output at 532 nm with variable power up to 2W) is used to shine the back surface of target. Doppler shifted reflected laser light from the surface is collected & transported to optical setup of VISAR. The same laser has been employed as the optical source in the present setup for characterizing the SRS in terms of linearity and SNR. The output of the laser source is passed through the Pockels cell working on in the principle of electro-optic effect. Pockels cell combined with Polarizer (optical analyzer) is used for switching “NO” optical rotation to “Half Wave” rotation which provides shuttering capability to allow or block the laser light falling on the measurement setup.

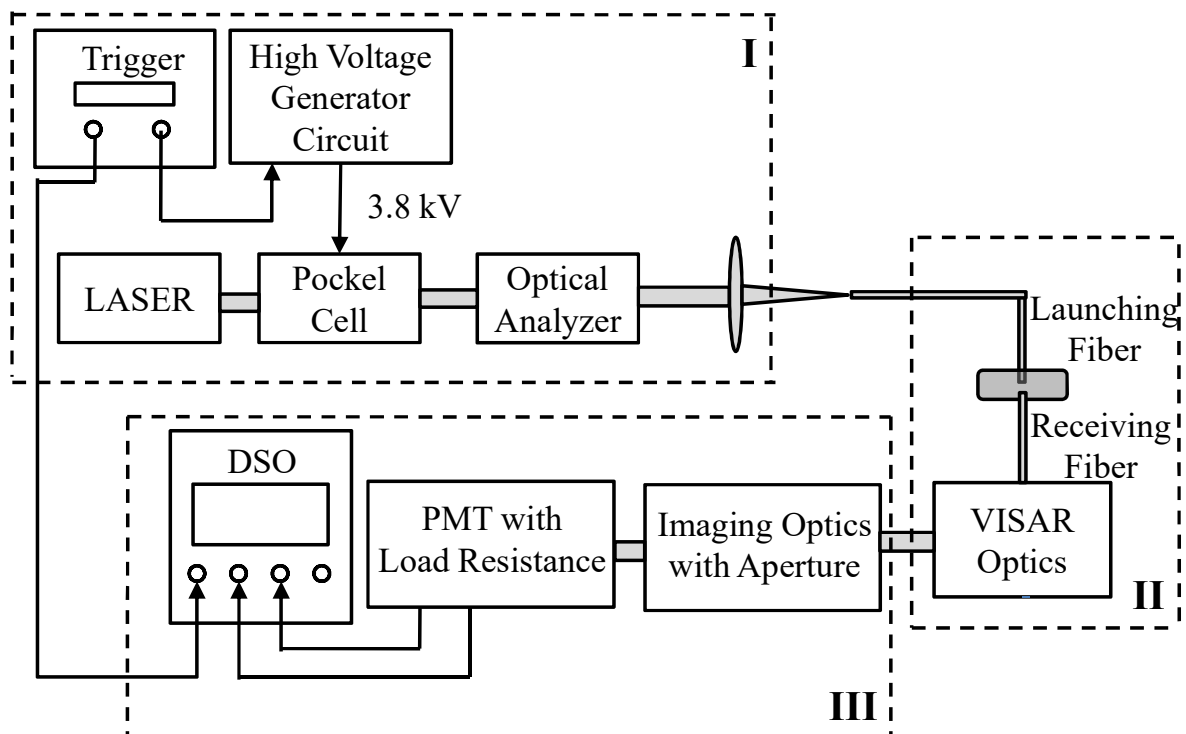


Figure 4.4: Measurement setup for characterization of signal recording system

Table 4.1: Specification of PMT

Parameters	PMT Specification
Spectral Response	230 nm to 920 nm
Photo Cathode	Multialkali (Extended Red)
Window Material	Borosilicate Glass
Input Voltage range	2.8 to 5.5 V
Max average output signal current	100 μ A
Control Voltage Adjustment	0.5 to 1.1 V
Peak Sensitivity Wavelength	630 nm
Cathode luminous sensitivity	500 μ A/lm
Anode Luminous Sensitivity	1000 A/lm
Radiant Sensitivity	1.5×10^5
Rise Time	0.57 ns (at Control Voltage of 1.0 V)

The advantage of Pockels cell is its ability to switch the light very fast (few tens of nanosecond) upon the application of voltage. Since the application of voltage can be controlled by the external trigger signal, the synchronization of time between experimental event and availability of laser source is relatively simpler. All the components i.e. laser source, Pockels Cell, its trigger circuit and optical analyzer form the part one of the measurement setup.

Further as displayed in Fig. 4.4, the second part consists of launching & receiving fibers and VISAR optics. During experiments the coupling between launching and receiving fiber is through target as shown in Fig. 4.1(a), whereas in present case for characterizing SRS these fibers are coupled head on with each other. VISAR Optics (expander, etalon, $\lambda/8$ plate, mirrors etc.) is arranged in same manner as they are used in actual experimental setup as shown in Fig. 4.1(a). The third part of the measurement setup is the signal recording system (SRS) of VISAR. As mentioned in section 4.2, the SRS consist of three parts, first is the imaging optics with aperture, second is the PMT with load resistance and third is DSO. The entrance of the imaging optics is covered with an aperture having minimum opening of 2 mm

and maximum up to of 50 mm. The main objective of placing an aperture is to limit the entry of stray light inside SRS and this in turn helps in controlling background current of PMT.

Imaging optics efficiently images generated fringes on to the photocathode of PMT. A commercially available PMT in the form of single module containing metal package PMT and high voltage power supply circuit is used in present setup. Typical specifications of the PMT are noted in table 4.1. The gain of PMT is controlled by applying a voltage in the range from 0.5 V to 1.0 V. Output current of PMT is converted to an equivalent voltage signal by using a load resistance of 50 Ω in the circuit. This voltage drop is recorded using DSO having analog bandwidth of 1 GHz and sampling rate of 5 GS/s. The signal on DSO can be stored/saved on a personal computer (PC) for further analysis and calculation of various parameters.

4.4.2 Parameter Measurement

The objective of the present work is to find out the operating range of SRS of VISAR for which it remains linear with sufficient signal amplitude (leading to high SNR). The main components of SRS which govern the required operating range are the coupled optical power and PMT response. The coupled optical power can be controlled by laser source and aperture opening where as PMT response is governed mainly by its supply voltage (PMT gain). The measurements carried out by varying the SRS parameters (laser source, aperture opening and PMT gain) for confirming the linear range of operation with sufficient SNR are listed below:

- (i) Signal amplitude at different optical power of CW laser (20 mW to 600 mW) at fixed aperture opening with variable PMT gain (Control Voltage: 0.5 V to 1.0 V)
- (ii) Signal amplitude at different optical power of CW laser (20 mW to 80 mW) with variation in aperture opening (2 mm to 50 mm) with fixed PMT gain.

- (iii) Pulse response at variable PMT gain (Control Voltage: 0.6 V to 1.0 V) using NaI scintillator with Cesium-137 source.

The above mentioned measurements are used to calculate/interpret various parameters like

- (i) Region of operation, based on PMT response linearity
- (ii) Gain linearity at different input optical power
- (iii) SNR variation with respect to (a) aperture opening and (b) input optical power at different PMT gain
- (iv) Variation in rise time and fall time with respect to PMT gain

Method of calculating the above are discussed in next section. It is to be noted that each data point or measurement is generated three times and then an average value is considered for processing. To minimize the effect of constant offset voltage of the VISAR output and in turn the effect of background current and saturation, the output of laser is converted into pulsed form using Pockels cell. The width of the pulse is chosen to be $\sim 70 \mu\text{s}$, same as that used in the actual experiments. The pulsed operation of laser source and in turn that of the SRS provides an added advantage of increased mean output current for linear range of operation. The specification sheet of PMT indicates the maximum output/anode current for its operation in linear range. This value of maximum output current is specified for its continuous mode of operation whereas in case of pulsed operation the values of maximum output current is treated as averaged over one second. Hence the pulse duration can be reduced to smaller than one second by maintaining the average output current per second be not more than maximum output current in continuous mode of operation. In the present case, the maximum average output current of PMT is $100 \mu\text{A}$ so that for a 50Ω load the output voltage is about 5 mV. In pulsed mode of operation this value of output voltage can further be increased proportionately. Hence the linearity of SRS needs to be established for pulsed (~ 70

μs) operation of laser source and maximum amount of output current/voltage that can be obtained from SRS.

The width of the pulse is chosen based on the time duration for which the laser light is required to be present during an experiment and $70 \mu\text{s}$ is found to be sufficient. Pulse shorter than $70 \mu\text{s}$ may result in loss of data while a pulse longer than $70 \mu\text{s}$ may reduce the maximum average output current/voltages for operation in linear range. In the next section the method of analyzing data and results are presented.

4.5 Data Analysis and Results

This section is divided in two parts. In first part linear range of operation based on the measured data is determined whereas in second part signal quality in terms of SNR, and rise/fall time is verified.

4.5.1 Range of Operation Selection

Range of operation of the PMT and in turns that of SRS, is decided based on its linear response to the input optical power. PMT response is measured at around 25 points in the range of 20 mW to 600 mW laser power. On detector side, the gain of PMT is varied by fixing control voltage at 8 different points in the range from 0.5 V to 1.0 V. At every settings of laser power and PMT gain, three independent measurements are recorded i.e. total of $25 \times 8 \times 3$ values of output voltage across 50Ω resistance. Average value of three measurements at each setting of laser power and PMT gain is taken as the input for evaluating the range of operation. Figure 4.4 presents the set of data points measured at different setting of laser input power and PMT gain setting. These data points are then used for processing and estimating operating range of the SRS for the VISAR.

For the purpose of analysis, let x , be the value of laser power and $f_g(x)$ the measurement of SRS output at gain setting ' g ' of PMT. To evaluate the region of operation, a linear curve fitting is carried out on the data $f_g(x)$ with x as the independent variable. To achieve the goodness of fit close to unity at each ' g ' setting, measurement points with higher input optical power (close to 600 mW) are removed. A general trend is observed that the more and more data points are required to be removed from the higher input optical power side as the gain is increased from $g = 0.5 V$ to $g = 1.0 V$. Let the result of the linear curve fitting of data be denoted as $f_g^{lf}(x)$ then the percentage non-linearity based on linear curve fit data is obtained as

$$\% NL_{lf} = \frac{f_g(x) - f_g^{lf}(x)}{f_g(x)} \times 100 \quad (4.6)$$

In Fig. 4.5, constraint lines are plotted along with the measured data points. The region outside the constraint lines indicate the portion of measured data for which the $\% NL_{lf}$ value is more than 5%. The region with $\% NL_{lf}$ less than 5 % (portion of data points

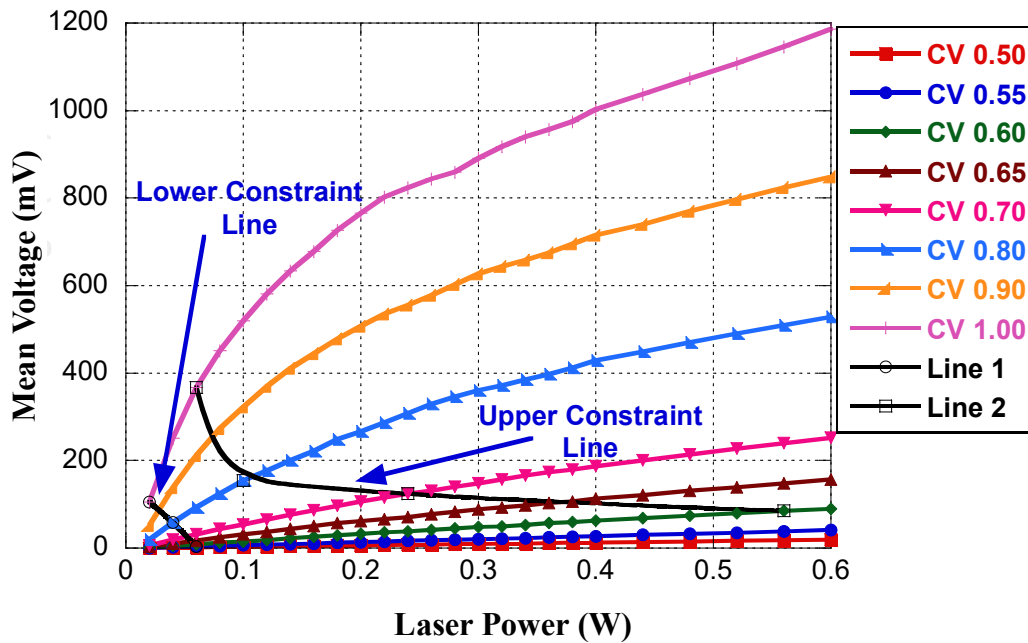


Figure 4.5: Measured mean output voltage with respect to input laser power at different CV setting of PMT

in between two constraint lines) is treated to be linear for operation of SRS. Additional confirmation of linearity is obtained by verifying additivity and homogeneity on the portion of data points in between two constraint lines plotted in Fig. 4.4. The additivity and homogeneity relations used for confirmation are defined as follows:

$$\text{Additivity: } \text{for } x_1 \Rightarrow f_g(x_1); x_2 \Rightarrow f_g(x_2) \quad (4.7)$$

$$\text{such that } x_3 \Rightarrow f_g(x_3) \Rightarrow f_g(x_1) + f_g(x_2) \quad \text{where } x_3 = x_1 + x_2$$

$$\text{Homogeneity: } \text{for } x_1 \Rightarrow f_g(x_1); \quad (4.8)$$

$$\text{such that } ax_1 \Rightarrow f_g(ax_1) \Rightarrow af_g(x_1) \quad \text{where } a \text{ is a constant}$$

From Fig. 4.5, it can be interpreted that as the input power is increased for a fixed PMT gain, the response moves from linear to nonlinear region of operation. Similarly, it is observed that for a fixed input power, if the PMT gain is increased by changed control voltage (CV) from 0.5 V to 1.0 V the response moves from linear to nonlinear region. A major cause of non-linearity under such conditions is the saturation effect which arises either from high optical input power or from high gain of PMT. The saturation in the response of PMT occurs due to space charge limitation at the last few dynodes near the anode. Another reason for saturation is the production of radial voltage drop at the photocathode caused by large current densities (either by high gain or large optical input) [91].

It is also evident from Fig. 4.5 that, for very small value of optical power the PMT response is not linear for lower gains. This is attributed to the prominent effect of dark current at low control voltage and small laser power. Large dark current can also reduce the range of linear operation by reducing the saturation output pulse current for PMT [91].

Figure 4.6, which represents the gain of PMT with respect to control voltage setting at three different laser powers, complements the information of Fig. 4.5. The gain has been calculated from measured output voltage and laser power using the relation:

$$\text{Gain} = \left(\frac{v_m}{R_L} \right) \times \frac{1}{x} \quad (4.9)$$

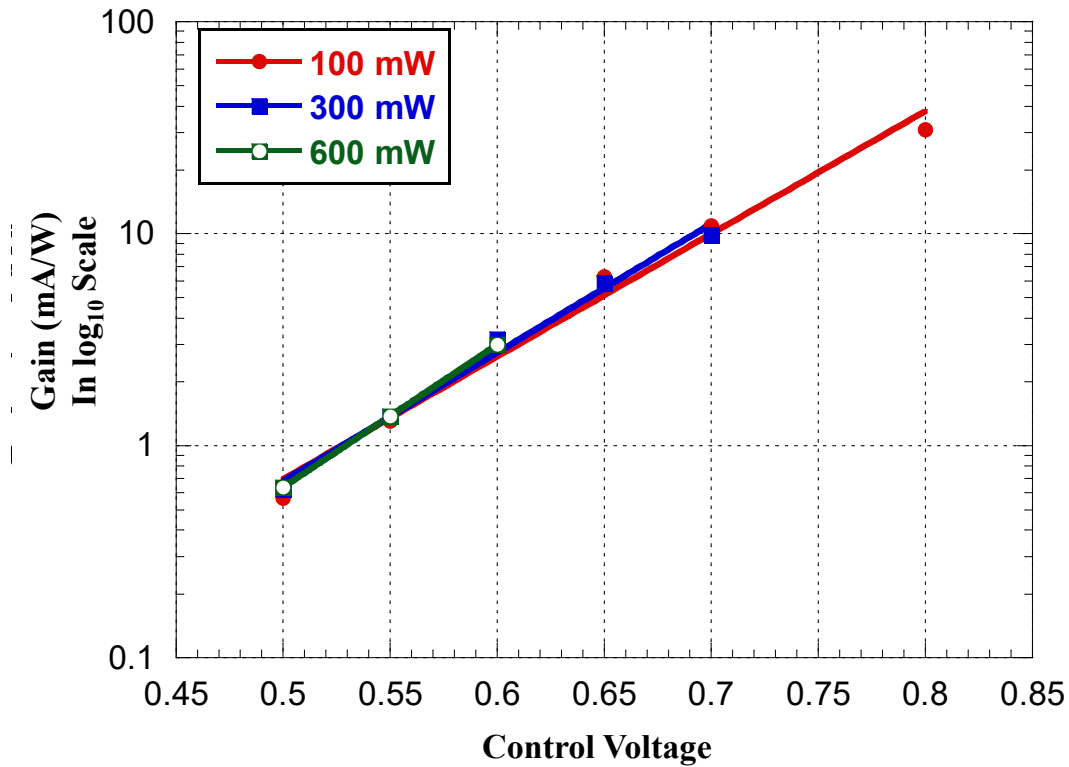


Figure 4.6: Gain Variation with respect to CV for three optical input powers

where v_m is the measured output voltage, R_L is the output load resistance and \mathcal{X} is the laser power. For low laser power (100 mW), the gain is linear when PMT control voltage setting ranges from 0.5 V to 0.8 V. This linear range of control voltage reduces to 0.5 V - 0.6 V for input laser power of 600 mW.

4.5.2 Signal Quality Measurement

Further, the variation in signal quality in terms of SNR (in dB) with respect to laser power and opening of the aperture has been determined. The variation in SNR with respect to laser power is determined at different control voltages (gain setting) of PMT. However, the variation in SNR with respect to aperture opening is determined at different laser power, for a fixed control voltage. SNR in present studies is determined as given in Equ. 4.2.

Figure 4.7 represents the calculated values of SNR with respect to laser power for different PMT control voltages, ranging from 0.5 V to 1.0 V. It is clear from the figure that as

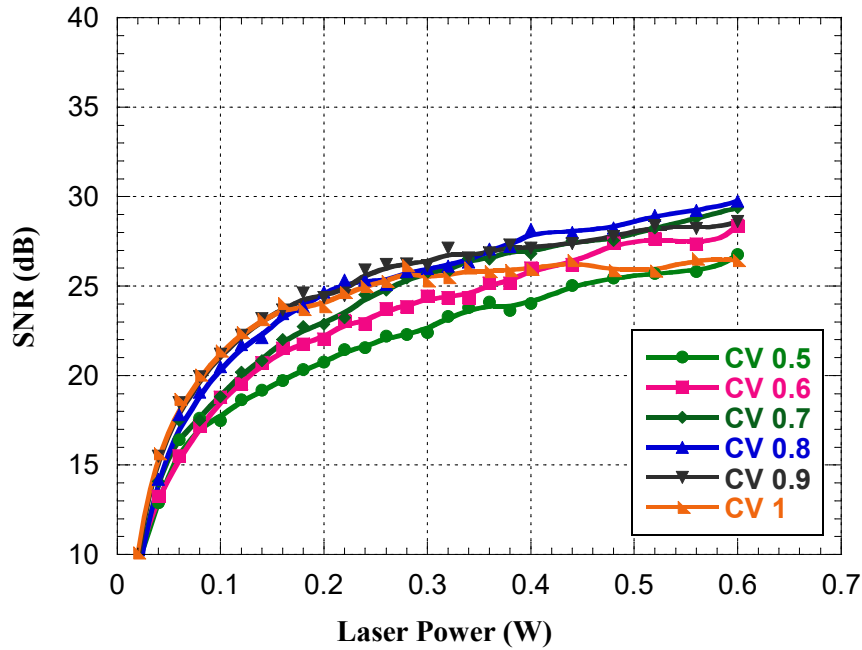


Figure 4.7: SNR Measurement with respect to Input Laser Power at different CV settings

the laser power is increased from 0.2 W to 0.6 W, the average value of SNR increases monotonically from a minimum of ~ 9.5 dB to maximum of in the range of ~ 27 dB to ~ 29.5 dB for all control voltages settings. It is also evident from the figure that the improvement in SNR with increasing PMT control voltage setting is not very significant (within $\sim 10\%$ at the largest input optical power of 0.6 W). The improvement in SNR by increasing laser power is caused by increase in the number of photons falling on the photocathode of PMT, leading to generation of more anode current.

Similarly Fig. 4.8 shows variation in SNR with respect to opening of aperture placed in front of imaging optics to limit the effect of stray light from other areas. This aperture is having minimum opening of 2 mm and maximum of 50 mm in diameter. As seen in Fig. 4.8, the SNR increases monotonically with the increase in aperture opening up to 40 mm. Thereafter, either it saturates or decreases.

Aperture opening allows uninterrupted entry to the free space optical beam (diameter ~ 15 mm) on to the PMT of SRS. The saturation in SNR beyond 40 mm of opening indicates

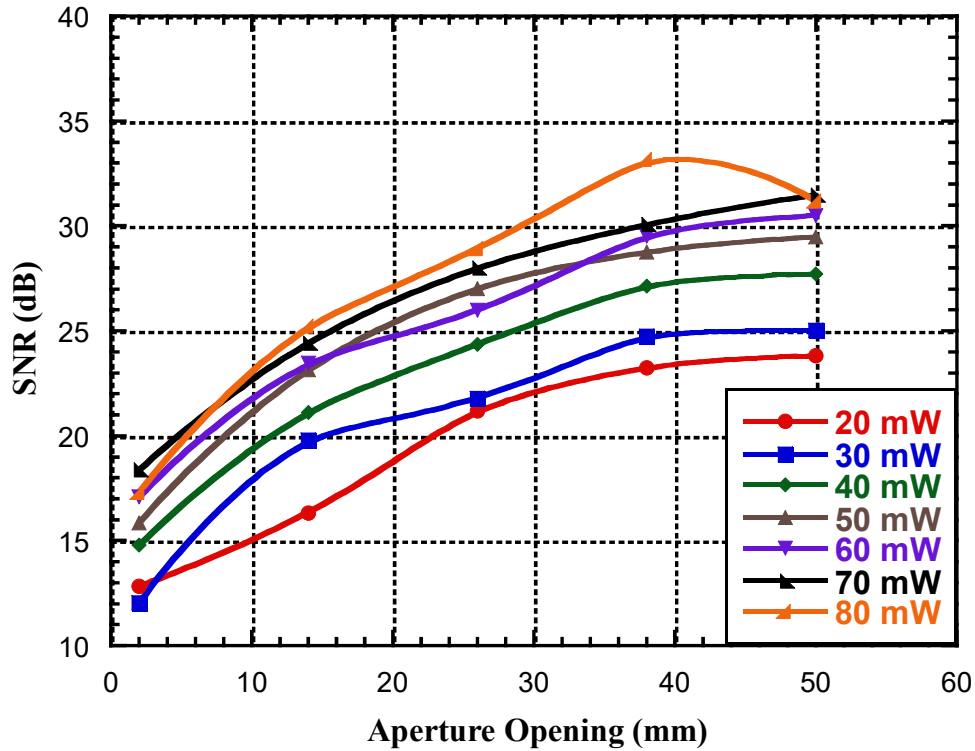


Figure 4.8: SNR Measurement with respect to aperture opening at different Input Laser Power

that apart from intended optical signal, background light is also getting coupled to PMT and this leads to increase in random noise level. Further, it is also clear from the figure that at all aperture openings (at least up to 40 mm) the SNR improves as the input laser power is increased. The value of SNR up to 20 dB or higher is sufficient for recording the signal which can further be improvement using signal processing techniques [124] if required. Hence for linear operation of SRS with sufficient SNR, the combination of laser power, PMT gain setting (Control Voltage) and aperture opening (~40 mm) are chosen such that the recorded electrical signal has value of SNR up to 20 dB or higher (Fig. 4.7 & 4.8) and output voltage in between the two constraint lines (Fig. 4.5).

Another important characteristic of PMT is its time response to the fast-optical pulses. In the present study, the rise time characteristic of the PMT has been determined by recording the fast pulses having rise time of order of 400 ps generated from NaI(Ti) scintillator coupled

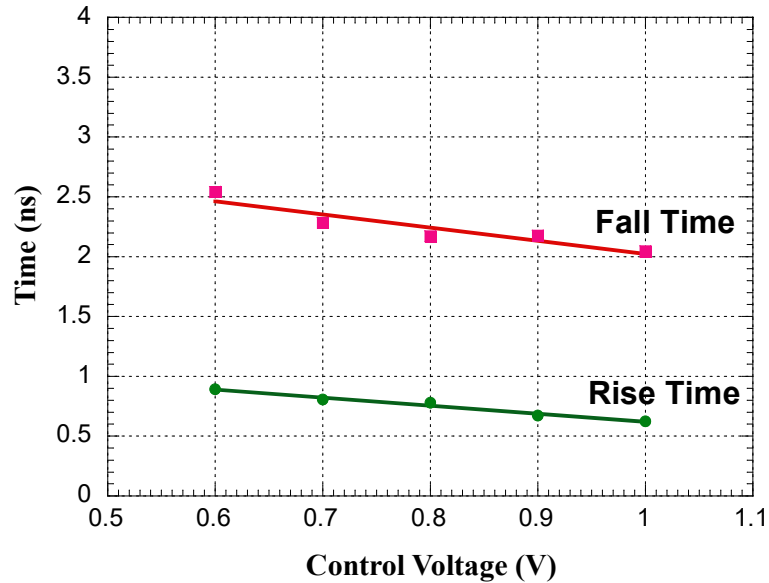


Figure 4.9: Rise Time and Fall Time variation with respect to Control Voltage

with PMT in presence of with Cs^{137} source. The measured rise time and fall time of output pulses, with respect to the PMT control voltage setting, is presented in Fig. 4.9. As evident from the figure, both the rise time and fall time of the PMT output pulse decrease monotonically with increasing control voltage. This monotonous decrease could be associated to the well-established fact that the increase in control voltage (or equivalently the electric field intensity) improves the electron transit speed and shortens the transit time and rise time. The rise time improves from 0.9 ns to 0.6 ns as control voltage increases from 0.6 V to 1.0 V (Fig. 4.9), whereas for the similar range of control voltage the fall time improves from 2.5 ns to 2.0 ns.

4.6 Summary and Conclusions

The work, describes a procedure for optimization of PMT gain, laser power and aperture of SRS so that it can work in linear region with sufficient SNR for accurate measurement of velocity history using VISAR. The procedure is significant for in-situ optimization of SRS, *i.e.* with PMT, imaging optics and aperture in their actual position as in

real experiment. The major outcomes of the present work, in terms of linear range of operation and signal quality for SRS can be summarized as follows:

- (i) For a fixed gain setting (control voltage) of PMT, the SRS response (output voltage across load resistance of 50Ω) increases with increasing input optical power. The response beyond the upper constraint line (Fig. 4.5) deviates more than 5% from the linear fit of data.
- (ii) For a fixed input optical power, the response of SRS (output voltage across load resistance of 50Ω) increases as the PMT gain is increased. Response beyond the upper constraint line (Fig. 4.5) deviates more than 5% from the linear fit of data.
- (iii) For low input optical power ($< 60 \text{ mW}$) the SRS response with respect to the input optical power does not follow linearity and deviates more than 5% from the linear fit of data.
- (iv) Additivity and homogeneity test on the data between upper constraint and lower constraint line are performed and found to be satisfying within 5% limit with the linear fit.
- (v) Signal to noise ratio (SNR) is calculated for full measured data set (as displayed in Fig. 4.7). The acceptable value of SNR is 20 dB or higher i.e. laser power should be more than 0.2 W for lowest PMT gain setting (Control Voltage 0.5 V). SNR is also calculated as a function of aperture opening for different input laser powers (Fig. 4.8). Aperture opening of the SRS in the range of 25 mm to 40 mm provides the acceptable SNR value of up to 20 dB or higher.
- (vi) The rise time and fall time of PMT are recorded independently and they show a decreasing trend as the control voltage increased from 0.6 V to 1.0 V.

The procedure of optimization of SRS for VISAR mentioned here is successfully implemented and parameters of SRS in all shock experiment are selected on the basis of the

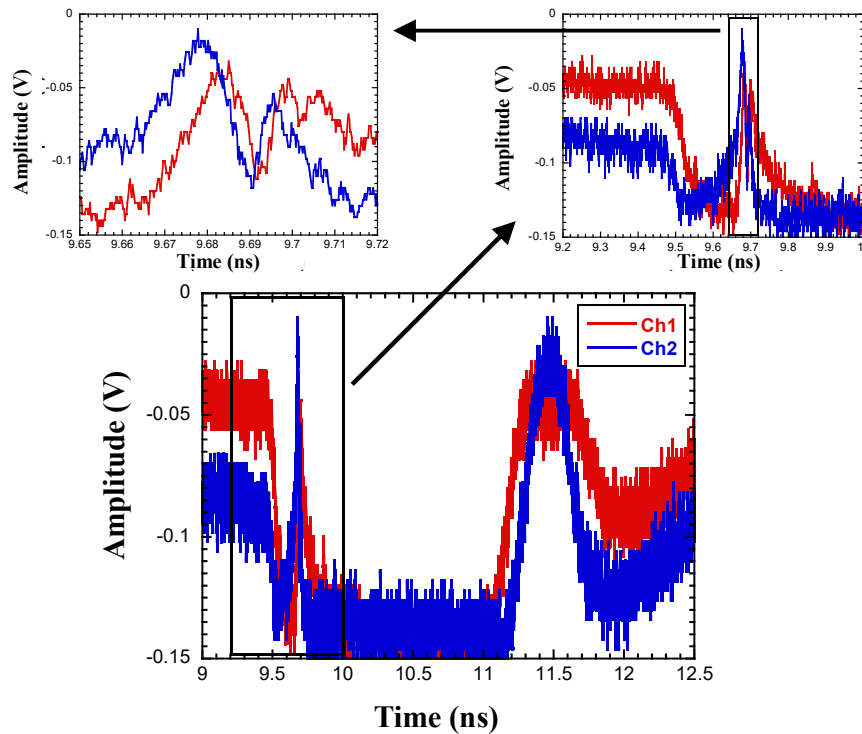


Figure 4.10: Improved signal record after applying present studies

above-mentioned results. The mechanical and physical properties of materials have successfully been estimated by recording fringe pattern and estimating accurate velocity profiles [29]. A typical VISAR signal recorded in one of shock experiment under the constraint parameter setting (PMT Control voltage 0.8 V & aperture opening 30 mm) is presented in Fig. 4.10. The recorded signal has SNR of 25 dB. The minimum period of one fringe measured in this recorded signal is of the order of 20 ns. This generic procedure of identifying the suitable operating range of SRS for VISAR interferometer could be utilized for similar set ups having different optical components and photo detector.



Chapter 5

Development of Modified Wiener Filter based Signal De-noising Method for VISAR

5.1 Introduction

In previous chapter the linearity and range of operation for VISAR has been established. It was also confirmed that the recording system (which is consist of PMT and DSO in present case) has sufficient bandwidth and sampling rate to record the signal of desired dynamics. The phase of the recorded/measured data during experiment contains the information about the free surface/particle velocity of the target. But to obtain the information on the free surface/particle velocity profile from the measured phase, the unwrapping of phase is required. The performance of phase unwrapping algorithms used for this purpose depends significantly upon the SNR of the recorded/measured data. In present chapter, a novel de-noising method based on the modified Wiener filter has been discussed and used for de-noising the VISAR signals. The qualification of the proposed method is carried out on the basis of optimization of filter parameters and comparison with the other standard de-noising methods. Further, the improvement in the free surface velocity history derived from de-noised VISAR signals is presented. Also the information is presented about the method of reading experimental data and selecting required data range for signal pre processing based on the knowledge about the experimental setup.

5.2 Experimental Setup and Data Selection

5.2.1 Experimental Setup

Figure 5.1 shows the typical experimental setup with sensor locations for generating different signals for measurement of impact velocity, shock velocity, stress profile, free surface velocity profile etc. during dynamic compression experiments. As discussed earlier, in dynamic compression experiment using Gas Gun, a flyer plate travels with the velocity in the range from 100 m/s to 1 km/s and impacts at the stationary target plate. Before impact of flyer plate on to the stationary target, its velocity is measured using electrical or optical sensors placed across the path of the flyer plate (Fig. 5.1). As already mentioned in earlier chapter, these sensors provide information on impact velocity by measuring the time of flight. Based on same principle of time of flight measurement, the shock velocity is measured using shock arrival sensors. The stress profile inside the target is measured using piezo-resistive Manganin gauge. Whereas the free surface velocity is measured using VISAR for which is reflected laser light is collected using probe.

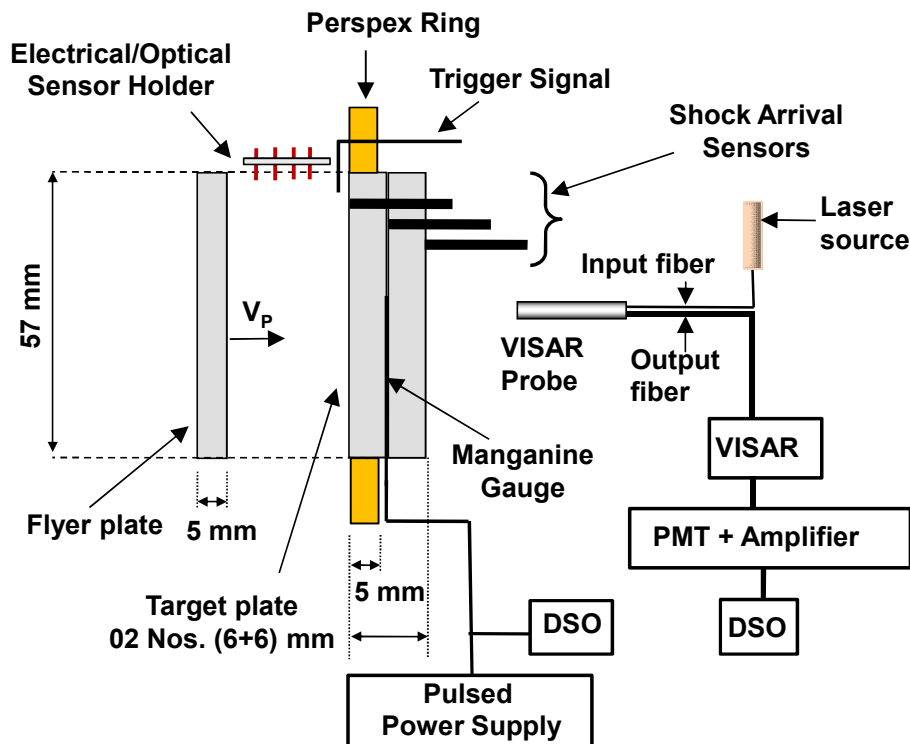


Figure 5.1: Typical Plate Impact Experimental Setup

As shown in the Fig. 5.1, just before the impact of flyer on the target, a pair of pins is used to generate a trigger signal which enables the recording system to start the recording of data from different diagnostic systems. The desired time window for data acquisition using recording system is predetermined depending on the experimental parameters such as distance of trigger pins from impact surface and impact velocity. Further, the knowledge of impact velocity and distance of trigger pins from impact surface is useful in selecting useful data as discussed in next section.

5.2.2 Data Selection

Dynamic compression experiments are single shot experiments and preparation of each experiment takes a lot of efforts, hence performance of each diagnostic technique including the trigger generating system is very important. Trigger signal which allows the recording of all other signals is of paramount importance, hence its performance and consistency has to be ensured before each experiment. This signal is a positive edge signal having very small rise time of the order of ~ 10 ns and amplitude of ~ 5 -12 V. In recorded signal the time reference of the trigger signal is zero time and reference of other data is taken as post trigger (time after zero time) and pre trigger (time before zero time). In a well designed and systematic experiment all the diagnostic signals are available in the post trigger time.

In these experiments, only impact velocity data is available in pre trigger time. Based on the impact velocity data and prior estimate of material parameters of target, the approximate time range is anticipated for the rest of the diagnostic signals. The approximate information of this time range is very useful in selecting the data from the recorded signals. Invariably DSOs are used to record the data from the sensors and diagnostic setups. These DSOs can save the data in digital form where one column is reserved for each recorded channel and one dedicated column for time stamping for each data point. The number of data

points in each column including time stamping is fixed based on the setting of record length (number of data points reserved for recording) in the DSO. The duration of record setting defines the sampling rate for particular fixed number of samples. The typical DSO used in dynamic compression experiments has the recording specification as: analog bandwidth of 1 GHz, sampling rate of 5 GHz and record length up to 10 million points. These specifications correspond to total record time of 2 ms at the highest sampling rate of 5GS/s. The format of digitally stored data can be in comma separated values (.CSV), text format (.TXT) or specific to the instrument. For analysis of data using MATLAB, the data is stored in CSV format.

For analysis of VISAR signals, the start of data is selected on the basis of the time anticipated for the arrival of the shock wave at the target rear surface and end of data is observed in the signal itself till the VISAR probe is intact for provided useful data. The VISAR probe is placed in such a way that the complete history of the free surface velocity is captured before probe is damaged. Figure 5.2 displays a typical recorded VISAR signal, where, start of signal and end of signal is marked. Further pre-processing of data (de-noising) is described in next section.

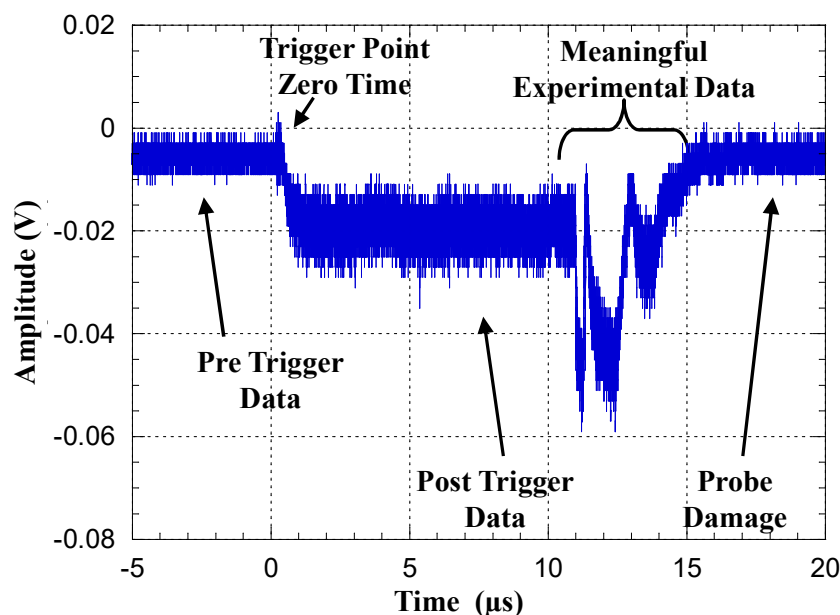


Figure 5.2: Typical recorded signal of VISAR with data identification.

5.3 Requirements of Signal De-noising and Available Methods

Once the meaningful part of the recorded VISAR data is identified, one needs to calculate the phase change as a function of time. The phase of the recorded signal contains the information about the particle/free surface velocity of the shock loaded target. Phase of the signal changes from 0 to 2π for a single fringe (one complete cycle of sinusoidal signal), but for more than one fringe the phase again starts from 0 after reaching 2π . Identification of this phase jump indicates the completion of one cycle and start of new fringe. Hence it is very important to identify these phase jumps for counting correct number of fringes.

Phase unwrapping algorithms are developed to detect phase jumps and convert them in accurate total number of fringes [98]. The presence of noise (low SNR) in the recorded signal, however, makes it difficult to detect phase jump correctly and sometime results in false jumps [99-101]. This is evident from the two situations one corresponding to clean signal (Fig. 5.3(a)) and other representing the case of noisy signal (Fig. 5.3 (b)). As is clear from the figure for noisy signal the derived phase information contains many false jumps.

Apart from the detection of false phase jump, addition of noise increases the uncertainty in determination of particle/free surface velocity. Further, as the change in phase and frequency of the signal is function of the time dependent velocity of the target free surface which itself is governed by the material properties, it is not possible to predict it in advance. At the same time any de-noising mechanism requires some information about the input signal, *e.g.* its frequency, SNR and type of noise, for selecting filter parameters like pass band, threshold etc. De-noising of a signal corrupted by additive noise having separable spectrum for signal and noise, is carried out using linear filters like low pass, high pass and band pass filters [102].

However, for signals, where, noise and signal spectrums are non-separable, the spectrum of signal is cleaned by methods like Fourier coefficients thresholding [103, 104],

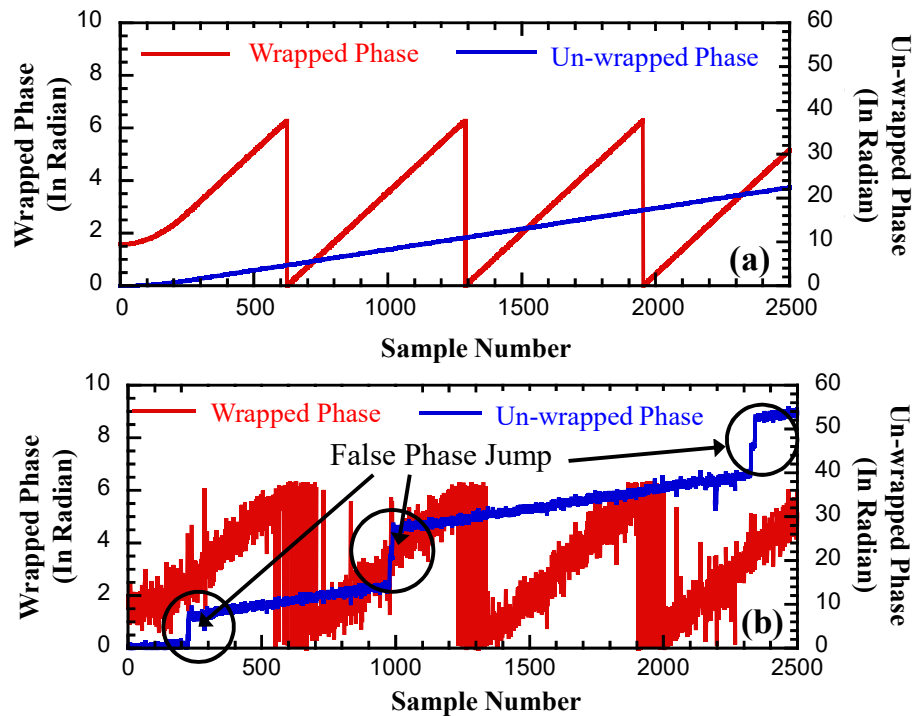


Figure 5.3: Wrapped and Unwrapped Phases (a) Clean Signal (b) Noisy Signal with false phase jump due to noise.

wavelet shrinkage [105 - 108], spectral subtraction [109 - 113] etc. The performance of such methods depends on the selection of threshold value. Too much of threshold will destroy the signal components where as too small a threshold will leave the noise component in the signal unchanged. There is another class of filters available which are called adaptive filters where clean noise free signal is obtained by minimizing Mean Squared Error (MSE) between desired signal $x(n)$ (noise free signal) and estimated signal $\hat{x}(n)$ (filter output). Wiener filter is one such method which adapts the filter coefficients depending on the noise present in the signal. Larger is the SNR smaller is the value of filter coefficient. Next section presents the two important de-noising filters (Spectral Subtraction Method and Wiener filter) for the noise removal from the signals where noise and signal spectrums are non separable. Further using the best available features of the two filters a novel de-noising method has been proposed and developed.

5.3.1 Spectral Subtraction Method

Spectral subtraction method (SSM) is one of the oldest methods of signal processing for de-noising the signal from the additive stationary noise [125]. It is based on the principle that noise spectrum can be estimated and updated from the non active region of the recorded signal and the clean signal is obtained by subtracting this noise spectrum estimate from the recorded noisy signal spectrum [109 - 113]. It is assumed that the noise is stationary and additive in nature, *i.e.* its spectrum does not change with time and it is uncorrelated with the actual signal. Mathematically this can be expressed as follows [125]:

$$y(n) = x(n) + d(n) \tag{5.1}$$

Where, $x(n)$ is noise free signal, $d(n)$ is the stationary additive noise and $y(n)$ is the noisy signal. Here n is the time index. The objective of the spectral subtraction is to estimate $x(n)$ from the given $y(n)$ assuming $d(n)$ is uncorrelated with $x(n)$. Fig. 5.4 presents the block diagram representation of the SSM. SSM works on the segmented data, the $y(n)$ is divided into ‘ K ’ segments of equal length using windowing operation. Each segmented signal is transformed into frequency domain using Discrete Fourier Transform (DFT). The segmented

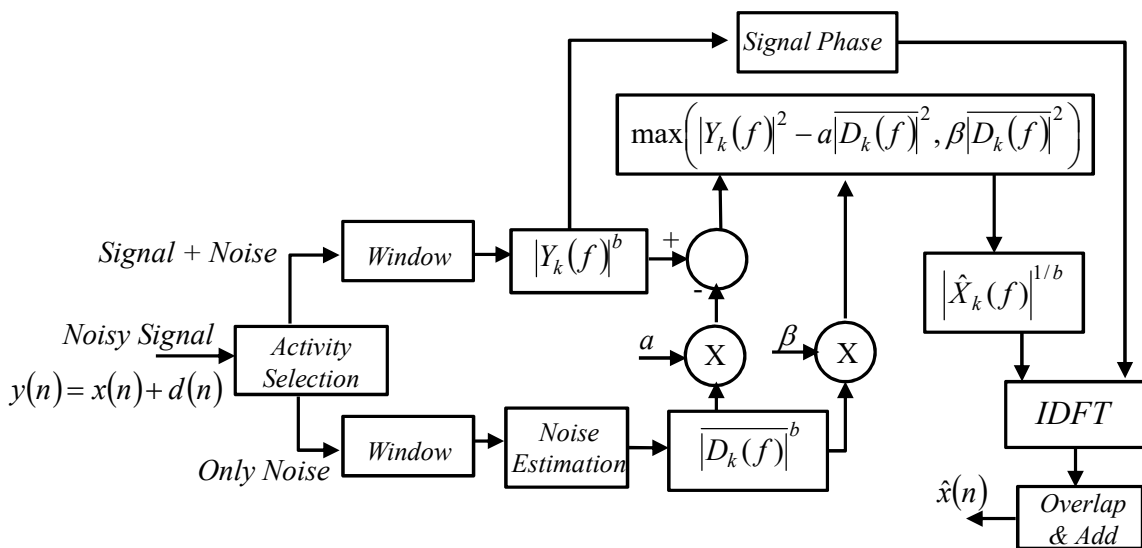


Figure 5.4: Block diagram of Spectral Subtraction Method

signal in frequency domain is given as [125]:

$$Y_k(f) = X_k(f) + D_k(f) \text{ for } 0 \leq k \leq K - 1 \quad (5.2)$$

where k is the index for the segment with $Y_k(f)$, $X_k(f)$ and $D_k(f)$ are the DFT coefficients for $y(n)$, $x(n)$ and $d(n)$, respectively of the segment k . Mathematically spectral subtraction is represented as:

$$|\hat{X}_k(f)|^b = |Y_k(f)|^b - a\overline{|D(f)|^b} \quad (5.3)$$

Where, $\overline{|D(f)|^b}$ is the time averaged spectrum of noise for K frames and is calculated as:

$$\overline{|D(f)|^b} = \frac{1}{K} \sum_{k=0}^{K-1} |D_k(f)|^b \quad (5.4)$$

As mentioned in Equ. 5.3, the exponent b determines whether it is a subtraction of magnitude spectrum or power spectrum. The $b = 1$, is used for magnitude spectral subtraction and $b = 2$, is used for power spectral subtraction, respectively. Here 'a' is the scaling factor which defines the amplitude of noise subtraction. Spectral subtraction presented in Equ. 5.3, may contain negative spectral component which are not practical values in Fourier domain. Another parameter β known as noise floor is introduced in the SSM [112] to convert negative spectral components into meaningful positive values.

The SSM using scaling factor and noise floor is given as:

$$|\hat{X}_k(f)|^2 = \begin{cases} |Y_k(f)|^2 - a\overline{|D(f)|^2} \\ \beta\overline{|D(f)|^2}, \text{ if } |Y_k(f)|^2 - a\overline{|D(f)|^2} < \beta\overline{|D(f)|^2} \end{cases} \quad (5.5)$$

where, $a \geq 0$, $\beta \ll 1$ and $b = 2$ is chosen for power spectral subtraction. The noise spectrum consist of random peaks and valleys, the introduction of scaling factor and noise floor tries to smooth out the estimated signal spectrum and improves the signal quality. Amplitude of noise subtraction is varied using scaling factor. For smaller value of 'a' ($a < 1$) the noise component may remain unchanged in the de-noised signal while for larger value of 'a' ($a > 1$) the spectral components required in de-noised signal may get attenuated. Noise

floor or residual noise of the enhanced signal is determined by the factor β . The introduction of noise floor limits the spectral component value in de-noised signal to a lower bound of $\beta\overline{|D(f)|^2}$. Addition of noise floor term in spectral subtraction also reduces high amplitude transient in the frequency spectrum [110, 111]. As reported in the literature [112], the optimum value of scaling factor ‘ a ’ ranges from 3 to 6 and that of noise floor ‘ β ’ ranges from 0.005 (0.5%) to 0.02 (2%) of noise spectrum for the SNR ≥ 0 dB. The obtained power spectral estimate after SSM, is converted to Fourier coefficients using square root of $|\hat{X}_k(f)|^2$ as the magnitude part and phase of $Y_k(f)$ as phase part for the Fourier coefficients. An Inverse Discrete Fourier Transform (IDFT) is then performed to reconstruct the time domain de-noised estimate of the signal. Windowed time domain signal is reconstructed back using overlap and add method.

5.3.2 Wiener Filter

Wiener filtering is the popular signal processing techniques which has been in use for de-noising of images [103, 104, 108], speech signals [107] and ECG signals [126]. A block diagram of WF filter is displayed in Fig. 5.5. The design objective of Wiener filter is to estimate clean signal from the signal corrupted with additive, non-correlated noise. The estimate of clean signal is obtained by minimizing Mean Squared Error (MSE) between desired signal $x(n)$ and estimated signal $\hat{x}(n)$. As presented in [102], the optimized solution for the minimization problem in frequency domain, in terms of filter transfer function, is written as:

$$H(f) = \frac{P_X(f)}{P_X(f) + P_D(f)} \quad (5.6)$$

where $P_X(f), P_D(f)$ are the power spectrum of the desired signal $x(n)$ and noise $d(n)$. In terms of signal to noise ratio (SNR) Wiener filter equation is written as:

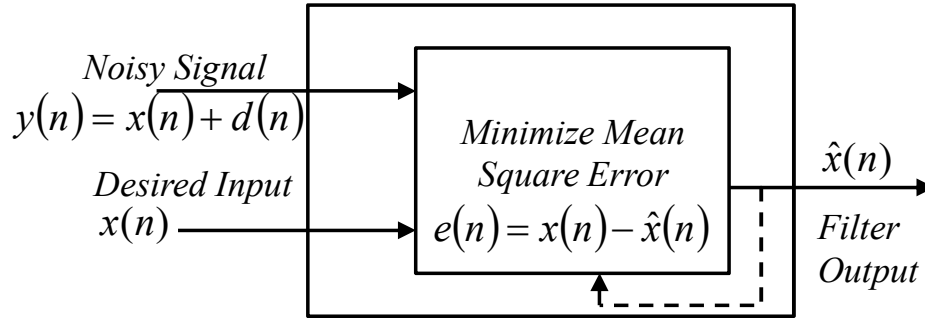


Figure 5.5: A block diagram representation of Wiener Filter

$$H(f) = \left[1 + \frac{1}{SNR(f)}\right]^{-1} \quad (5.7)$$

Where $SNR(f)$ for stationary and uncorrelated signals $x(n)$ and noise $d(n)$ is given as

$$SNR(f) = \frac{P_X(f)}{P_D(f)} \quad (5.8)$$

Wiener filter is a zero phase linear filter and its coefficients vary from 0 to 1 i.e. $0 \leq H(f) \leq 1$.

For frequency components with low SNR, Wiener filter coefficient tends to attenuate them and for frequency components with high SNR, it tends to pass signal without any attenuation. WF provides the optimal method of tapering off the noisy components (low SNR) to give de-noised signal with least mean square error. The Wiener filter requires estimation of power spectrum of the desired signal and noise prior to the filtering process. For the practical cases where the power spectrum of clean signal is not available the noisy signal power spectrum is used as

$$H(f) = \frac{P_X(f)}{P_X(f) + P_D(f)} = \frac{P_Y(f) - P_D(f)}{P_Y(f)} \quad (5.9)$$

where, the power spectrum of noisy signal and noise is given as:

$$P_Y(f) = E[|Y(f)|^2] \text{ and } P_D(f) = E[|D(f)|^2] \quad (5.10)$$

The power spectrum calculations for the Wiener filter coefficients are based on the averaging of the ensemble of different realization of the signal and noise data. Whereas SSM

utilizes instantaneous spectrum for noisy signal power spectrum and time averaging for noise power spectrum. For wide-sense stationary ergodic process, the time-averaged spectrum approaches the ensemble-averaged spectrum as the length of the signal for averaging increases [125]. Hence WF and SSM can be interchangeably used for the data from the ergodic process. This encourages the use of output of SSM for determining WF coefficients and to estimate the de-noised signal. Next section presents the proposed method for de-noising the signal using WF reinforced with SSM, where the instantaneous noisy signal and time average of the noise data is used to estimate desired signal power spectrum for WF.

5.3.3 Modified Filter Design

As discussed earlier, the use of Wiener filter requires estimation of the power spectrum of the desired signal and noise prior to application. The estimation of the desired signal spectrum is carried out using thresholding of either wavelet transform coefficients [105 - 108] or power spectrum coefficient [103, 104] of noisy signals. In present study it has been proposed to use spectral subtraction method, discussed in section 5.3.1 for estimating desired signal power spectrum for the Wiener filter. Whereas, time averaging of the noise data (as shown in Equ. 5.4) available during no signal activity period is utilized for noise power spectrum estimation.

The block diagram of the proposed scheme is presented in Fig. 5.6. As displayed in Fig. 5.6, the spectral subtraction output is used for the estimate of desired signal and noise power spectrum. This estimate of desired signal and time averaged noise power spectrum is then utilized to calculate coefficient of Wiener filter as mentioned in Equ. 5.6. The calculated filter coefficients are convolved with the noisy measured signal $Y_k(f)$ to obtain the de-noised spectrum of the signal. This spectrum is converted to time domain using inverse DFT. In time domain, de-noised signal is created by overlap and adding the windowed signal.

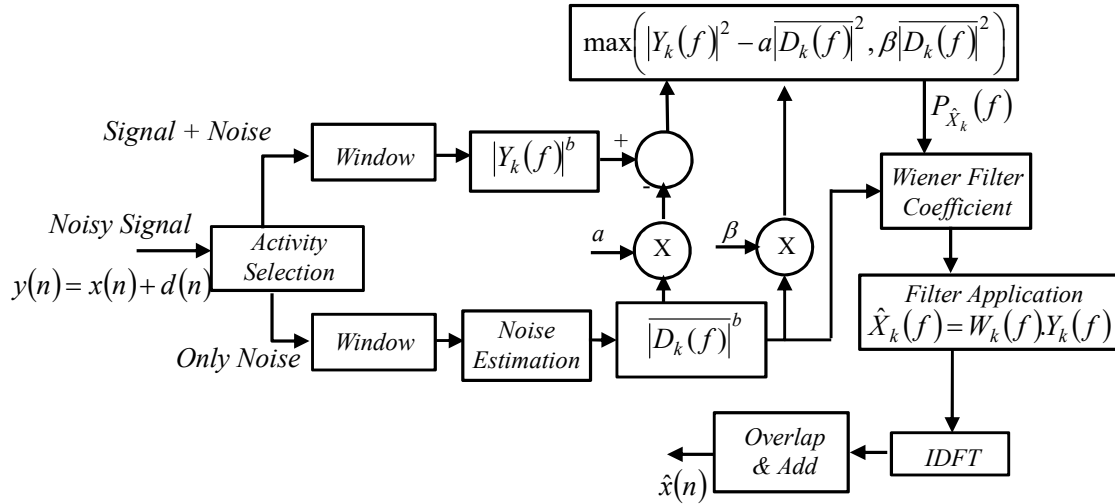


Figure 5.6: Block diagram representation proposed de-noising tool

The filter coefficients are calculated as presented in Equ. 5.9 and rewritten in terms of estimated power spectrum as follows:

$$H_{WF}(f) = \frac{P_{\hat{X}}(f)}{P_{\hat{X}}(f) + P_{D(f)}} = \frac{|\hat{X}_K(f)|^2}{|\hat{X}_K(f)|^2 + |D(f)|^2} \quad (5.11)$$

Rewriting Equ. 5.11, results in

$$H_{WF}(f) = \left[1 + \frac{1}{SNR_I} \right]^{-1} \text{ where, } SNR_I = \frac{|\hat{X}_K(f)|^2}{|D(f)|^2} \quad (5.12)$$

Equation 5.11 is the optimal Wiener filter for de-noising that is applied to a practical noisy signal having noise spectrum estimate based on the time average of the recorded signal during non activity period and signal spectrum estimate based on the spectral subtraction method optimized for scaling factor and noise floor. Equation 5.12 shows that the Wiener filter works on the improved signal to noise ratio SNR_I , which is higher than the original noisy signal. As discussed earlier and evident from the Equ. 5.11 and 5.12 also, the Wiener filter attenuates the frequency components where signal to noise ratio is low and allows the frequency components to pass with higher SNR. The minimum noise content or SNR of the output of SSM is defined by the noise floor i.e. β . The Wiener filter coefficient corresponding to noise floor is calculated by using estimate of spectrum component as:

$$|\hat{X}_k(f)|^2 = \beta |D(f)|^2 \text{ if } |Y_k(f)|^2 - a |D(f)|^2 < \beta |D(f)|^2 \quad (5.13)$$

Putting this value of $|\hat{X}_k(f)|^2$ in Equ. 5.12 results in:

$$H_{WF}(f) = \left[1 + \frac{1}{\beta}\right]^{-1} \text{ where, } \beta = \frac{|\hat{X}_k(f)|^2}{|D(f)|^2} = SNR_I \quad (5.14)$$

Where, $H_{WF}(f)$ is the Wiener coefficient at residual noise. It is clear that the proposed system further attenuates the residual noise and cleans the signal based on the improved SNR i.e. SNR_I of the estimated signal using SSM method. In next section implementation of proposed filter i.e. reinforced WF with SSM (SSM+WF) has been presented.

5.4 Filter Implementation

The implementation of the SSM+WF has been carried out by developing a code in MATLAB environment. To compare the performance of SSM+WF filter with SSM, two standard signals Bump and Doppler [127, 128], are selected. Realization of these signals is carried out for the signal length of 1024 data point. Additive White Gaussian Noise (AWGN) of similar length having zero mean and variance corresponding to SNR levels of 0 dB, 10 dB, 20 dB and 30 dB are generated. Using the standard signals and generated zero mean AWGN signals, noisy standard signals of different SNR levels are created.

The testing and verification of the proposed filter is carried out in two steps. First is the optimization for the scaling factor ' a ' for SSM. Second is the study of effect of variation of noise floor ' β ' variation on the performance of SSM and SSM+WF. The optimization of scaling factor ' a ' is carried out by varying its value from 1 to 10 for all input SNR values ranging from 0 dB to 30 dB. The optimized value is then chosen as the fixed parameter for the study the effect of variation of noise floor ' β ' on the performance of the filters (SSM and SSM+WF). For this purpose, the noise floor value is varied from 10% to 0.5% (i.e. $\beta = 0.1$ to 0.005) of noise power spectral component (Equ. 5.5).

Root Mean Square Error (RMSE) between original signal (Bump and Doppler) and de-noised signal using SSM and SSM+WF is chosen as the performance criteria and is calculated using following expression:

$$RMSE = \sqrt{\frac{\sum_{n=0}^{N-1} (\hat{x}(n) - x(n))^2}{N}} \quad (4.15)$$

Here, N is the total number of samples in the signal. After applying and comparing the SSM and SSM+WF methods on the two standard signals Bump and Doppler, these have been implemented on the interferometer signals generated due to the moving free surface of the target and recorded by VISAR instrument in two different experiments. As shown in Fig. 5.1, the VISAR system consists of PMTs for converting the generated fringe pattern into electrical signal. This signal is recorded on the digital storage oscilloscope having sufficient bandwidth and sampling rate. The dynamic compression experiments are of small duration (few μs), hence a laser source is synchronized with the event and operated for duration of $\sim 50\mu\text{s}$. Signal other than the Doppler shifted signal due to the movement of target plate during this time duration is used to sample the noise data for noise power spectrum estimation. Since this signal contains noise features of actual recording system, so it provides a good estimate of the noise power spectrum. Comparison of techniques for de-noising the signal such as SSM, SSM+WF, is carried out based on the improvement of the SNR of de-noised signal. As described in Chapter 4, the SNR is calculated using Equ. 4.2. Further, the mean and standard deviation of the estimated velocity profile is used to estimate the accuracy and precision of the measurement data. Accuracy is defined as the variation between the mean of the estimated velocity and the true value of velocity. On the other hand precision is defined as the variation in the mean velocity because of the standard deviation in the measured data. These quantities are given as

$$\% \text{ Accuracy} = \frac{V_{True} - V_{measured}}{V_{True}} * 100; \quad \% \text{ Precision} = \frac{2 * \sigma}{V_{measured}} * 100; \quad (5.17)$$

5.5 Filter Characterization

5.5.1 Optimization of Scaling Factor

The RMSE at several values of SNR (ranging from 0 dB to 30 dB) is determined as a function of scaling factor using Equ. 5.15 for noise removal based on SSM. Fig. 5.7 (a) and (b) show the variation of RMSE value as a function of scaling factor for the standard signals Bump and Doppler, respectively. As displayed in the Fig. 5.7 for each SNR, the variation in RMSE with scaling factor is calculated at the maximum and minimum of the noise floor (β), *i.e.* at 10% and 0.5% of the noise power spectrum. It is clear from Fig. 5.7 that the absolute value of RMSE between de-noised signal and original standard signal is lower for the cases having value of β as 0.5% of the noise power spectrum as compared to the case having value of β as 10% of the noise power spectrum. Another important feature, as shown in the Fig. 5.7 (a) and (b), is that the RMSE value for both the standard signals (Bump and Doppler) is minimum at the scaling factor 'a' of 4 for all SNR levels and for both values of noise floor ($\beta = 10\%$ and $\beta = 0.5\%$). This suggests that the optimized value of 'a' is 4, irrespective of input SNR and noise floor. As reported in literature [110, 112] for low SNR (SNR > 0 dB) speech

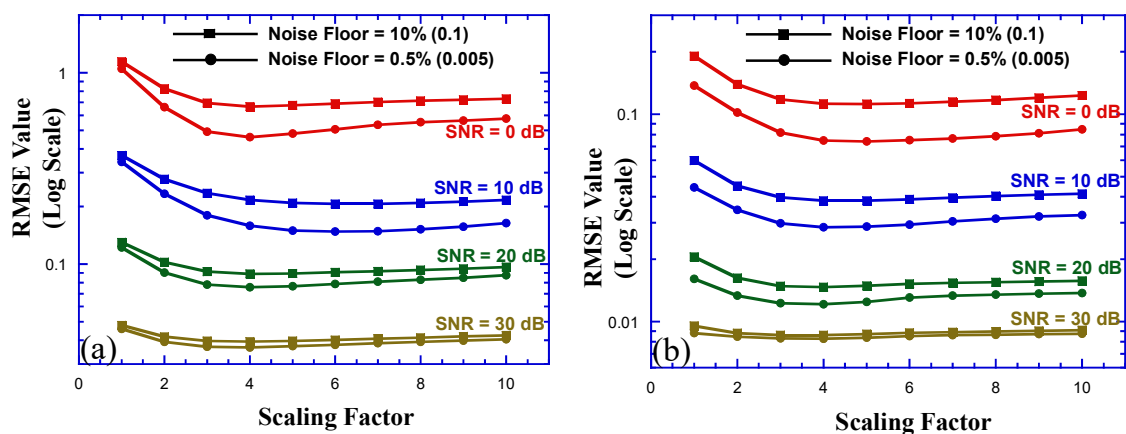


Figure 5.7: Variation in RMSE value for SSM only for scaling factor from 1 to 10 and noise floor of 10% and 0.5% (a) Bump Signal (b) Doppler Signal

signals the value of ‘ a ’ lies between 3 and 6. The presently determined value of ‘ $a = 4$ ’ for standard signal (Bump and Doppler) is in good agreement with the reported value [110, 112].

5.5.2 Effect of Noise Floor Variation

Fig. 5.8 (a) and (b) represent the variation of RMSE value, as a function of β at fixed value of scaling factor ($a = 4$) for the standard signals, Bump and Doppler using SSM and SSM+WF. Table 5.1, contains the percentage change in RMSE values for SSM and SSM+WF when β is varied from 10% to 0.5% for different SNR levels. As depicted in Fig. 5.8 (a) and (b), and Table 5.1, in case of SSM + WF method, the RMSE for all the SNR values shows a slight change (within 4%) with the variation in β in the range from 10% to 0.5%, whereas the same in case of SSM method shows a significant change (within 45%) with similar variation in β . This shows that the proposed method (SSM+WF) is relatively insensitive for the selection of noise floor or in other words the SSM+WF reduces the dependence of the quality of de-noising on noise floor i.e. one of the important parameter in minimizing RMSE using SSM. The observed insensitivity of the proposed system towards noise floor as compared to SSM is due to the addition of Wiener filter as the second step for de-noising. The Wiener filter further attenuates the spectral components depending on their

TABLE 5.1

Percentage Variation in RMSE Value for Noise Floor Variation from 10% to 0.5%

SNR	Method	Bump	Doppler
0 dB	SSM	44.86	45.42
	SSM+WF	03.46	04.00
10 dB	SSM	36.55	31.31
	SSM+WF	02.90	03.08
20 dB	SSM	17.55	31.72
	SSM+WF	01.15	02.84
30 dB	SSM	07.10	20.45
	SSM+WF	00.36	01.63

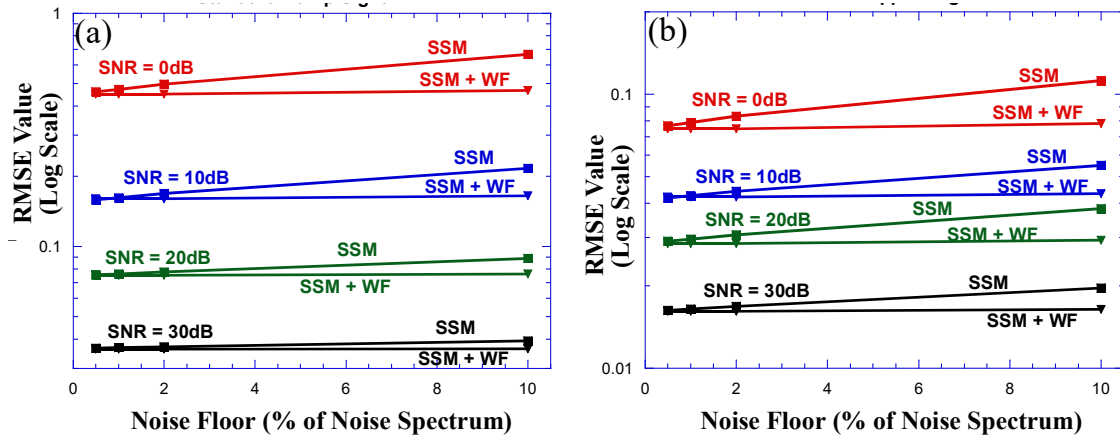


Figure 5.8: RMSE variation with respect to noise floor (a) Bump signal (b) Doppler Signal

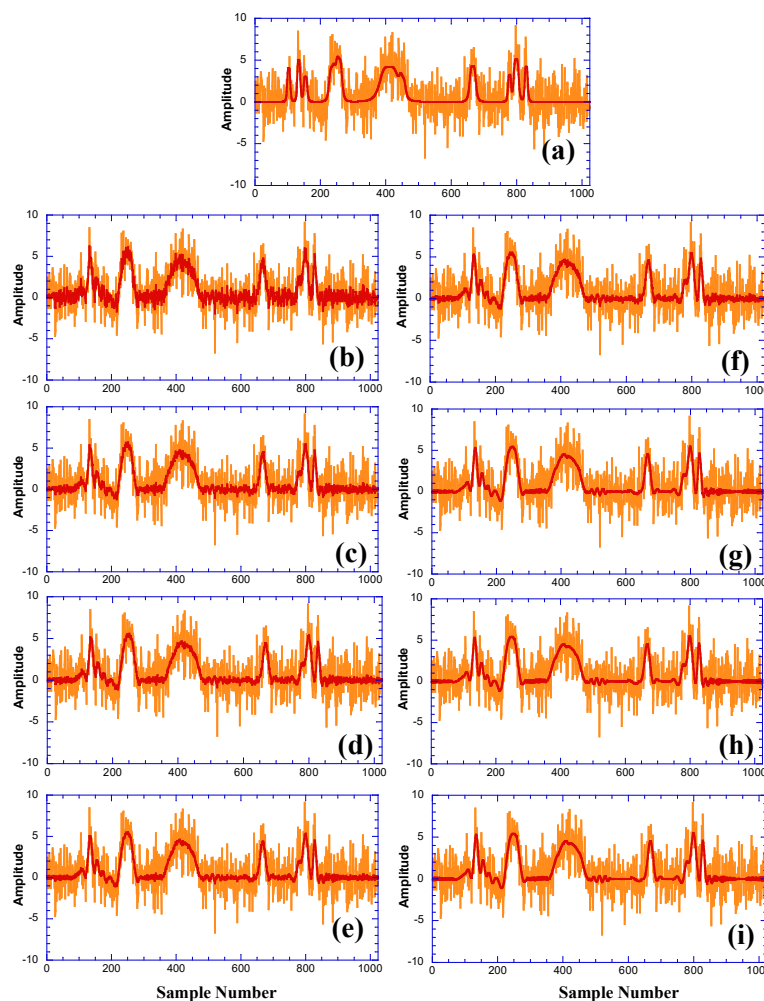


Figure 5.9: Standard Bump Signal (a) Original Signal along with 0 dB SNR (b-e) Noisy signal having 0dB SNR along with de-noised signal using SSM with noise floor values as 10%, 2%, 1% and 0.5% respectively, (f-i) Noisy signal having 0dB SNR along with de-noised signal using SSM+WF with noise floor values as 10%, 2%, 1% and 0.5% respectively.

TABLE 5.2
RMSE values for 0 dB SNR at different noise floor from SSM and SSM+WF methods. Also listed are the % differences in the same for the two methods

β at 0 dB SNR	Method	Bump	Doppler
10	SSM	0.666	0.112
	SSM+WF	0.466	0.078
	% Difference	42.92	43.58
2	SSM	0.496	0.083
	SSM+WF	0.450	0.075
	% Difference	10.22	10.66
1	SSM	0.472	0.079
	SSM+WF	0.450	0.075
	% Difference	4.88	5.33
0.5	SSM	0.460	0.077
	SSM+WF	0.450	0.075
	% Difference	2.22	2.70

SNR, specially the one's having only residual noise, as presented in Equ. 5.14. Fig. 5.9 represents the standard Bump signals de-noised using SSM and SSM+WF for input SNR of 0 dB with noise floor values of 10%, 2%, 1% and 0.5%, respectively. Table 5.2, represents the numerical value of the RMSE for same setting of parameter as used in Fig. 5.9. It also presents the percentage difference between RMSE values calculated using two methods. It is clear from the Fig. 5.9 and Table 5.2 that the de-noised signal using SSM+WF is less noisy as compared to that obtained using SSM for the noise floor ranging from 10% to 0.5%. At lowest noise floor (0.5%), though the numerical value of RMSE is close (within ~2.5%) for both SSM+WF and SSM (Table 5.2), the de-noised signal looks smoother (Fig. 5.9) for the proposed filter as compared to SSM.

5.5.3 Comparison of Proposed Filter with other Commonly Used Filters

Comparative study of few commonly used de-noising methods with proposed methods has been carried out by applying them on standard signals (Doppler and Bump). The comparison is made on the basis of RMSE value calculated between original and reconstructed standard signals (Doppler and Bump) at different SNR levels. Three types of de-noising methods are used. First is the low pass filtering method using averaging of adjacent points implemented by considering 5 points and 20 points for averaging. Second method is the wavelet shrinkage method using ‘Bi-orthogonal’ and ‘Daubechies’ family of wavelets. For application of wavelet shrinkage method ‘heusure’ is selected as threshold selection rule along with ‘soft’ threshold, ‘5’ level of decomposition with ‘mln’ for level based threshold selection were utilized. Bior6.8 [100] and db8 [99] mother wavelets were selected. Other details of the wavelet shrinkage method for de-noising are beyond the scope of this thesis. The third method used for comparing performance of the proposed filter is the spectral subtraction method (SSM). For implementing SSM and SSM+WF the scaling factor and noise floor are selected as $\alpha = 4$ and $\beta = 0.5\%$, respectively. Figure 5.10a and Fig. 5.10b represents the calculated RMSE values between original standard signal and reconstructed standard signal, for different SNR values.

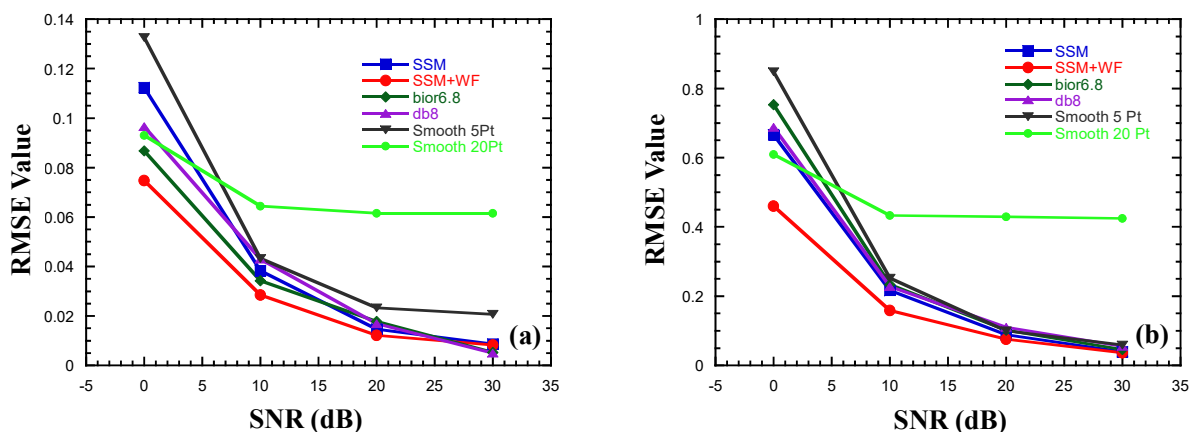


Figure 5.10: RMSE variation with respect to SNR for different de-noising methods using input as (a) Doppler Signal, (b) Bump Signal

As presented in Fig. 5.10, for high noise signal i.e. low SNR levels (up to 25dB), the proposed filter (SSM+WF) performs better than linear low pass filter (i.e. Smooth 5Pt and Smooth 20Pt), wavelet shrinkage method (i.e. bior6.8 and db8) and SSM method for both the standard signals (i.e. Doppler and Bump). At higher SNR level (~ 30 dB) the performances of these filters become comparable.

5.5.4 Experimental Signal De-noising

Having compared the performance of the SSM+WF method with SSM as well as other methods using standard signal, similar exercise on the multi-frequency electrical signals generated by the VISAR instrument due to moving free surface of the target plate in two different plate impact experiments using Gas Gun has been carried out. The SNR for test signals calculated using Equ. 4.2, are 18.52 dB and 25.26 dB, respectively. Table 5.3 shows the improved SNR of the de-noised signal and percentage change in SNR with respect to SNR of raw test signals at different noise floor levels of 10%, 2%, 1% and 0.5%, respectively.

TABLE 5.3
SNR Improvement for the signals recorded in dynamic compression experiments
(starting SNR Test 1: 18.52 dB and Test 2: 25.26 dB)

Method	Noise Floor (β)	Test 1		Test 2	
		SNR (dB)	% Change	SNR (dB)	% Change
SSM	10%	27.68	49.46	33.99	34.56
	2%	31.48	69.97	37.70	49.24
	1%	32.40	74.94	38.30	51.62
	0.5%	33.43	80.50	38.95	54.19
SSM+WF	10%	30.65	70.89	36.13	43.03
	2%	33.44	80.56	39.66	57.00
	1%	33.44	80.56	39.66	57.00
	0.5%	33.44	80.56	39.66	57.00

According to the values of SNR listed in the Table 5.3, for noise floor of 0.5%, the final SNR improvement using both the methods is around ~80% for experimental signal for test 1 and ~57%, for experimental signal for test 2. Further, for test 1 the improved SNR in case of SSM+WF, varies from 30.65 dB to 33.46 dB (~ 8.5% variation) for beta variation from 10 % to 0.5 %,whereas, the same changes from 27.68 dB to 33.43dB (~ 17.2% variation) for SSM.

Similarly the improved SNR for test 2 varies from 36.13 dB to 39.66 dB (~8.9 % variation) using SSM+WF method and from 33.99 dB to 38.95 dB (~12.9 % variation) using only SSM method. It is also observed that there is no improvement in SNR (reached at its peak improvement) for the noise floor value of 2% to 0.5% for the case of SSM+WF method in both the test signals. These observations further justify the insensitivity of the proposed method towards the noise floor selection at the stage of estimating signal power spectrum using SSM method. Fig. 5.11 (a) & (b) shows the original noisy signals and signals de-noised using proposed SSM+WF filter for $a = 4$ and $\beta = 0.5\%$ in two experiments test1 and test2.

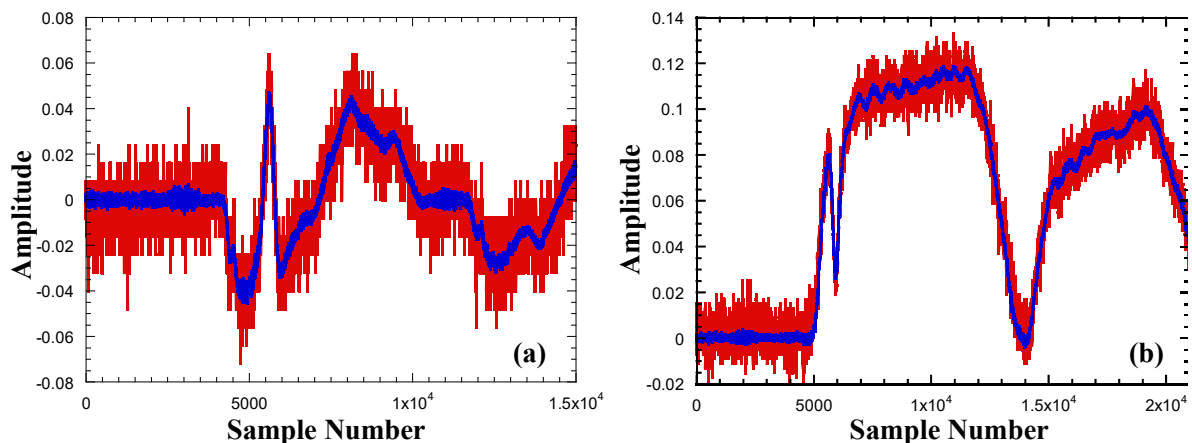


Figure 5.11: Noisy and De-noised experimental signal using SSM+WF with $a = 4$ and $\beta = 0.5\%$ (a) Test 1 and (b) Test 2; For both test signals each sample number corresponds to 0.2 ns real time.

5.5.5 Improvement in Velocity Measurement

In present section the improvement in estimated free surface velocity of target plate after applying the proposed de-noising method on the two sets of quadrature fringe shift traces (90° phase difference between the two traces) recorded using VISAR in two separate experiments has been discussed. Figure 5.12 (a and b) shows the original noisy quadrature coded signals of the two tests (Test 1 and Test 2) along with the signals de-noised using SSM+WF filter with parameter as $a = 4$ and $\beta = 0.5\%$. These signals were used to estimate the free surface velocity history of the target plate by counting the number of interference fringes shifted as a function of time. Phase unwrapping algorithm is used to count total number of integral ($N_I(t)$) and fractional fringes ($N_F(t)$).

The estimated velocity profiles using original noisy quadrature coded record (Red trace) and de-noised record (Blue trace) is presented in Fig. 5.13a and 5.13b corresponding to Test 1 and Test 2. The major improvement in accuracy and precision of velocity measurement in terms of peak velocity is presented in Table 5.4. Here accuracy is taken as the closeness of the mean peak estimated free surface velocity to the peak flyer velocity measured from the other stable method just before the impact. It may be noted that the experiments were done in symmetric configuration and for symmetric configuration the peak free surface velocity is expected to be almost equal to the flyer velocity.

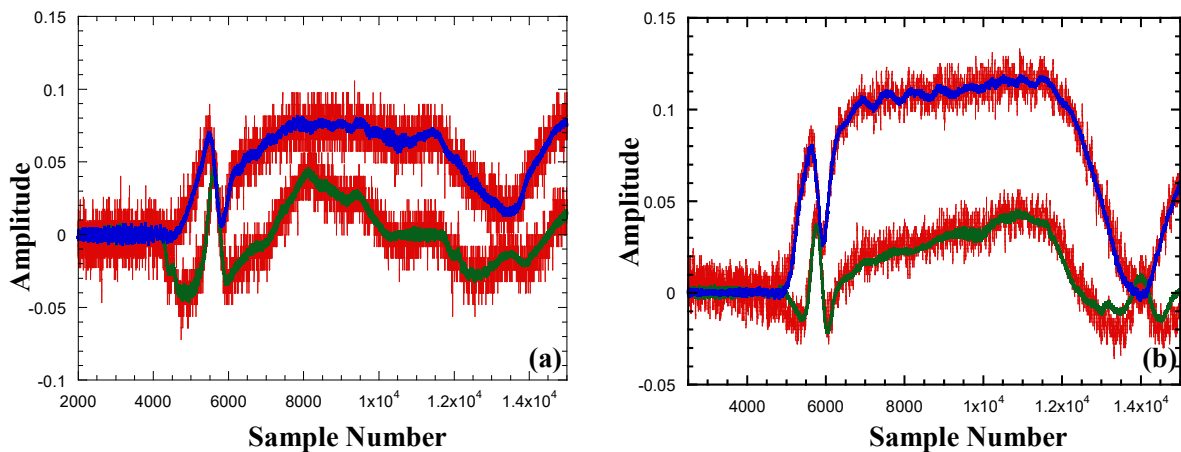


Figure 5.12: Original noisy and filtered quadrature fringes for (a) Test 1, (b) Test 2

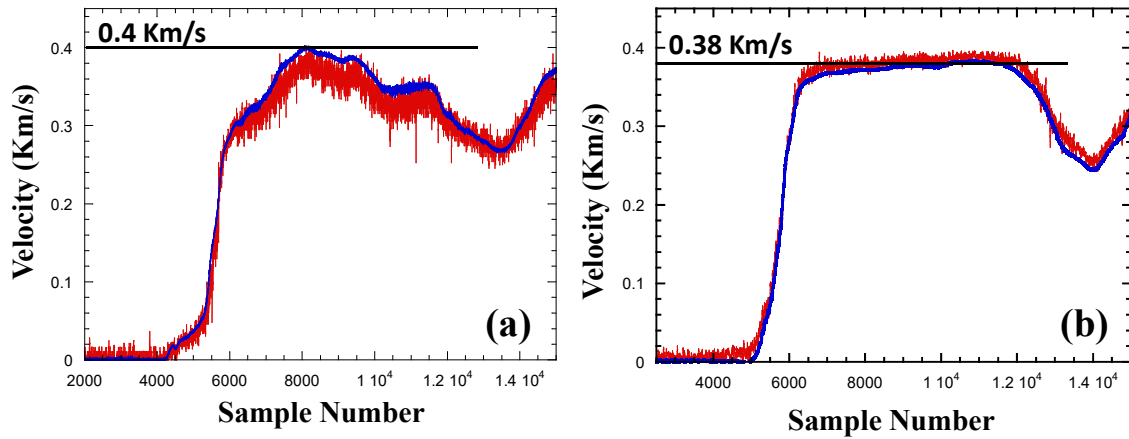


Figure 5.13 Estimated Velocity profiles using original noisy signal (Red trace) and filtered signal (Blue trace) using proposed filter (SSM+WF) along with measured peak velocity for (a) Test 1, (b) Test 2.

From table 5.4 it is clear that the accuracy has improved from 2.10% to 0.52% and precision has improved from 1.70% to 0.46% for Test 2, whereas for Test 1, these figures are 6.25% to 1.00% and 4.58% to 1.31%, respectively, due to implementation of proposed filter.

5.6 Summary

In this chapter, a method for de-noising of multi-frequency electrical signals generated and recorded by the VISAR instrument during the shock compression of the materials achieved in plate impact experiments conducted using single stage gas gun has been

TABLE 5.4
Uncertainty improvement in free surface velocity estimation
(Peak Velocity Test 1: 0.40 km/s and Test 2: 0.38km/s)

	Test 1				Test 2			
	Mean (km/s)	Standard Deviation	Accuracy In %	Precision In %	Mean	Standard Deviation	Accuracy In %	Precision In %
Original Noisy Data	0.375	0.0086	6.25	4.58	0.388	0.0033	2.10	1.70
Filtered Data with SSM+WF	0.396	0.0026	1.00	1.31	0.382	0.00089	0.52	0.46

presented. The proposed method utilizes capabilities of spectral subtraction method for separating signal components from noisy signal corrupted by additive, non correlating noise, using scaling factor and noise floor in non-linear fashion. The estimated/separated signal components and noise estimates obtained during non activity of the signal are used to implement Wiener filter. The proposed SSM+WF filter is optimized for the scaling factor of 4, at which the RMSE values are minimum for all noise levels in the range from 0 dB to 30 dB and found to be insensitive for the noise floor selection.

The percentage change in the RMSE value of de-noised standard signals with the noise floor variation from 0.5% to 10% of the noise power spectrum has been found to be less than 4% for proposed SSM+WF de-noising method while the same is found to be up to 45% for SSM method. The standard signals are also de-noised using commonly used methods like adjacent point averaging and wavelet shrinkage methods. It was shown that the proposed method has lowest RMSE error as compared to all other methods. The percentage change of SNR improvement calculated for the de-noised experimental VISAR signal using SSM+WF method has been found to be ~8.5% for noise floor changing from 10% to 0.5%, whereas the same calculated using SSM method is up to ~15%. This further justifies the insensitivity of the proposed SSM+WF filter system as compared to only SSM filter for variation in noise floor. The improvement in accuracy using SSM+WF is determined to be 6.25% to 1.00% and that in precision is estimated to be 4.58% to 1.31% for signals recorded in test 1. These for test2 are evaluated to be from 2.10% to 0.52% and 1.70% to 0.46%, respectively. It has been demonstrated that the proposed Wiener filter reinforced with spectral subtraction, i.e. SSM+WF filter, performs better and is simple to implement in de-noising fringe signals recorded using VISAR. Some of the key advantages of proposed system are listed below:

- i. No parameter optimization is required i.e. out of the two parameter of SSM method, first parameter scaling factor is optimized for 4 ($a = 4$) and proposed filter (SSM+WF) is insensitive towards second parameter noise floor (β).
- ii. Proposed method is adaptive in nature as all required data is derived from the measured signal such as noise spectrum from the portion of signal where there is no Doppler shift and signal spectrum from the output of the spectral subtraction method. Hence any variation in input signal such as recording instruments, material property etc are automatically adapted in the process.
- iii. Filter coefficients are varying between 0 and 1 depending on the SNR value at a particular frequency component. Further it is a zero phase filter i.e. the output of the filter does not alter the phase of the input signal. Hence there is no added phase to the original signal leading to no change in the phase information of the recorded signal during the de-noising process.

Implementation is relatively simple and can be added as a functional block in signal processing of the measured signals.



Chapter 6

Characterization of VISAR using LTI Model And Inverse Solution for Two Delay System

6.1 Introduction

The term simulation refers to the entire process of constructing, using and justifying a model that involves analytically intractable mathematics [129]. The results of the computer simulation are used to complement and validate real-world experimentation and/or explore physical and conceptual hypotheses related to such experimentation. Computer simulations are considered as a tool used by scientists in scientific domain and these should be subjected to similar rigorous stages that goes into constructing any other precise scientific instrument. Complex and contemporary scientific instruments like velocity interferometers, e.g. VISAR used for measuring time varying material velocity in high strain rate experiments require understanding of the instrument in much greater detail owing to its complexity and refinements those have been carried out by Barker and others [24 - 30] since its initial development. Data generated from such complex scientific instruments needs careful and rigorous attention and analysis method to get desired result. In view of this, a Linear Time Invariant (LTI) model of VISAR has been developed and validated with the help of experiments. Present chapter describes the same. The outcome of the model is discussed and some of the data processing techniques and modifications in instrument are proposed for improving capability of VISAR.

6.2 VISAR and its Governing Equations

In this section general description of the instrument and governing equations of the VISAR is discussed. Final equations will be presented in the form so that they can be used directly for modeling the instrument.

6.2.1 Instrument Description

Though a brief discussion of VISAR has already been provided in section 4.2 mainly concentrating on SRS, in present section the instrument is discussed in little detail by keeping model development in mind. VISAR is essentially a modified Michelson interferometer which measures the differential Doppler shift as a function of time by beating two light signals, reflected from moving free surface of the target material, at two different instants of time separated by a small time interval of order of a fraction of nanosecond to few nanoseconds. Block diagram type schematic of the instrument is presented in Fig 6.1. As displayed in figure the defused reflected laser light from the target is divided in two different parts. One of the parts is delayed by placing optical slab/etalon while the other part is allowed to interfere without delay. The time resolved beat frequency is then utilized to deduce the free surface velocity history. The typical free surface velocities in plate impact experiments using gas guns or explosives could range from few hundred m/s to few km/s with corresponding strain rates generated in the target material ranging from $\sim 10^4/s$ to $\sim 10^8/s$. The target free surface reaches such high velocities within a fraction of microseconds.

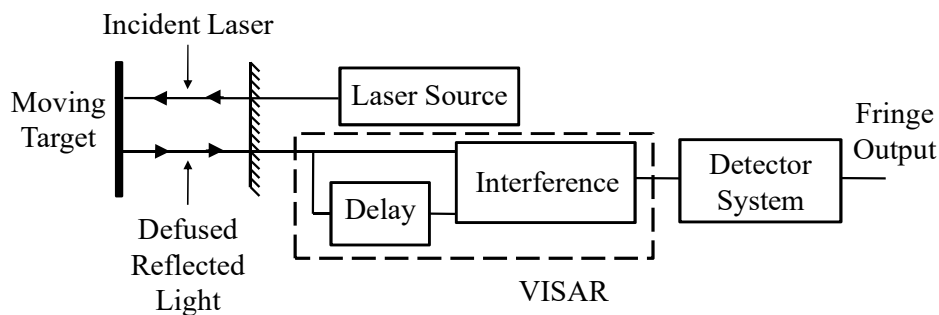


Figure 6.1: Schematic of VISAR with experimental setup

The more accurate representation of such fast changing velocities requires not only fast linear detectors and recording systems but also the proper optimization of interferometer design parameters such as VISAR delay time ‘ τ ’ or fringe constant to generate a sufficient number of fringes. The closer is the measured free surface velocity history to the actual one, the more realistic will be the physical or mechanical quantities, *e.g.* dynamic yield strength, spall strength etc., derived from this.

6.2.2 Governing Equations

A brief presentation of governing equations and analysis technique which are discussed in detail by Barker and Dolan [114, 115] is given here. Conventionally VISAR works on the optical differentiation of the input displacement history of the target using the time step of the optical delay (τ) of the instrument decided by the length and material of the etalon used i.e. VISAR delay (τ) [114, 115]. The generated optical phase history which is proportional to the differential position history of the target, is converted to velocity profile using fringe constant (F_C) given as the velocity per fringe constant of the instrument. It may be noted that one fringe corresponds to increase in the phase value by 2π . Velocity of the target from the measured fringes/phase history is calculated as [114, 115].

$$y(t) = F_c \times F(t) = \frac{\lambda_0}{2\tau} \times \frac{\Phi(t)}{2\pi} \quad (6.1)$$

Where $y(t)$ is the velocity of the target or instrument/system output, and $F(t)$ is the measured fringe count. λ_0 is the wavelength of the laser used. Appendix A contains the derivation of the Equ. 6.1. Here $\Phi(t)$ is the phase history of the target and is given as [114, 115]

$$\Phi(t) = \frac{4\pi}{\lambda_0} [x(t) - x(t - \tau)] \quad (6.2)$$

Where $x(t)$ and $x(t-\tau)$ is the position of the target at two different time instances separated by the optical delay, τ . Let us now relate the phase with the distance $[x(t) - x(t - \tau)]$ as given in Equ. 6.2, and discussed in detail by Dolan [115]. In case of VISAR, output phase is proportional to the difference in phases at two different time instances separated by known time. Phase of the sinusoidal output of the system is given as:

$$\Phi(t) = \phi(t-t_1) - \phi(t-t_2) \quad (6.3)$$

with $\phi(t-t_1)$ and $\phi(t-t_2)$ are the phase of the reflected laser source at two different time instances. Here $\phi(t)$ is given as

$$\phi(t) = \omega_0 t + \phi_0 = \frac{2\pi c_0}{\lambda_0} t + \phi_0 \quad (6.4)$$

where c_0 is the speed of light. This phase is related to the target position in following way

$$\phi(t_1) = \omega_0 (t_1 - 2t_r) + \phi_0 = \omega_0 \left(t_1 - \frac{2}{c_0} (x(r) - x(t_1)) \right) + \phi_0 \quad (6.5)$$

Here $x(r)$ is the position of measurement plane i.e. location of optical probe and $x(t_1)$ is the position of the target at the point of measurement at time t_1 . Similarly let $\phi(t_2)$ is the phase related to position of target at time t_2 . The Equ. 6.3 can be rewritten as follows by using Equ. 6.5:

$$\Phi(t) = \phi(t-t_2) - \phi(t-t_1) = \omega_0 (t_2 - t_1) + \frac{2\omega_0}{c_0} (x(t-t_1) - x(t-t_2)) \quad (6.6)$$

As, $t_2 = t_1 + \tau$, Equ. 6.6 reduces to

$$\Phi(t) = \omega_0 \tau + \frac{2\omega_0}{c_0} (x(t) - x(t-\tau)) \quad (6.7)$$

Here $\omega_0 \tau$ is constant and depends on the un-shifted laser wavelength and optical delay. Equation 6.7 relates optical phase of the output signal to the differential target position and can be utilized for model development.

It is clear from Equ. (6.1) and (6.2) that the velocity history measured by the VISAR is the differentiation of the displacement using time step ‘ τ ’. The optical delay ‘ τ ’ is defined by the condition of equal virtual lengths of two legs of interferometer [75, 78, 115]. The concept of virtual length and optical delay is the key difference between displacement interferometer (sensitive to position) and VISAR (sensitive to differential position). The condition of virtual length is introduced in VISAR by placing an etalon in one of the leg of interferometer making the lengths of two legs physically different but virtually same. The condition of equal virtual length of the two legs (zero virtual separation) is required for fringe formation while physically different length of the two legs created by etalon is required to eliminate the shortcomings of the displacement interferometer [75].

6.3 Linear System: Properties and Solution

6.3.1 General LTI system and Convolution Sum as Solution

A linear system is a mathematical model of an instrument based on the use of linear operators. A general deterministic system can be described by transfer function $h(n)$ that maps input $x(n)$ as a function of time, to an output $y(n)$. Linear system transfer function behaves like a black box description of the system as shown in Fig. 6.2. The important basic properties of the linear system are homogeneity, additivity and shift invariant [130]. Homogeneity implies, change in amplitude of the input signal corresponds to change in amplitude of output signal. Additivity implies, if system is linear for two independent input signals than addition of these two input signals corresponds to addition of respective output signal. Shift invariant property indicates that the shift in input signal will result only identical shift in output signal. Mathematically these properties can be expressed as [130]

$$\text{if } x(n) \Rightarrow y(n) \text{ then, } kx(n) \Rightarrow ky(n) \qquad \text{Homogeneity}$$

$$\text{if } x_1(n) \Rightarrow y_1(n) \text{ and } x_2(n) \Rightarrow y_2(n);$$

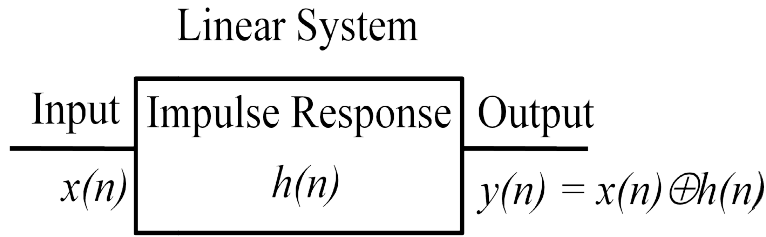


Figure 6.2: Black box representation of Linear System

then $x_1(n) + x_2(n) \Rightarrow y_1(n) + y_2(n)$ *Additivity*

if $x(n) \Rightarrow y(n)$; then $x(n + s) \Rightarrow y(n + s)$ *Shift Invariant* (6.8)

As discussed in [131], convolution sum method can be used for analyzing the behavior or response of linear systems. It requires decomposition or resolving the input signal into a sum of elementary signals. The elementary signals are selected so that the response of the system to each signal component is easily determined. Using the linearity property of the system, the responses of the system to elementary signals are added to obtain total response of the system to the given input signal. Suppose the decomposition of the input signal $x(n)$ is given as [131]

$$x(n) = \sum_{k=-\infty}^{\infty} x(k)\delta(n-k) \tag{6.9}$$

Where $\delta(n)$ is the unit sample sequence. The right hand side of the above equation is the summation of an infinite number of unit sample sequence $\delta(n-k)$ with associated amplitude equal to $x(k)$. Let unit sample sequence response of the linear system be

$$y(n,k) \equiv h(n,k) = T[\delta(n-k)] \tag{6.10}$$

Here 'n' is the time index and 'k' is a parameter showing the location of the input impulse. If $x(k)$ is the amount by which input impulse sequence is scaled then corresponding scaled output will be $x(k)h(n,k)$. The complete response of the system to the input signal $x(n)$ can be written as the sum of weighted outputs as follows:

$$y(n) = \sum_{k=-\infty}^{\infty} x(k) \Gamma[\delta(n-k)] = \sum_{k=-\infty}^{\infty} x(k) h(n,k) \quad (6.11)$$

Here superposition and linearity properties of the linear system are used. The expression is a function of both $x(n)$ and the response $h(n,k)$ of the system to the unit impulses $\delta(n-k)$ for $-\infty < k < \infty$. For time invariant linear system the above expression simplifies to:

$$y(n) = \sum_{k=-\infty}^{\infty} x(k) h(n-k) \Leftrightarrow x(n) \oplus h(n) \quad (6.12)$$

Equation 6.12, which is a convolution sum, gives the response $y(n)$ of a linear time invariant system as function of the input signal $x(n)$ and unit sample (impulse) response $h(n)$. In other words input $x(n)$ is convolved with impulse response $h(n)$ to yield the output $y(n)$.

6.3.2 VISAR as LTI System and its Characteristic

Work on the black box model of the linear system is required to find out the impulse response $h(t)$ of the system. VISAR can be thought of as a system with input as the position history of the target and measured output as phase history of the target. With this, the Equ. 6.1 can be rewritten as:

$$y(t) \equiv \frac{\lambda_0}{4\pi} \phi(t) = x(t) - x(t - \tau) \Leftrightarrow y(t) = x(t) \oplus h(t) \quad (6.13)$$

Equation 6.13 indicates that, to develop the model for the VISAR, having displacement history as input and corresponding phase value as output, one needs to determine impulse response $h(t)$ of the instrument which can provide differential displacement value. The possible structure of the impulse response $h(t)$, is given as

$$h(t) = \delta(t) - \delta(t - \tau) \quad (6.14)$$

Here impulse response $h(t)$ consists of positive and delayed negative impulse [116]. To get the solution or the response of the system, position history $x(t)$ of the target is convolved

with the impulse response $h(t)$ of the instrument. The amount of delay depends upon the optical delay ' τ ', which is the transit time difference between the two legs of the interferometer and is given as [75]:

$$\tau \equiv t_2 - t_1 = \frac{2l}{c_0} \left(\eta - \frac{1}{\eta} \right) \quad (6.15)$$

Where l is the length of etalon, η is its refractive index and c_0 is the speed of light. From Equ. (6.15), it is clear that ' τ ' is purely the function of the size and refractive index of the etalon. Further, considering the correction due to dispersion, the expression gets modified as follows [115]:

$$\tau = \tau_0 \left(1 + 2\delta \frac{v}{c_0} \right) \quad (6.16)$$

Here v is the velocity of the target, τ_0 uncorrected delay time and δ is a dimensionless parameter for a given etalon material and operating wavelength. In present case etalon material is fused silica having $\delta = 0.0266$ for operating wavelength of 532 nm. The effect of dispersion correction, on the uncorrelated delay time ' τ_0 ' for peak velocities up to 1 km/s, is negligible hence for all practical purposes delay time ' τ ' is assumed to be constant in deriving the model parameter. This allows us to consider $h(t)$ as time invariant impulse response and developed system defined by $h(t)$ as linear time invariant system for VISAR. This also implies that convolution sum, Equ. (6.12), can be used for generating solution for the model. Frequency response of impulse function $h(t)$ of VISAR linear model obtained by performing Fourier analysis of the Equ. 6.14 [116] can be expressed as:

$$H(f) = 1 - \exp(-j2\pi f\tau) \quad (6.17)$$

where $H(f)$ is the frequency domain response of $h(t)$ and f is the frequency. The frequency and phase response of the $h(t) \Leftrightarrow H(f)$ is plotted in Fig. 6.3. From the expression of frequency response and spectral plot of the impulse function $h(t)$, it is inferred that $H(f)$

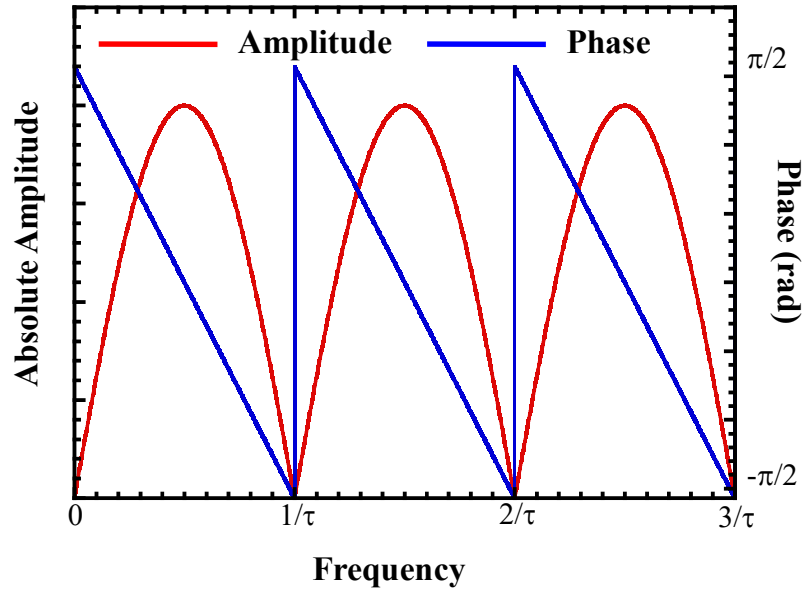


Figure 6.3: Frequency and Phase plot of VISAR Linear Model

is having periodic zeros at frequency points which are integer multiple of $1/\tau$. This is the classic explanation of missing fringes in the VISAR. Let us assume that position history $x(t)$ is sinusoidal with frequency equal to integer multiple of $1/\tau$, alternatively the distance travelled by the moving target surface in τ time equals to integer multiple of $\lambda_0/2$ (periodic with ' τ '), in such case the VISAR will not be able to respond or the phase change is equal to integer multiple of 2π (Equ. 6.1) and fringe will not be recorded. In other words, due to the presence of zeros in the system response function $H(f)$ at the frequencies equal to integer multiple of $1/\tau$, the spectral component present in position and/or velocity history were removed. This explains the inability of VISAR to measure signals (position and/or velocity history) exactly periodic with delay time ' τ '. In practical cases the position history is neither sinusoidal nor linear, hence only the components of the velocity profile which are having frequencies multiple of the $1/\tau$, will be eliminated by the system zeros of the impulse response function. The phase of the system impulse response $H(f)$, is linear, that means the delay introduced by the model is frequency independent and is same for all frequency components [131]. This delay in time domain is given as:

$$T_d = \frac{N-1}{2 \times F_S} \quad (6.18)$$

Where N is number of tap (coefficients in impulse transfer function $H(f)$) and F_S is the sampling frequency. Group time delay introduced by the developed VISAR model is equivalent to $\tau/2$. Application of this delay introduced by the model in Equ. (6.1), gives the standard VISAR equation [11] for velocity profile as:

$$y(t - \tau/2) = F_C \times F(t) \Rightarrow \frac{\lambda_0}{2\tau} \times F(t) \quad (6.19)$$

6.4 Validation of Developed Model

6.4.1 Flow of Data and Expected Signal

Figure 6.4 shows the various steps involved in predicting the fringe pattern for a simulated/artificially synthesized free surface velocity history used as the input. Correspondingly Fig. 6.5 shows the expected signals at each step.

As mentioned in section 6.2.2, VISAR is sensitive to only acceleration and deceleration, the zero and constant velocity yields constant phase output. As a first step towards the verification of the model, velocity profile used as input has been synthesized from the artificial data of constant acceleration, constant velocity and constant deceleration (Fig. 6.5 a). All data points are generated at the sampling interval of 0.2 ns with peak velocity of 1 km/s reached in time of 10 ns. The displacement profile calculated for this velocity profile as shown in Fig. 6.5b has convex, linear and concave displacement profiles corresponding to three different regions of the velocity profile. The delay τ used in the VISAR model is 1 ns and the dynamic response of the recording system has been assumed to be sufficiently large to capture all the phase change that is being converted to sinusoidal fringe pattern. The phase profile and corresponding fringe movement patterns are displayed in Fig. 6.5c and Fig. 6.5d, respectively. As expected, for constant velocity region, phase is

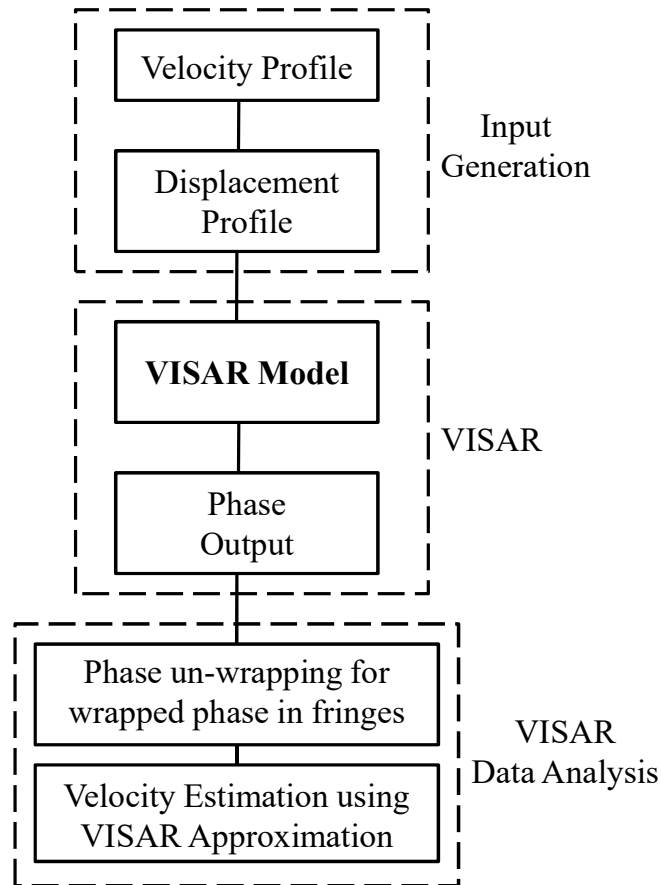


Figure 6.4: Steps used in Model Validation

constant. Also direction of phase change in acceleration region is opposite to that in deceleration region. This is the unique feature of the VISAR which gives it ability to distinguish between acceleration and deceleration. The change in the direction of phase can be identified from the quadrature coded fringe record (Fig. 6.5d). Further, in Fig. 6.6, the homogeneity and additive property of the developed model using the above mentioned synthesized velocity profile is presented.

As shown in Fig. 6.6a, to demonstrate homogeneity property, signal 2 is chosen as double of the signal 1. This signal is then passed through the developed model. Corresponding model output is presented in Fig. 6.6b, as output 2, which is double of the output 1, corresponding to signal 1

Similarly to check additivity three signals are required where one signal is the to get

signal 4. The output signal corresponding to signal 1, Signal 3 and Signal 4 are displayed in Fig. 6.6b as output 1, output 3 and output 4. As is clear from the figure output 4 is equal to sum of output 1 and output 3, satisfying the additivity.

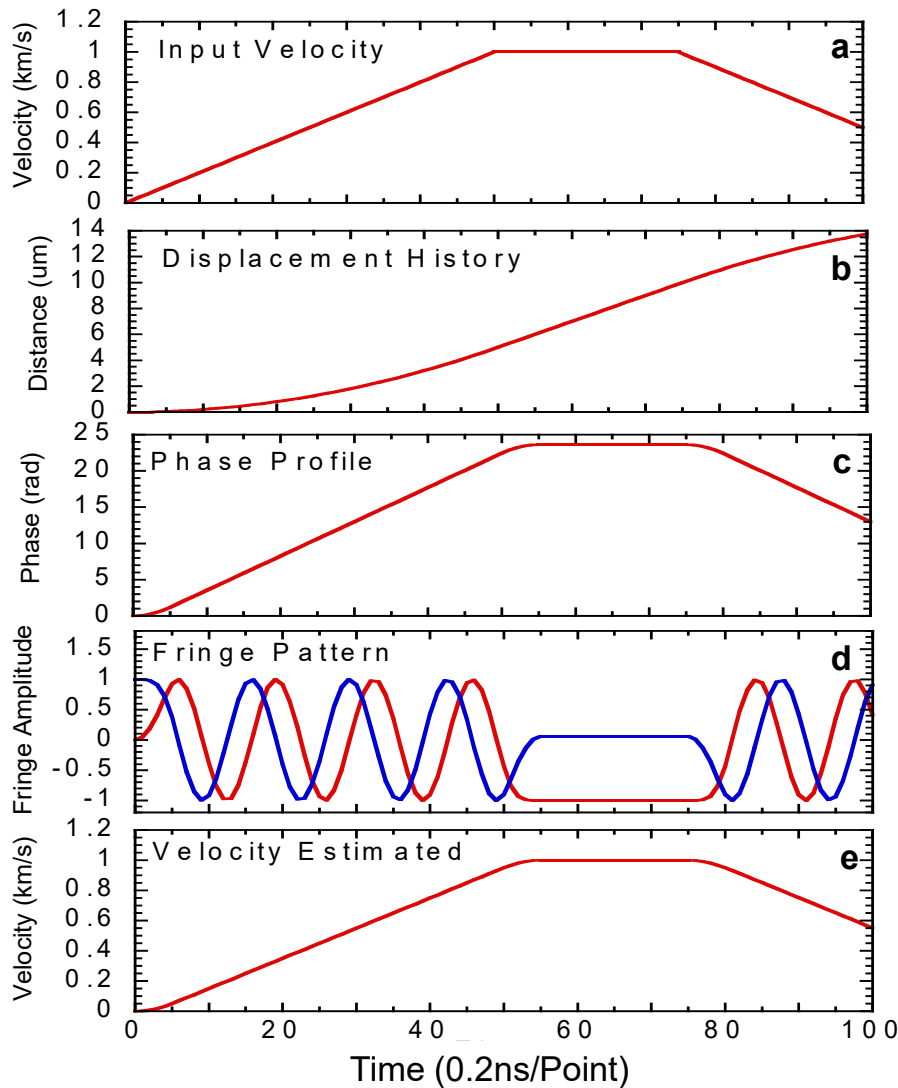


Figure 6.5: (a) Numerically generated velocity data with constant acceleration and deceleration. (b) Displacement history corresponding to generated velocity data, (c) Generated phase profile using Linear Model of the VISAR, (d) Phase information wrapped in periodic $0-2\pi$ sinusoidal fringe pattern, (e) Estimated velocity from the generated fringe pattern using VISAR approximation.

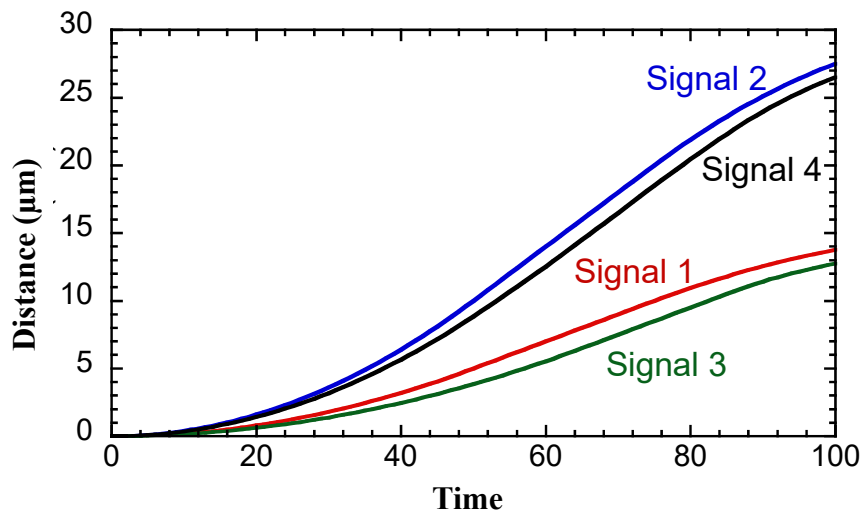


Figure 6.6(a): Signal 1: Numerically simulated displacement history; Signal 2: Twice the Signal 1 [$2 \times \text{Signal 1}$]; Signal 3: Numerically simulated displacement history, independent of Signal 1; Signal 4: Addition of Signal 1 and Signal 3 [$\text{Signal 1} + \text{Signal 3}$]

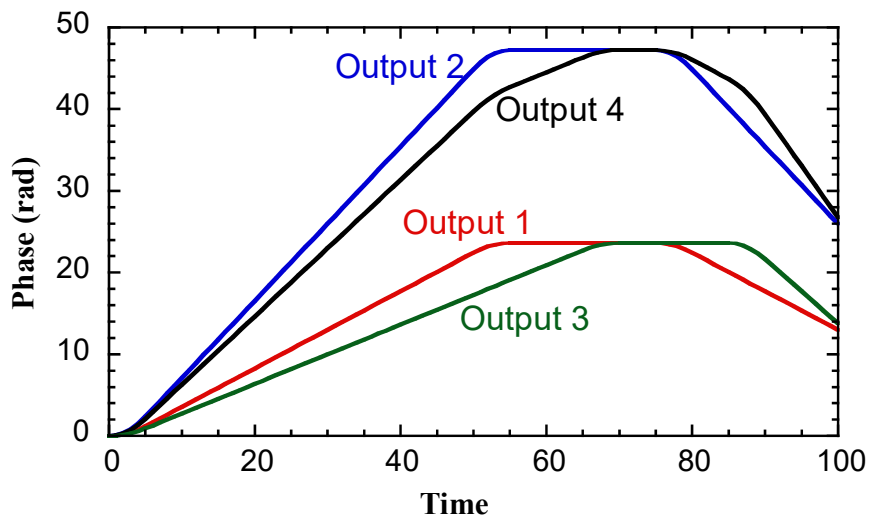


Figure 6.6(b): Output 1 to Output 4 are phase output of the model corresponding to displacement history from Signal 1 to Signal 4.

6.4.2 Experimental Setup for Validating Model with Experimental Data

Next, attempt was to validate the model by using simulated free surface velocity profile of Al2024-T4 alloy of aluminium. For this purpose the impact experiment is simulated using hydrodynamic code considering Mie-Grunesien Equation of State of the aluminium alloy and Rankine-Hugoniot jump conditions. The simulation was performed for the plate impact experiment in symmetric impact condition with impact velocity chosen to be 0.56 km/s [19]. The free surface velocity profile calculated from the simulation has been used as input to generate the expected fringe profile of the VISAR employing the developed model.

In order to validate the fringe profile so generated using developed model, a plate impact experiment has been carried out under the conditions identical to those used in hydrodynamic simulations. Schematic of the experimental setup is similar to that displayed in Fig. 5.1. The 5 mm Al2024-T4 flyer plate is accelerated to the velocity of 0.56 km/s in 63 mm bore diameter single stage light gas gun [16] and impacted on the stationary target of Al2024-T4 having thickness 8 mm. An optical probe collected the reflected laser light from the target free surface and transported it to VISAR instrument. Output of the instrument is recorded using PMT and DSO. The delay time τ used in the experiment was 1ns, same as that used for the modelling.

6.4.3 Comparison of Simulated and Experimentally Recorded Fringe Pattern

For validation of the fringe signal generated using model on the simulated free surface velocity history it was compared with that recorded in actual experiment. Correlation was one of the criteria utilized for comparison of the two signals. In present case, comparison of fringes in time as well as frequency domain has been carried out. Correlation of two signals [132] in time domain is given as:

$$r_{xy}(l) = \sum_{n=-\infty}^{n=\infty} x(n)y(n-l) \quad l=0, \pm 1, \pm 2, \dots \quad (6.20)$$

Where $x(n)$ and $y(n)$ are the two signals (in present case one corresponding to the experimental signal and other corresponding to that generated using model to simulated free surface velocity profile) and l is the time lag in one of the signal. Whereas, the spectral coherence of the two signal is expressed as:

$$C_{xy}(f) = \frac{|P_{xy}(f)|^2}{P_{xx}(f)P_{yy}(f)} \quad (6.21)$$

Where, P_{xx} , P_{yy} are the spectral power density corresponding to signal $x(n)$ and $y(n)$, and P_{xy} is the cross power spectral density.

As it is clear from Equ. 6.20, correlation can be calculate by multiplying one signal with the shifted version of another signal from extreme left ($-\infty$) to extreme right ($+\infty$). The value of correlation function $r_{xy}(l)$ is maximum where both signal $x(n)$ and $y(n)$ are in phase or similar. The parameter l defines the lag (difference) present between two signals. The value of $r_{xy}(l) = 1$ (for normalized scale) or $r_{xy}(l) = \max(r_{xy}(l))$ (for absolute scale) indicates that the two signals are similar. For the case of spectral coherence, the spectral coherence coefficient C_{xy} is maximum ($C_{xy}=1$) in the situation where cross spectral power density of the two signals are identical to the multiplication of individual spectral power density. Fig. 6.7a, presents one of the quadrature fringe signal recorded in the experiment and the corresponding fringe signal generated by applying linear model of VISAR on simulated free surface velocity history. The corss-correlation signal in Fig. 6.7b, shows peak value at the time lag of zero ($l=0$), this indicates that there is no absolute difference between the two signal including time lag. Magnitude squared coherence estimate C_{xy} of the input signals $x(n)$ and $y(n)$ is calculated using Welch's averaged, modified periodogram method. The magnitude squared coherence estimate is a function of frequency that indicates how well x corresponds to y at

each frequency. Fig. 6.7c, represents the frequency spectrum of the simulated and experimentally measured signal while Fig. 6.7d, presents the magnitude squared coherence coefficient of the two signals. As depicted in Fig. 6.7d, the value of magnitude squared coherence is near to 1, for frequencies corresponding to signal frequency (upto 5 MHz as displayed in Fig. 6.7c), indicating that the frequency content of the two signals are close to each other and they represent almost identical signals.

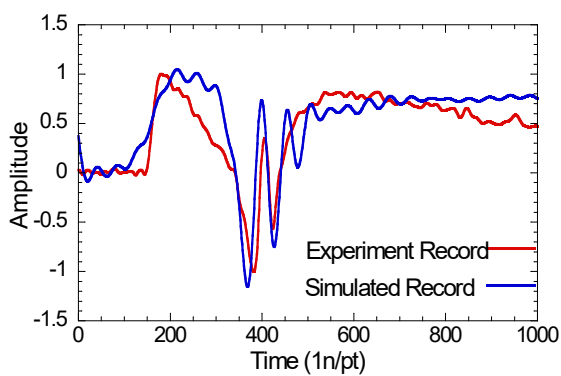


Figure 6.7a: Experimental as well as Simulated Fringe pattern

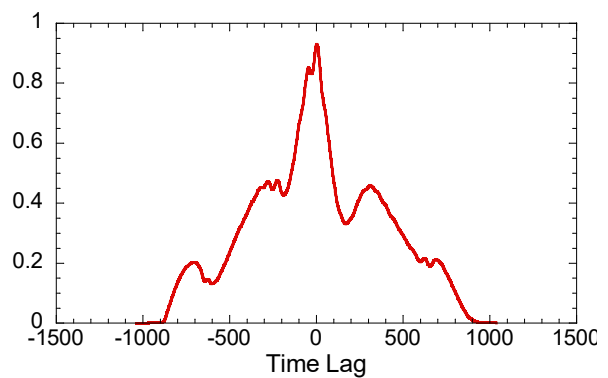


Figure 6.7b: Cross correlation between Experiment and simulated fringe pattern

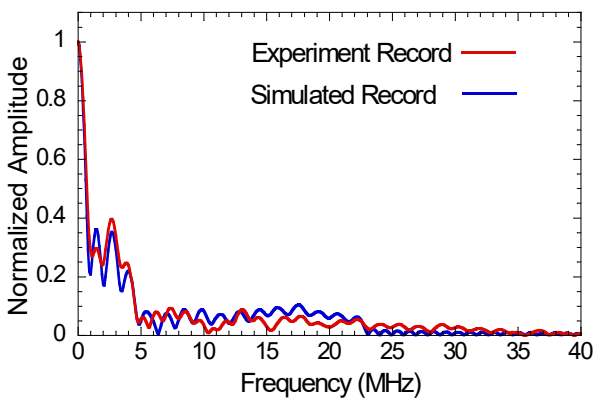


Figure 6.7c: Frequency Spectrum of both signals (Experiment and Simulated)

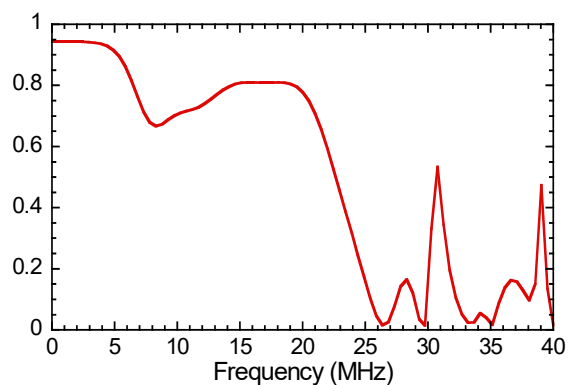


Figure 6.7d: Mean Square Coherence between Frequency Spectrum of both signals (Experiment and Simulated)

6.5 Discussion on VISAR Characteristic

Present section attempts to relate instrument delay ‘ τ ’ with the required detector response and bandwidth of the VISAR. For instance, consider two fringe profiles (Fig. 6.8a) corresponding to two different delays ‘ τ ’ such that one delay is twice the other, for a given free surface velocity history. For these two different ‘ τ ’ the total number of fringes can be calculated using expression:

$$F = \frac{V_{peak} * 2 * \tau}{\lambda_0} \tag{6.22}$$

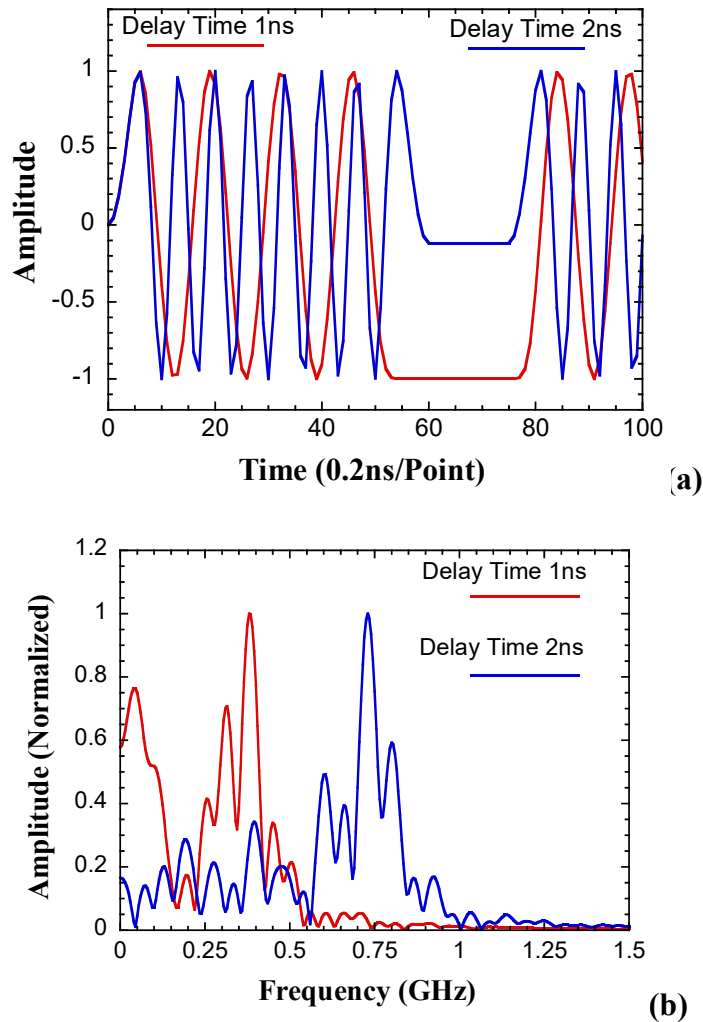


Figure 6.8: (a) Model generated fringe pattern for two different delays; (b) Frequency content of the fringes

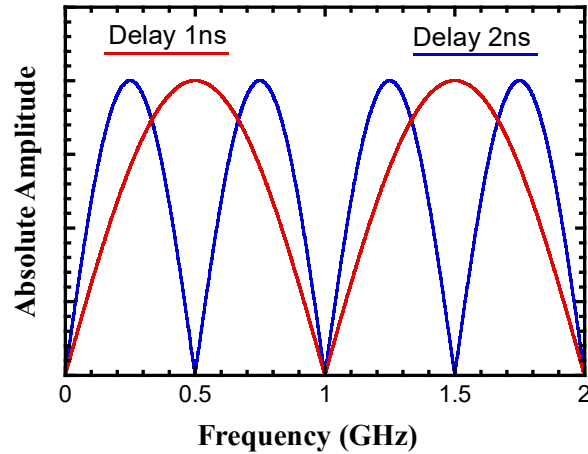


Figure 6.9: Comparison of the spectrum response of VISAR for different delay ‘ τ ’

Where F is total number of fringes, V_{peak} is peak target velocity, and λ_0 is wavelength of the laser source. From the Equ. 6.22, it is clear that for same input velocity the number of fringes generated in system having larger delay will be more, i.e. in same amount of time more number of fringes are shifted. This situation is presented in Fig. 6.8a, and corresponding frequency contents derived from Fourier analysis of the fringe patterns is shown in Fig. 6.8b. As evident from the Fig. 6.8b, the the frequency content of the fringe data corresponding to smaller ‘ τ ’ is less as compared to that for larger ‘ τ ’. From the figure and discussion it is clear that the larger delay will generate more number of fringes thereby, improving the overall resolution of the instrument provided detection system does not limit the response.

On the other hand according to Equ. 6.17, Fig. 6.3 and Fig. 6.9, the use of larger delay ‘ τ ’ reduces the useful frequency band (bandwidth of the first lobe). Hence, while deciding instrument delay care must be taken about the dynamic range of the velocity rise to be measured and detectors should be selected accordingly.

6.5.1 Different Modes of VISAR Operation

Equation 6.2 represents the phase output of the VISAR instrument. For the case, where instrument delay ‘ τ ’ is small as compared to the rise time of the velocity of target free

surface, the instrument works in ‘short delay’ mode. This mode is also called derivative mode as $\Phi(t)$ can represent derivative of displacement i.e. true velocity of the moving target [5, 10].

This is expressed as:

$$\Phi(t) \propto (x(t) - x(t - \tau)) \Rightarrow \tau \times \frac{dx(t)}{dt} \Rightarrow \tau \times v(t) \quad (6.23)$$

In ‘short delay’ or derivative mode the phase output of VISAR is proportional to the velocity of the moving target surface. In other case, where, instrument delay is comparable with the rise time of the velocity of target free surface, the phase output remains proportional to the difference in position history of the target. This situation or mode of operation is called

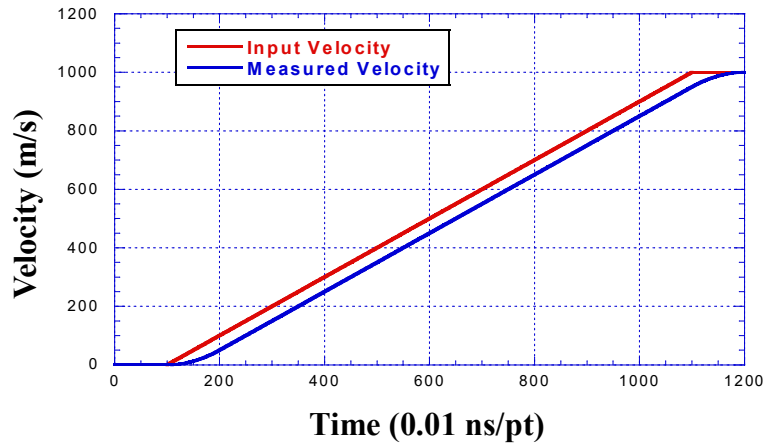


Figure 6.10(a): Short Delay Mode, i.e. VISAR instrument delay \ll Rise time of the velocity of target free surface

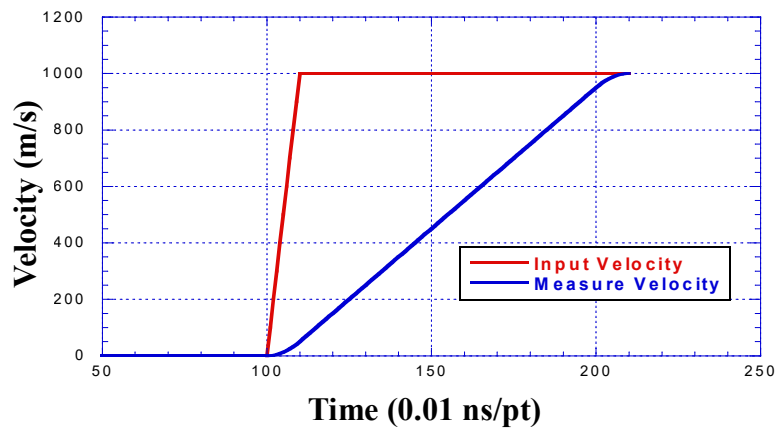


Figure 6.10(b): Long Delay Mode, i.e. VISAR instrument delay \gg Rise time of the velocity of target free surface

‘long delay’ or difference mode [5, 10]. Instrument response under these two conditions is represented in Fig. 6.10a and 6.10b, respectively.

As shown in Fig. 6.10a, for first case, i.e. for short delay mode, the measured velocity history is almost same as the input velocity history (or actual velocity history) whereas, for second case (Fig.6.10b), i.e. for long delay mode, the measured velocity history deviates significantly from the actual one with relatively sluggish rise time. It is clear that for second situation the fine features of the velocity profile may be lost during measurement process which may lead to the incorrect interpretation of the experimental data. In yet another example, the performance of the VISAR instrument for three delays such that $\text{delay}_1 > \text{delay}_2 > \text{delay}_3$ with delay 1 less than the rise time of the velocity and delay 2 and delay 3 comparable with the rise time is compared (Fig. 6.11). As is clear from the figure, the shorter the delay closer is the measured velocity profile with actual input velocity profile. For delay 1 the measured velocity profile displays excellent agreement with input velocity profile.

6.6 Inverse Problem Definition

From the above discussions based on the VISAR model and different modes of its operations following few points can be drawn regarding its use in experiments:

- (i) It is clear that longer instrument delay ‘ τ ’, will increase the resolution of velocity measurement as more number of fringes will be generated for same amount of velocity.
- (ii) The required bandwidth of the detection system (PMT and amplifiers) will be more for longer instrument delay as more fringes needs to be detected in same amount of time.
- (iii) The width of the first lobe in frequency response of the instrument is determined by the instrument delay. For longer delay the width of the first lobe is smaller i.e. the dynamic range for the measurement of input velocity will be less.

- (iv) It is to be noted that longer the delay compared to the rise time of the actual velocity (input velocity) less accurate (due to significantly large differences in actual rise time and the measured rise time) will be the measured velocity profile.

In summary the delay of VISAR instrument, which is the time difference between two interfering Doppler shifted lights from the moving target, has to be less as compared to the rise time of the velocity of the target surface. Also, for the VISAR delay more or comparable to the rise time of the velocity, the VISAR response deteriorates even if the bandwidth of the recording system is increased.

In view of the above discussion the general guidelines for the designing of VISAR instrument is to have a detection system with sufficient bandwidth corresponding to the first lobe of the instrument response ($1/\tau$, in terms of frequency components), i.e. sufficient to record dynamics of the moving target surface. For solution of the problem in long delay mode of VISAR, it has been proposed [116] that two VISAR systems with different delay time must be used in the same experiment and the data recorded by two must be combined to get the desirable results. This would also solve the problem of missing frequency corresponding to integral multiple of the $1/\tau$. But, it has not been discussed that how the results of the two

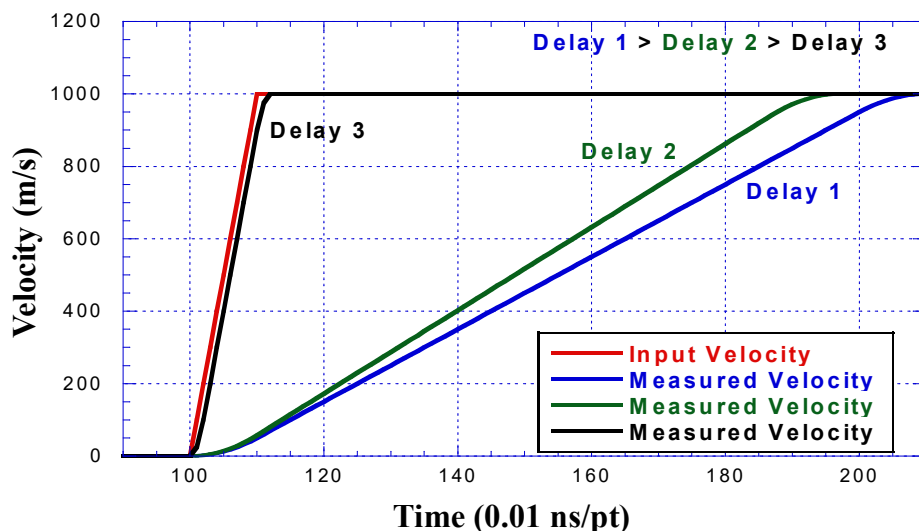


Figure 6.11: Effect of Instrument delay on measurement

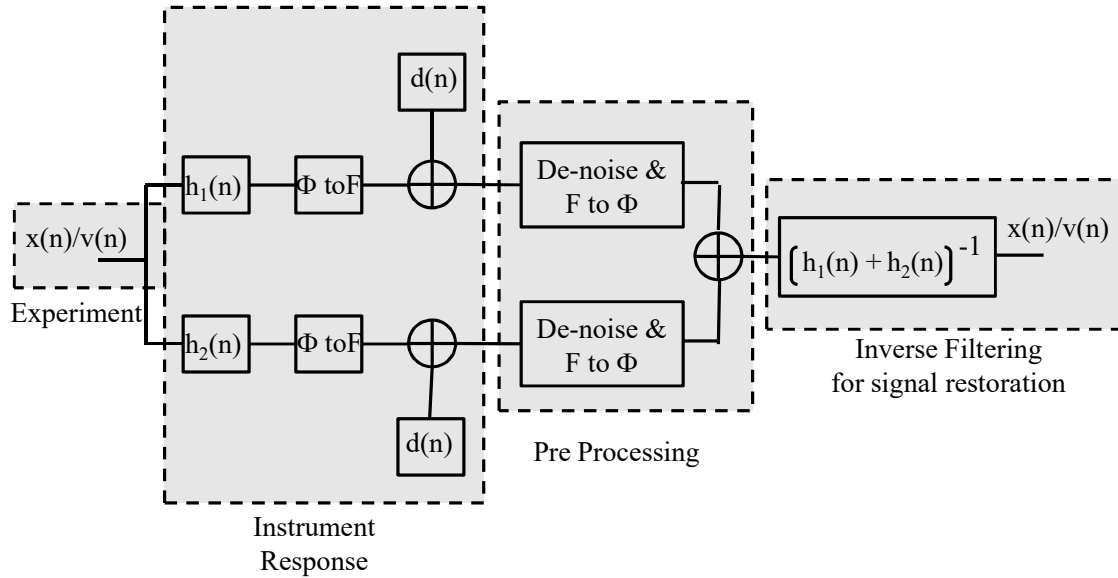


Figure 6.12: Proposed schematic to overcome Instrument Response

VISAR having independent delay can be combined to get the correct history of the moving free surface of the target.

One of scheme proposed in the present work for combining the results of two delay VISAR is presented in Fig. 6.12. The measurement system proposed in Fig. 6.12 has the time resolved target free surface motion during shock propagation as the input. In next step the motion of target free surface is sensed by two VISAR systems having different delays with system response function as $h_1(n)$ and $h_2(n)$. Corresponding to each VISAR system phase (Φ) and fringes (F) are generated and recorded. The recorded fringe signal also contains the additive noise ($d(n)$) incorporated in the signal during the process of detection and recording.

Hence, the proposed scheme of signal processing for the recorded experimental data starts with the de-noising. After de-noising, the fringes are converted into the phase history using phase unwrapping method. The next step in analyzing data of two VISAR systems requires combining the outcome of phase unwrapping step into one signal. Further analysis of the combined signal is carried out by solving inverse of the combined forward system

response $([h_1(n)+h_2(n)]^{-1})$ of the two VISAR systems. The outcome of the inverse of the combined forward system response is the displacement history which can be converted to velocity history by numerically differentiating the same. Fig. 6.13 shows the frequency response of the two VISAR's having different delays and that of the combined response of these two delays. It is clearly seen that the width of the first lob in frequency response has increased substantially and can be utilized to get information which individually delay VISAR could not provide.

The development of desired signal processing method for the two delay VISAR systems requires to answer the question of the type “What could be the input for a given output with known system function?” The answer to this question could be given by inverse problem and its solution. These solutions could be based on the linear processing of data or on the numerical methods to find out solutions of the inverse problem [130, 131].

6.6.1 Introduction To Inverse Problem

In general a forward problem is to compute the output, given a system and the input to

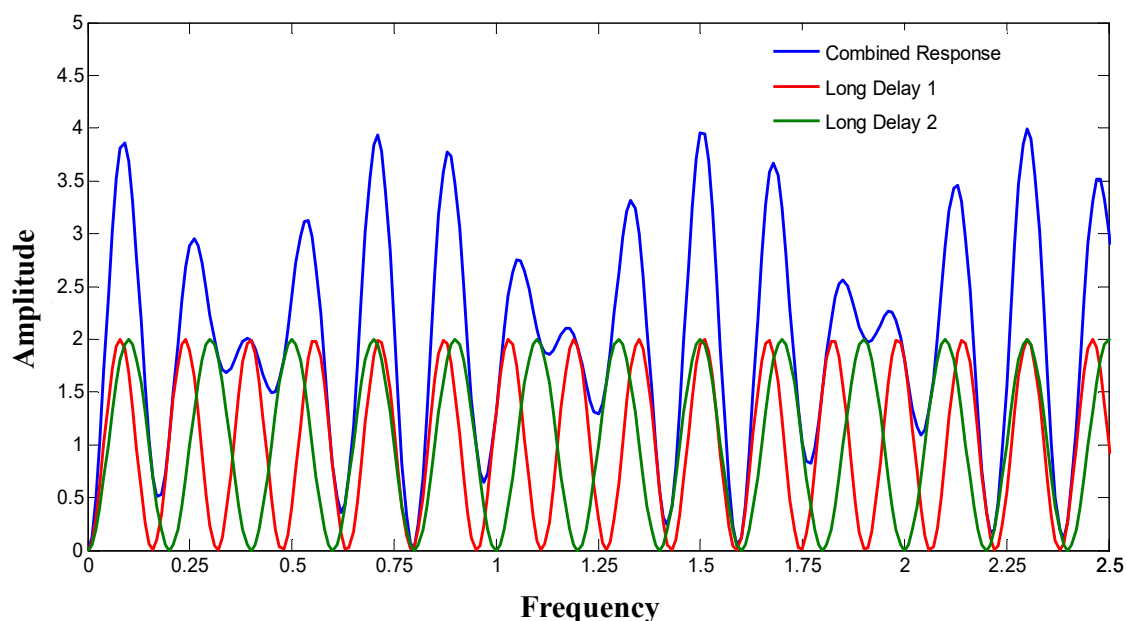


Figure 6.13: System Response of two delay VISAR system

the system. However, the inverse problem arises when it is required to compute information about the internal or hidden data from outside or accessible measurement. Equivalently, the inverse problem is to compute either input or the system parameter. Inverse problems are the important mathematical problems in science and mathematics because they provide us information about those parameters which cannot be observed directly. Let $x(n)$ is the input to the system $h(n)$ and the measured output is $y(n)$. This can be written as

$$\left. \begin{aligned} y_{true}(n) &= x_{true}(n) * h(n) \\ \text{Alternatively, } y(n) &= y_{true}(n) + d(n) = x_{true}(n) * h(n) + d(n) \end{aligned} \right\} \quad (6.24)$$

Here $y(n)$ is the measured output with some error such as noise of measuring system or system error. $y_{true}(n)$ is the true output value based on the actual input signal $x_{true}(n)$ and system model $h(n)$ without any error and system noise. The $d(n)$ is the additive Gaussian noise (Ref. Section 4.3) in the system. In inverse, problem measured data set is available as $y(n)$ apart from either of $x_{true}(n)$ and $h(n)$ is known to calculate the other part [133]. This situation is presented in Fig. 6.14.

Determination of $x_{true}(n)$ from the knowledge of $y(n)$ and $h(n)$ is called inverse problem and determination of $h(n)$ from the knowledge of $x(n)$ and $y(n)$ is called system identification. In continuous form the system function $h(n)$ can be represented as integral operator as

$$\int_a^b h(s, n)x(n)dn = y(s) \quad (6.25)$$

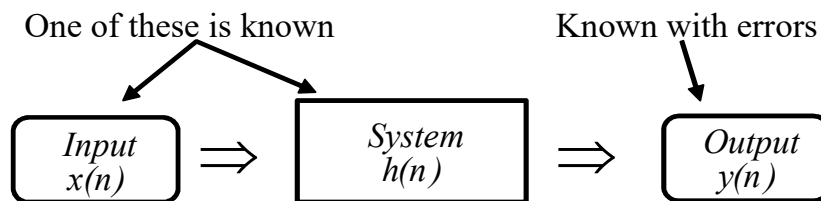


Figure 6.14: Inverse problem definition

Function $h(s, n)$ is called kernel and the system is linear as superposition and scaling can be applied as

$$\int_a^b h(s, n)(x_1(n) + x_2(n))dn = \int_a^b h(s, n)x_1(n)dn + \int_a^b h(s, n)x_2(n)dn$$

$$\text{And } \int_a^b h(s, n)\alpha x_1(n)dn = \alpha \int_a^b h(s, n)x_1(n)dn \quad (6.26)$$

Equations in the form of 6.26 where $x(n)$ is unknown are called **Fredholm integrals equations of the first kind (IFKs) [134]**. Key property of these equations is that it is difficult to obtain useful solution by straight forward methods. This equation arises from large number of inverse problems. In many cases kernel equation can be written to depend explicitly on $(s - n)$, which produces convolution equation:

$$\int_{-\infty}^{+\infty} h(s - n)x(n)dn = y(s) \quad (6.27)$$

Here interval of integration is extending from minus infinity to plus infinity, but other intervals can easily be accommodated by having $h(s - n) = 0$ outside of interval of interest. Forward problem of the type Equ. 6.27 for determining $y(s)$ from $x(n)$ is called convolution, and the inverse problem of determining $x(n)$ from $y(s)$ is called de-convolution.

Determination of solution of inverse problem requires solving system of inverse equation mathematically. It is important that the solution of the system of equation should not only mathematically acceptable, but also physically plausible and consistent with the system constrains. Important points to be considered while solving the problem are:

- (i) Existence: There may be no model that exactly fits the data. This can occur in practice because mathematical models of the systems are approximate or because data contains noise.
- (ii) Uniqueness: The exact solution to the problem may exist, but they are not unique, i.e. there are multiple solutions are available besides $x_{true}(n)$.

- (iii) **Instability:** Process of calculating inverse problem can be unstable as a small change in measurement can lead to enormous changes in the estimated model. Inverse problems where such situation arises are referred as *ill-posed problem*.

Inverse problems appear in several fields, including medical imaging, image processing, mathematical finance, astronomy, geophysics and nondestructive material testing. Typical inverse problems arise from asking simple questions "backwards". For instance, the simple question might be "If precisely the structure of the inner organs of a patient is known, what kind of X-ray images would be obtained from her?" The same question backwards is "Given a set of X-ray images of a patient, what is the three-dimensional structure of her inner organs?" This is the inverse problem of Computerized Tomography, or CT imaging. Usually the inverse problem is more difficult than the simple question that it reverses. Successful solution of inverse problems requires specially designed algorithms that can tolerate errors in measured data.

The problem defined as convolution sum as given in Equ. 6.27 that can be, in most general way, solved for input x_{true} from measured output y is using de-convolution, is given as:

$$\hat{X}_{true}(f) = \frac{Y(f)}{H(f)} = X_{true}(f) + \frac{D(f)}{H(f)} \quad (6.28)$$

Where $X_{true}(f)$, $Y(f)$, $H(f)$ and $D(f)$ are the Fourier pair of $x(n)$, $y(n)$, $h(f)$ and $d(n)$ respectively. $\hat{X}_{true}(f)$ is the estimate of the input signal calculated from the measured data $y(n)$ and system model $h(n)$. The second terms in the Equ. 6.28 is because of the noise present in the measurement. In most of the cases $H(f)$ is a low pass system containing very low values for the high frequency components. The de-convolution method to calculate $\hat{X}_{true}(f)$ is perfect but corrupted by the presence of noise. At high frequencies, where noise dominates, the presence of second term generates high frequency artefacts in the calculated

signal when direct solution is used to calculate inverse problem. This poses the challenge in calculating inverse system.

In next section, a solution is proposed to solve the inverse problem based on modified Wiener Filter. Wiener Filter [102 – 105, 135, 136] model is based on the minimization of least square error between filter output and desired signal. As mentioned earlier also, some of the main application areas for Wiener filter are linear prediction, echo cancellation, channel equalization, radar signal processing and system identification.

6.7 Modified Wiener Inverse Filter

In present section theory of Wiener Filter as de-convolution or inverse filter is presented. Apart from that the modification proposed to standard inverse filter is also presented. Schematic of the measurement system is displayed in Fig. 6.15. The output $y(n)$ of the system is written as:

$$y(n) = x(n) * h(n) + d(n) \quad (6.29a)$$

$$Y(f) = X(f).H(f) + D(f) \quad (6.29b)$$

Where, $y(n) \Leftrightarrow Y(f)$, $x(n) \Leftrightarrow X(f)$, $h(n) \Leftrightarrow H(f)$ and $d(n) \Leftrightarrow D(f)$ are the Fourier pair of the measured output, true input, system function and added noise independent of input signal. It is required to find out some filter such that:

$$\hat{x}(n) = y(n) * w(n) \quad (6.30a)$$

$$\hat{X}(f) = Y(f).W(f) \quad (6.30b)$$

Where, $\hat{x}(n) \Leftrightarrow \hat{X}(f)$ and $w(n) \Leftrightarrow W(f)$ are the Fourier pair of estimated input and inverse filter based on minimizing mean square error between estimated input and the true input. This method is based on the theory of Wiener filter and is supposed to take care of noise present in the system along with the system response. Let $\epsilon(f)$ is the error between estimated input $\hat{X}(f)$ and true input $X(f)$ which is presented as:

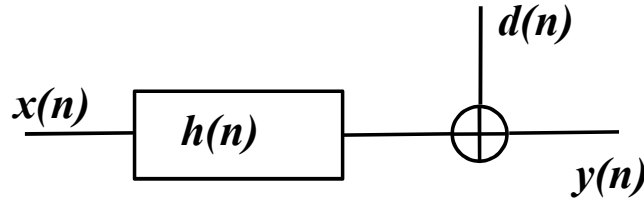


Figure 6.15: Measurement system with input $x(n)$, system function $h(n)$, additive measurement noise $d(n)$ and measured output with error $y(n)$.

$$\epsilon(f) = \mathbb{E} \left[\left(X(f) - \hat{X}(f) \right)^2 \right] \quad (6.31)$$

$$\epsilon(f) = \mathbb{E} [(X(f) - Y(f) \cdot W(f))^2]$$

$$\epsilon(f) = \mathbb{E} [(X(f) - (X(f) \cdot H(f) + D(f)) \cdot W(f))^2]$$

Rearranging gives

$$\epsilon(f) = \mathbb{E} \left[\left((1 - W(f)H(f))X(f) - W(f)D(f) \right)^2 \right]$$

Now expanding the quadratic term inside the expectation operator \mathbb{E} , and applying independence condition of noise and input signal results in:

$$\epsilon(f) = [1 - W(f)H(f)][1 - W(f)H(f)]^* P_{xx}(f) + W(f)W(f)^* P_{nn}(f) \quad (6.32)$$

Where $P_{xx}(f) = \mathbb{E}|X(f)|^2$ and $P_{nn}(f) = \mathbb{E}|D(f)|^2$ are the power spectrum of the input signal and additive noise respectively. To find out the minimum value of the mean square error $\epsilon(f)$ it is required to take derivative of Equ. 6.32 with respect to filter coefficients $W(f)$ and set it equal to zero. Then:

$$\frac{d\epsilon(f)}{dW(f)} = W^*(f)P_{nn}(f) - H(f)[1 - W(f)H(f)]^* P_{xx}(f) = 0 \quad (6.33)$$

Rearranging the above equation gives the filter coefficients in terms of system function and the desired input as:

$$W(f) = \frac{H^*(f)P_{xx}(f)}{|H(f)|^2 P_{xx}(f) + P_{nn}(f)} \quad (6.34)$$

In Equ. 6.34, $W(f)$ is the Fourier transform of the inverse filter for the system function, $H(f)$ and $P_{xx}(f)$ and $P_{nn}(f)$ is the power spectrum of required signal and noise, respectively. $W(f)$ is derived on the basis of minimization of mean square error as per the theory of Wiener filter [102, 130, 131, 135, 136]. This equation (Equ. 6.34) is called Wiener filter for de-convolution or Wiener system inverse filter (WIF). Equation 6.34 can be modified and rewritten as:

$$W(f) = \frac{1}{H(f)} \left[\frac{|H(f)|^2}{|H(f)|^2 + \frac{P_{nn}(f)}{P_{xx}(f)}} \right] \Rightarrow \frac{1}{H(f)} \left[\frac{|H(f)|^2}{|H(f)|^2 + \frac{1}{SNR(f)}} \right] \quad (6.35)$$

where $W(f)$ is the WIF coefficients, $H(f)$ is the system transfer function, $P_{nn}(f)$ and $P_{xx}(f)$ are the power spectrum of measured noise and input signal to be estimated. In Equ. 6.35, $1/H(f)$ is the inverse of the original system and $SNR = P_{xx}(f)/P_{nn}(f)$ is the signal to noise ratio. When there is no noise in the system, i.e. infinite SNR , the term inside the bracket become unity and Wiener filter work as simple inverse of the system. However, as noise increases, the term inside bracket decreases to less than unity and the filter coefficient for particular frequency drops i.e. filter attenuates frequency component depending on their signal to noise ratio. In all practical cases system transfer function and measured noise is either known or can be estimation based on the available information.

In present case system transfer function is the developed VISAR model and noise estimation can be obtained using measured signal during non active period as mentioned in Chapter 5. The remaining component for implementing WIF is $P_{xx}(f)$ which is calculated based on the available information as:

$$P_{xx}(f) = \mathbb{E}|X(f)|^2 \Rightarrow \mathbb{E} \left| \frac{Y(f)}{H(f)} \right|^2 \Rightarrow \frac{P_{yy}(f)}{|H(f) \cdot H^*(f)|} \Rightarrow \frac{P_{yy}(f)}{|H(f)|^2} \quad (6.36)$$

In above equation, the $P_{yy}(f)$ is the power spectrum density of the measured system output and $|H^2(f)|$ is the system transfer function of the VISAR. Replacing the new found value of input signal power spectrum in the Equ. 6.35 yields:

$$W(f) = \frac{1}{H(f)} \left[\frac{|H(f)|^2}{|H(f)|^2 + \frac{P_{nn}(f) \cdot |H(f)|^2}{P_{yy}(f)}} \right] \Rightarrow \frac{1}{H(f)} \left[\frac{1}{1 + \frac{P_{nn}(f)}{P_{yy}(f)}} \right] \quad (6.37)$$

This equation has two components, first one is the de-convolution part i.e. $1/H(f)$ and the second is the Wiener de-noising of the measured output signal i.e $Y(f)$. Hence, in WIF the de-noising of the measured signal is inherent part of the process and de-convolution of the obtained result is carried out using system transfer function. The modification carried out in the WIF is in its implementation. It is required to know the power spectrum of the unknown input signal for calculation of coefficients of WIF. By defining input power spectrum in terms of measured output signal $y(n)$ and system transfer function $h(n)$, (Equ. 6.36) the implementation of Wiener inverse filter become practical.

6.7.1 Implementation of Modified Inverse Filter

Two method of calculating inverse of a system response is presented in previous section 6.6. First one is the Wiener de-convolution (Equ. 6.35) and other is the modified inverse Wiener filter with the de-nosing carried out using filter (SSM+WF) proposed and developed in previous chapter 5. For comparison purpose, the de-convolution (equivalent to Equ. 6.28) with de-noising using Wiener filter (WF) as presented in Equ. 5.7 is also used. For simulation of these de-convolution methods and comparing their results, the input signal $x(n)$ (displacement profile) and system response $h(n)$ (VISAR model) has been selected and simulations were performed on the data sets for different level of noise assuming SNR's such as, 0dB, 10dB, 20dB, 30dB and 50dB. Noise in the system is added at the measurement of output data $y(n)$. Fig. 6.16 presents the data flow for the simulation. The three methods used

for de-convolution are also listed in the figure. Performance of the three filters namely, modified inverse WF, de-convolution with de-noising and Wiener de-convolution are measured in terms of the root mean square error (Equ. 5.15) present between actual input signal $x_{true}(n)$ and estimated input signal $\hat{x}(n)$. Figure 6.17, represent the variation of RMSE value for different SNR of the measured signal for three different de-convolution methods. It is clear that the modified inverse Wiener filter performs better as compared to other two methods. These results are encouraging and suggest that the modified inverse filter can be utilized for the determination of the displacement/velocity history of the target surface using two delay system methods in the VISAR.

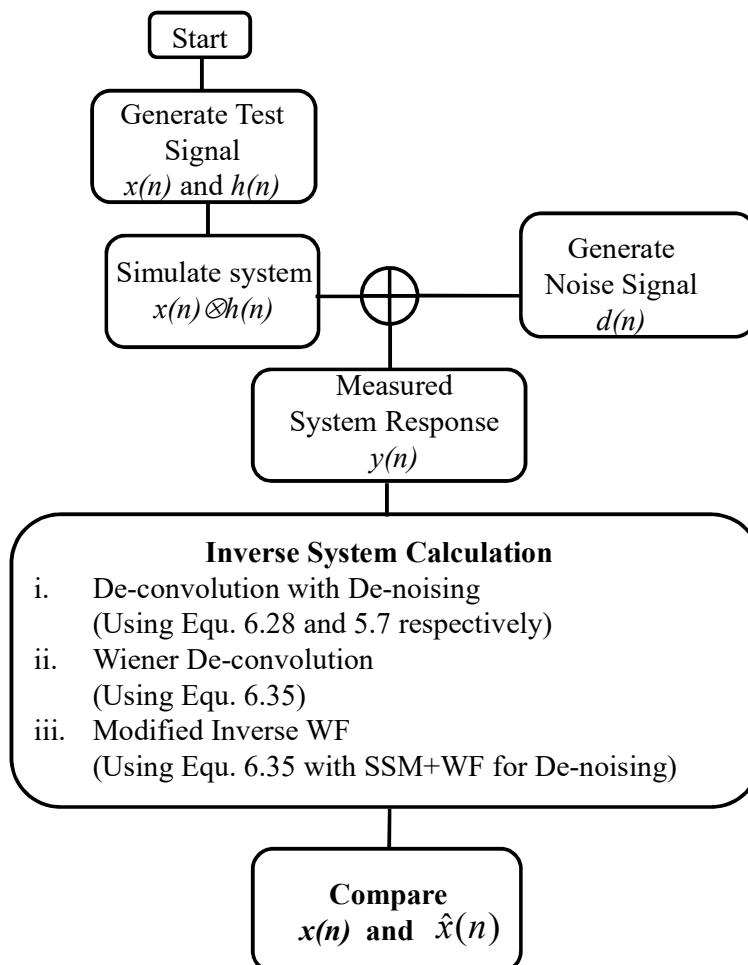


Figure 6.16: Proposed scheme for calculating inverse system response

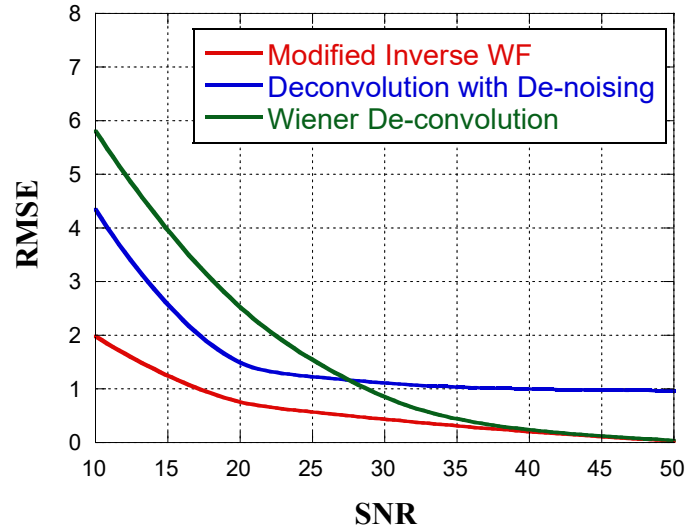


Figure 6.17: Root Mean Square Error presented for the comparison of the performance of three de-convolution method namely, Modified Inverse WF, Standard Wiener de-convolution and standard de-convolution applied after de-noising using the WF filter.

6.7.2 Two Delay VISAR Simulation

The results of the inverse filter implemented using Wiener method appear adequate enough to implement it for the determination of the displacement/velocity history of the target free surface in shock wave experiments employing two delay VISAR setup for overcoming the problem in long delay mode. For simulating the condition two delays (long delays) are selected and a velocity profile with rise time smaller than the two delays is created. For testing the VISAR approximation method one more delay (short delay) is selected. Response of VISAR instrument is obtained in terms of fringe signal using developed VISAR model. To simulate the actual measurement setup the noise equivalent to SNR value 35 dB is added to the generated fringe record.

Before performing the de-convolution, signals are de-noised using developed modified Wiener de-noising filter (Chapter 5). Now the VISAR approximation method as given in Equ. 6.1, is used to calculate velocity profile for all three delays. To test the performance of the proposed method of two independent long delay, the unwrapped phase obtained for two

long delay data is combined and modified inverse Wiener filter is applied. The schematic of the data and system flow is given in Fig. 6.18 (a) and (b). The obtained result of the system is the displacement history of the moving surface of the target, which is converted to velocity history by numerical differentiation as shown in Fig. 6.19. As is evident from the figure, the results for two independent long delays using VISAR approximation are significantly off from the actual input velocity profile, whereas, the same moves close to actual input profile when the procedure of estimating the velocity (modified inverse WF) is applied on the combined data of the two long delays. As far as the result of the VISAR approximation with short delay is concerned, it is able to represent input velocity faithfully.

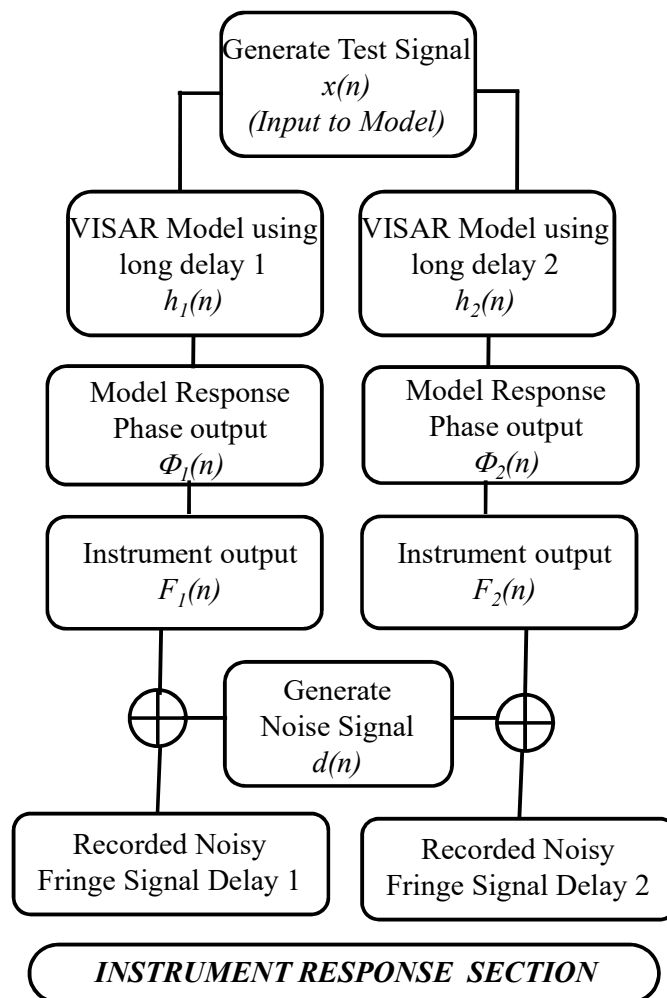


Figure 6.18(a): Steps for generating simulated VISAR response

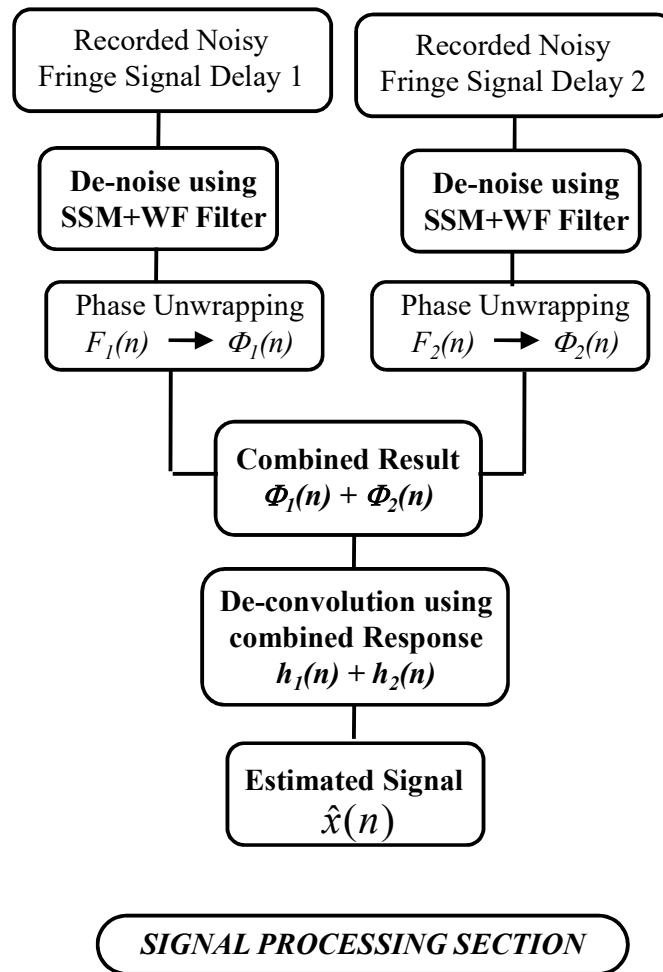


Figure 6.18(b): Signal processing steps for de-convolution

6.8 Summary

The LTI model of the VISAR has been developed to have deep insight of the response of the instrument. The first half of the chapter is dedicated for the development of the VISAR model and its characterization. Developed model response showed that the instrument delay which is the main component for the measurement of the differential Doppler shift puts restriction on the dynamic range of the instrument by placing periodic zeros at multiple of $1/\tau$ frequencies in the frequency response of the transfer function. To overcome the limitation of dynamic response due to instrument delay (τ), a method of two delay system has been

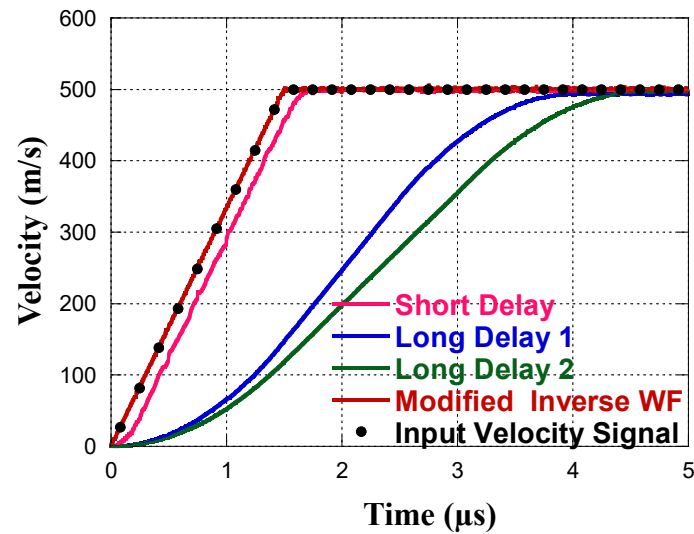


Figure 6.19: Comparison of estimated velocities using VISAR approximation method using one short delay and two long delay. Also presented is the estimated velocity using modified inverse WF by combining two long delay data along with input velocity signal.

proposed for displacing the zeros of the single delay system function by combining the result of the two independent instrument responses [116].

The analysis method to determine the displacement/velocity history of the free surface of the shock loaded target plate using proposed arrangement is developed using theory of inverse system. A de-convolution method based on the modified Wiener inverse filter is proposed and tested at different noise levels. Finally the proposed method is applied to the signals simulated for two different independent delays and displacement/velocity history of the system is estimated employing developed modified Wiener inverse filter (WIF). It is found that the proposed modified Wiener inverse method of de-convolution applied on the combined data of the two long delay VISAR systems produces the velocity history satisfactorily close to the actual (input) velocity history.



Chapter 7

Summary and Future Scope

Minimization of uncertainty in the measurement of physical parameters using different diagnostic techniques in dynamic compression experiments was the aim of present thesis work. The procedure adopted was to improve upon the complete measurement system used for determination of a physical parameter. The physical parameters include the shock temperature which is measured employing time resolved RP and free surface/particle velocity history which is measured using VISAR instrument. The complete measurement system for each of these physical parameters includes instrument design (system hardware including optics and electronics), data/signal processing (LTI modeling, de-noising etc.) and estimation methods (non linear curve fitting, linearity estimation, statistical methods etc). These parts of measurement system are interrelated and interconnected. Hence, to minimize the uncertainty of the measurement for above mentioned physical parameters, work has been done on all these parts.

For the measurement of shock temperature, the time resolved RP was developed. The hardware design of the instrument includes optical fiber based intensity collection system from the shocked target and beam splitter based wavelength selection optics. Si-PIN photodiode is used as the fast-sensitive detector for the selected spectral range. Other detectors that can be used are InGaAs and Mecerury Cadminum Teluloid (MCT) for low temperature measurement. The developed RP is systematically calibrated using NIST traceable calibration source. Temperature and emissivity estimation method is developed

based on the minimization of least square error by doing non linear curve fitting of measured radiance data points with the Planck's distribution. The uncertainty in temperature estimation from the measured radiance data using RP has been calculated to be within 5%. The error in estimation of emissivity was on the higher side and is because of the weak dependence of Planck's distribution on emissivity. It has been proposed in literature to use some functional form of emissivity (linear or quadratic) with dependence on temperature and wavelength to minimize the error in emissivity estimation. However, to get a meaningful functional form (linear or quadratic) the emissivity measurement is important. The emissivity is not only the bulk property of material, it also depends on the surface condition of the sample, hence it is difficult to measure the same. Innovative methods of in-situ emissivity measurement can be taken up as post thesis work for more accurate estimation of temperature and emissivity in dynamic compression experiments. With the improvement in the functional form of the emissivity, the estimation method of non linear least square is also required to be modified and updated based on the number of variables (parameters to be fitted) and number of equation to be solved (number of wavelength for measurement).

In case of VISAR instrument which is used for determination of free surface/particle velocity history by measuring time resolved Doppler shift, the overall accuracy of free surface/particle velocity measurement depends on the linearity of the measurement system. Work has been done to characterize the VISAR's SRS and determined the range of operation for which the deviation from linearity in PMT output is less than 5%. The procedure that we have adopted is generic and can be used for VISAR or any other measuring instrument using PMT as optical to electrical converter unit.

Most of the data reduction techniques (ellipse fitting, phase unwrapping etc.) to be applied on VISAR, require experimental fringe signal to be recorded with as high SNR as possible. But due to the constraint environment of experimental setup, the signals of 15-20 dB

SNR are generally obtained after recording. To further improve the SNR of signal a modified Wiener based de-noising filter has been developed as a part of present thesis work. This is an adaptive filter and modifies the filter coefficients based on the SNR of the input signal. A change in SNR of as high as 80% (from ~18 dB starting SNR to 33 dB final SNR) has been obtained after processing the raw experimental signals employing this filter. This modified Wiener filter generates one of the required estimates of signal power spectrum using SSM method. The possibility of employing wavelet shrinkage method or other innovative methods for generating such estimate for Wiener filter can be taken up as post thesis work.

Modeling of any instrument gives insight into its characteristics which under normal conditions may not be observable. To achieve such insight for VISAR instrument, the forward definition of VISAR (equation 6.2) is modeled as LTI system. This developed LIT system is characterized for its performance in time as well as frequency domain and validated with the experimental result. One of the important observation highlighted is that the response of VISAR instrument is not faithful when the rise time of velocity of moving target surface is of the order of instrument delay ' τ '. The use of normal VISAR approximation method under such experimental condition is not correct. The thesis has presented the method of solving such problem by using two delay VISAR. Also presented is one of the methods of combining the data of two delay system for determining the accurate velocity/displacement history of the target. The developed method is based on the solution of the inverse problem using modified inverse Wiener filter. Singular Value Decomposition (SVD) based inverse problem solution and predictive filter (Kalman and Particle filters) based techniques can be explored as post thesis work.



Appendix A: Relation between Target Free Surface Velocity and Fringe Count

Consider a simple displacement type Michelson interferometer in which mirror of one of the leg at time t acquires a velocity of $y(t)$. Then fringe frequency $f(t)$ and velocity $y(t)$ are related as:

$$y(t) = \frac{\lambda_0}{2} f(t) \quad (\text{A.1})$$

where λ_0 is the wavelength of the laser light. The fringe frequency $f(t)$ is the difference between the frequency $f_L(t)$ of the Doppler shifted light at time t and f_0 of the original light i.e. $f(t) = f_L(t) - f_0$. Now, unlike the displacement interferometer, the velocity interferometer uses the Doppler shifted lights at two different instants of time t and $(t-\tau)$, where τ is the delay introduced by the long leg. Therefore, fringe frequency produced by a velocity interferometer can be expressed as:

$$f_{v.i.}(t) = f_L(t) - f_L(t - \tau) \quad (\text{A.2})$$

Or

$$f_{v.i.}(t) = [f_L(t) - f_0] - [f_L(t - \tau) - f_0] \quad (\text{A.3})$$

Or

$$f_{v.i.}(t) = [f(t)] - [f(t - \tau)] \quad (\text{A.4})$$

The fringe count $F(T)$ is equal to the integral of the velocity interferometer fringe frequency up to time T . So,

$$F(T) = \int_0^T [f(t) - f(t - \tau)] dt \quad (\text{A.5})$$

Now it is assumed that $f(t) \equiv 0$ for $t < 0$, hence, Eq. A.5, reduces to

$$F(T) = \int_{T-\tau}^T f(t) dt \quad (\text{A.6})$$

Solving Eq. (A.1) for $f(t)$ and substituting in Eq. (A.6) gives

$$F(T) = \frac{2}{\lambda_0} \int_{T-\tau}^T y(t) dt \quad (\text{A.7})$$

Average value of $y(t)$ during the interval of integration i.e. delay in long leg, can be expressed as

$$\bar{y} = \frac{1}{\tau} \int_{T-\tau}^T y(t) dt \quad (\text{A.8})$$

Or

$$\int_{T-\tau}^T y(t) dt = \tau y\left(T - \frac{\tau}{2}\right) \quad (\text{A.9})$$

Substituting the Eq. (A.9) to Eq. (A.7) the expression for velocity of moving free surface becomes:

$$y\left(T - \frac{\tau}{2}\right) = \frac{\lambda_0}{2\tau} F(T) \quad \text{or} \quad y(T) = \frac{\lambda_0}{2\tau} F(T) \quad (\text{A.10})$$

The Eq. (A.10) is the equation of velocity interferometer where velocity upto time T is related to fringe count $F(T)$ upto time T .

Reference

- [1] T.R. Harrison and W.M.H. Wannamaker, “An Improved Radiation Pyrometer”, *Rev. Sci. Inst.*, **1941**, *12*, 20-32.
- [2] Alice M. Stoll and James D. Hardy, “Direct Experimental Comparison of Several Surface Temperature Measuring Devices”, *Rev. Sci. Inst.*, **1949**, *20(9)*, 678-686.
- [3] D.D. Bloomquist, G.E. Duvall and J.J. Dick, “Electrical Response of Bi-metallic Junction to Shock Compression”, *J. Appl. Phys.*, **1979**, *50*, 4838-4846.
- [4] Z. Rosenberg and Y. Partom, “Direct Measurement of Temperature in Shock Loaded Polymethylmetacrylate with Very Thin Copper Thermister”, in *Shock waves in Condensed Matter-1983*(edited by J.R. Asay et.al, Elsevier, Amsterdam, **1983**, 251.
- [5] J. W. Taylor, “Residual temperatures in shocked copper”, *J. Appl. Phys.*, **1963**, *34*, 2727-2731.
- [6] S.B. Kormer, “Optical study of the characteristics of shock-compressed dielectrics”, *Sov. Phys. Usp.*, **1965**, *21*, 689-700.
- [7] S.A. Raikes, T.J. Ahrens, “Postshock temperatures in minerals”, *Geophys. J. R. Astr. Soc.*, **1979**, *58*, 717-747.
- [8] H. Sugiura, K. Konda and A. Sawaoka, “Method for the measurement of temperature in shock compression of solids”, *Rev. Sci. Inst.*, **1980**, *51(6)*, 750-752.
- [9] M.B. Boslough and T.J. Ahrens, “A sensitive time-resolved radiation pyrometer for shock-temperature measurement above 1500K”, *Rev. Sci. Inst.*, **1989**, *60(12)*, 3711-3716.
- [10] N.C. Holmes, “Fiber-coupled optical pyrometer for shock-wave studies”, *Rev. Sci. Inst.*, **1995**, *66(3)*, 2615-2618.

-
- [11] A. S. Rav, A. K. Saxena, K. D. Joshi, T. C. Kaushik, and S. C. Gupta, "Time resolved radiation pyrometer for transient temperature measurement", *AIP Conf. Proc.*, **2011**, 1349, 451.
- [12] S.C. Gupta, S.G. Love and T.J. Ahrens, "Shock Temperature in Calcite (CaCO₃) at 95-160 GPa", *Earth and Planetary Science Lett.*, **2002**, 201(1), 1-12.
- [13] G.A. Lyzenga, T.J. Ahrens, W.J. Nellis and A.C. Mitchell, "The temperature of shock-compressed water", *J. Chem. Phys.*, **1982**, 76(12), 6282-6286.
- [14] G.A. Lyzenga & Thomas J. Ahrens, "Multiwavelength optical pyrometer for shock compression experiments", *Rev. Sci. Instrum.*, **1979**, 50(11), 1421.
- [15] H.B. Radousky & A.C. Mitchell, "A fast UV/visible pyrometer for shock temperature measurements to 20,000K", *Rev. Sci. Instrum.*, **1989**, 60(12), 3707.
- [16] Oleg V. Fat'yanov, Toshiyuki Ogura Malcom F. Nicol, Kazutaka G. Nakamura & Ken-ichi Kondo, "Time-resolved two-band infrared radiometry of carbon tetrachloride under shock compression up to 10 GPa", *Applied Physics Letters*, **2000**, 77(7), 960.
- [17] David Portouche-Sebban, David B. Holtkamp. R. Richard Bartsch, Huan Lee & Gerald G Schmitt, "Application of high speed, low temperature infrared pyrometer in pulsed power experiments", *Rev. Sci. Instrum.*, **2001**, 72(7), 3008.
- [18] D. Partouche-Sebban, D.B. Hotlkamp, J.L. Pelissier, J. Taboury, A. Rouyer, "An investigation of shock induced temperature rise and melting of bismuth using high speed optical pyrometry", *Shock Waves*, **2000**, 11, 385-392.
- [19] D. Partouche-Sebban & J.L. Pelissier, "Emissivity and temperature measurements under shock loading, along the melting curve of bismuth", *Shock Waves*, **2003**, 13, 69-81.
-

-
- [20] A. Seifter, M.R. Furlanetto, M. Grover, D.B. Holtkamp, G.S. Macrum, A.W. Obst, J.R. Payton, J.B. Stone, G.D. Stevens, D.C. Swift, L.J. Tabaka, W.D. Turley & L.R. Veerer, "Use of IR pyrometry to measure free-surface temperatures of partially melted tin as a function of shock pressure", *Journal of Applied Physics*, **2009**, *105*, 123526.
- [21] H.B. Radousky, M. Ross, A.C. Mitchell and W.J. Nellis, "Shock temperatures and melting in CsI", *Physical Review B*, **1985**, *31(3)*, 1457-1562.
- [22] H.B. Radousky, W.J. Nellis, M. Ross, D.C. Hamilton and A.C. Mitchell, "Molecular Dissociation and Shock-Induced Cooling in Fluid Nitrogen at High Densities and Temperatures", *Physical Review Letters*, **1986**, *57(19)*, 2419-2422.
- [23] D. Chengda, H. Jianho and T. Hua, "Hugoniot temperatures and melting of tantalum under shock compression determined by optical pyrometry", *Journal of Applied Physics*, **2009**, *106*, 043519-1-7.
- [24] L.M. Barker and R.E. Hollenbach, "Shock-Wave Studies of PMMA, Fused Silica and Sapphire", *Journal of Applied Physics*, **1970**, *41(10)*, 4208-4226.
- [25] L. Toller and R. Fabbro, "Study of the laser-driven spallation process by the VISAR interferometry technique. II. Experiment and simulation of the spallation process", *Journal of Applied Physics*, **1998**, *83*, 1231-1237.
- [26] T.J. Vaogler *et.al.*, "Using the line-VISAR to study multi-dimensional and mesoscale impact phenomena", *International Journal of Impact Engineering*, **2008**, *35*, 1844-1852.
- [27] L.M. Barker, R.E. Hollenbach, "Interferometer Technique for Measuring the Dynamic Mechanical Properties of Materials", *Rev. Sci. Inst.*, **1965**, *36*, 1617.
- [28] K.D. Joshi, Amit Rav and S.C. Gupta, "Development Velocity Interferometer System for Any Reflector for Measurement of Mechanical Properties of Materials During
-

-
- High Strain-Rate Compression and Decompression Process” *BARC/2011/E/002*.
http://www.iaea.org/inis/collection/NCLCollectionStore/_Public/42/091/42091173.pdf
- [29] K.D. Joshi, Amit Rav, Amit Sur, T.C. Kaushik and S.C. Gupta, “Spall fracture in aluminium alloy at high strain rates”, *AIP Conf. Procee.*, **2016**, *1713*, 060013
<http://dx.doi.org/10.1063/1.4947819> .
- [30] K.D. Joshi *et.al.*, “Mechanical properties of Shock Treated Aluminium Alloy Al2024-T4”, *Journal of Phy. Conf. Series*, **2012**, *377*, 012045.
- [31] L. Dubrovinsky *et.al.*, “The most incompressible metal osmium at static pressures above 750 gigapascals”, *Nature*, **2015**, *525*, 226.
- [32] R. Hawke, D. E. Duerre, J. G. Huebel, J. G. Klapper, D. J. Steinberg, and R. N. Keeler, “Method of isentropically compressing materials to several megabars,”, *J. Appl. Phys.* **1972**, *43*, 2734.
- [33] G. Wang, B. Luo, X. Zhang, J. Zhao, C. Sun, F. Tan, T. Chong, J. Mo, G. Wu and Y. Tao, “A 4 MA, 500 ns pulsed power generator CQ-4 for characterization of material behaviors under ramp wave loading,”, *Rev. Sci. Instrum.*, **2013**, *74*, 0151117.
- [34] N. Amadou, E. Brambrink, A. Benuzzi-Mounaix, T. Vinci, T. de Resseguier, S. Mazevet, G. Morard, F. Guyot, N. Ozaki, K. Miyanishi, and M. Koenig, “Laser-driven quasi-isentropic compression experiments and numerical studies of the iron alpha-epsilon transition in the context of planetology,”, *AIP Conf. Proc.*, **2012**, *1426*, 1525.
- [35] A. Ray and S. V. G. Menon, “Quasi-isentropic compression using functionally graded materials in gas gun and explosive driven systems,” *J. Appl. Phys.*, **2009**, *105*, 064501.
- [36] Lee Davison, “Fundamentals of shockwave propagation in solids”, *Springer Verlag*, **2008**, p. 38.
-

-
- [37] G.E. Duval and R.A. Graham, “Shock Waves in High Pressure Physics and Chemistry”, *Rev. of Modern Phys.*, **1977**, 49, 523.
- [38] M. B. Boslough and J. R. Asay, “Basic Principles of shock compression”, in: *High pressure shock compression of solids*, edited by J. R. Asay, and M. Shahinpoor, (Springer-Verlag Berlin Heidelberg Germany), **1992**, 36.
- [39] T. J. Ahrens, “Shock wave techniques for geophysics and planetary physics”, in: *Methods of experimental physics: Geophysics laboratory measurement*, (Academic Press Inc. Orlando Florida, 1987), **1987**, 185-233.
- [40] H. Mao, W. A. Bassett, and T. Takahashi, “Effect of pressure on crystal structure and lattice parameters of iron up to 300 kbar”, *J. Appl. Phys.*, **1967**, 28, 272.
- [41] R. A. Graham, “Solids under high pressure-shock compression: Mechanics physics and chemistry”, (Springer-Verlag NY, 1993), **1993**, Chap. 3, 55.
- [42] H. S. Yadav and N. K. Gupta, “Flyer plate motion and its deformation during flight”, *Int. J. Impact Engg.*, **1988**, 7, 71.
- [43] L. C. Chhabildas and M. D. Knudson, “Techniques to launch projectile plates to very high velocities”, in: *High pressure shock compression of solids VIII : The science and technology of high-velocity impact*, edited by L. C. Chhabildas, L. Davison, and Y. Horie, (Springer-Verlag Berlin Heidelberg Germany, 2005), **2005**, 143.
- [44] L. C. Chhabildas, L. N. Kmetyk, W. D. Reinhart, and C. A. Hall, “Enhanced hypervelocity launcher - capabilities to 16 km/s”, *Int. J. Impact. Engg.*, **1995**, 17, 183.
- [45] M. De Icaza, C. T. Renero, and F. E. Prieto, “Experimental facilities for impact physics research at the National University of Mexico”, *Physica B+C*, **1986**, 139, 599.
- [46] R. W. Lemke, M. D. Knudson, and J. P. Davis, “Magnetically driven hyper-velocity launch capability at the Sandia Z accelerator”, *Int. J. Impact Engg.*, **2011**, 38, 480.
-

-
- [47] R. A. Burden, J. W. Gray, and C. M. Oxley, "Explosive foil injection (EFI) pre-accelerator for electromagnetic launchers", *IEEE Trans. Magn.*, **1989**, 25, 107.
- [48] P. Lehmann, J. Wey, H. Mach, A. Eichhorn and K. Daree, "Study of a railgun plasma armature", *IEEE Trans. Plasma Sci.*, **1989**, 17, 371.
- [49] Y. Zhou, P. Yan, Y. Sun, W. Yuan, D. Zhang, and M. Li, "Design of a distributed energy store rail gun", *IEEE Trans. Plasma Sci.*, **2011**, 39, 230.
- [50] D. Wetz, F. Stefani, J. Parker, and I. McNab, "Development of a Plasma-Driven Railgun to Reach 7 km/s", *Proc. IEEE Int. Power Mod. and High Voltage Conf.* May **2008**, 85-88.
- [51] I. R. McNab, F. Stefani, M. Crawford, M. Erenkil, C. Persad, S. Satapathy, H. Vanicek, T. Watt, and C. Dampier, "Development of a naval rail gun", *IEEE Trans. Magn.*, **2005**, 41, 206.
- [52] I. T. Jr. Luke and M. F. Stumborg, "The operational value of long range land attack EM guns to future naval forces", *IEEE Trans. Magn.*, **2001**, 37, 58.
- [53] K.E. Froeschner, R. S. Lee, H. H. Chau and R. C. Weingart, "Performance of a 100 kV/ 78 kJ electric gun system", in: *Shock Waves in Condensed Matter: Proceedings of the American Physical Society, Topical Conference, Sante Fe, Mexico-July1983*, edited by J. R. Assay, R. A. Graham, and G. K. Straub, (North-Holland, Amsterdam, 1984), **1984**, 85.
- [54] J. E. Osher, H. H. Chau, G. R. Gathers, R. S. Lee, and R. C. Weingart, "Applications of a 100-kV electric gun for hypervelocity impact studies", *Int. J. Impact Engg.*, **1986**, 5, 501.
- [55] M. D. Knudson, "Megaamps, megagauss, and megabars: Using the Sandia Z Machine to perform extreme material dynamics experiments", *AIP Conf. Proc.*, **2012**, 1426, 35.
-

-
- [56] J-P Davis, C. Deeney, M. D. Knudson, R. W. Lemke, T. D. Pointon, and D. E. Bliss, “Magnetically driven isentropic compression to multimegabar pressures using shaped current pulses on the Z accelerator”, *Phys. Plasmas.*, **2005**, *12*, 056310.
- [57] I. Gilath, “Laser induced spallation and dynamic fracture at ultra high strain rate”, *in: High pressure shock compression of solids: Dynamic Fracture and Fragmentation*, edited by L. Davison, D. E. Grady and M. Shahinpoor, (Springer-Verlag NY, 1996), **1996**, 92.
- [58] L. R. Veerer and S. C. Solem, “Studies of laser-driven shock waves in aluminum”, *Phys. Rev. Lett.*, **1978**, *40*, 1391.
- [59] R. Cauble, D. W. Phillion, T. J. Hoover, N. C. Holmes, J. D. Kilkenny, and R. W. Lee, “Demonstration of 0.75Gbar planar shocks in X-ray driven colliding foils”, *Phys. Rev. Lett.*, **1993**, *70*, 2102.
- [60] S. Eliezer, J. J. Honrubia and G. Velarde, “Direct-indirect drive a new possibility for laser induced fusion”, *Phys. Lett. A*, **1992**, *166*, 249.
- [61] T. Mochizuki S. Sakabe and C. Yamanaka, “X-Ray Geometrical Smoothing Effect in Indirect X-Ray-Drive Implosion”, *Japan. J. Appl. Phys.*, **1983**, *22*, L124.
- [62] S. N. Luo, D. C. Swift, T. E. Tierney, D. L. Paisley, G. A. Kyrala, R. P. Johnson, A. A. Hauer, O. Tschauner, and P. D. Asimow, “Laser induced shock waves in condensed matter: some techniques and applications”, *High Press. Res.*, **2004**, *24*, 409.
- [63] N. A. Tahir, D. H. H. Hoffmann, A. Kozyreva, A. Shutov, J. A. Maruhn, U. Neuner, A. Tauschwitz, P. Spiller, and R. Bock, “Shock compression of condensed matter using intense beams of energetic heavy ions”, *Phys. Rev. E.*, **2000**, *61*, 1975.
- [64] D. H. H. Hoffmann, A. Blazevic, P. Ni, O. Rosmej, M. Roth, N. A. Tahir, A. Tauschwitz, S. Udrea, D. Varentsov, K. Weyrich, and Y. Maron, “Present and future
-

-
- perspectives for high energy density physics with intense heavy ion and laser beams”, *Laser Part. Beams*, **2005**, *23*, 47.
- [65] R. J. Wasley, J. F. O'Brien, and D. R. Henley, “Design and construction of a new coaxial electrical discharge pin”, *Rev. Sci. Instrum.*, **1964**, *35*, 466.
- [66] Amit S. Rav, K.D. Joshi and Satish C Gupta, “Ionization pin arrival transducer for dynamic pressure experiments”, *12th National seminar on Physics and technology of Sensors*, **2007**, 134.
- [67] R. F. Benjamin and F. J. Mayer, “Applications of the microshell-tipped optical fiber”, *Optical Fiber Sensors, (Optical Society of America, 1985)*, **1985**, ThFF4.
- [68] L. M. Barker, M. Shahinpoor and L. C. Chhabildas, “Experimental and diagnostic techniques”, in: *High pressure shock compression of solids, edited by J. R. Asay, and M. Shahinpoor, (Springer-Verlag Berlin Heidelberg Germany, 1992)*, **1992**, 55.
- [69] G. Yiannakopoulos, “A review of Manganin gauge technology for measurements in gigapascal range”, *MRL Technical Report No. MRL-1990TR-90-5*.
- [70] C. S. Lynch, “Strain compensated thin film stress gauges for stress wave measurements in the presence of lateral strain,” *Rev. Sci. Instrum.*, **1995**, *66*, 5582.
- [71] F. Bauer, “PVDF gauge piezoelectric response under two-stage light gas gun impact loading”, *AIP Conf. Proc.* **2002**, *620*, 1149.
- [72] F. Bauer, “PVF2 polymers: Ferroelectric polarization and piezoelectric properties under dynamic pressure and shock wave action”, *Ferroelectrics*, **1983**, *49*, 231.
- [73] L. M. Barker and R. E. Hollenbach, “Laser interferometer for measuring high velocities of any reflecting surface”, *J. Appl. Phys.*, **1972**, *43*, 4669.
- [74] P. M. Johnson and T. J. Burgess, “Free surface velocity measurement of an impacted projectile by optical Doppler shift”, *Rev. Sci. Instrum.*, **1986**, *39*, 1100.
-

-
- [75] L. M. Barker, "The accuracy of visar instrument", *AIP Conference Proceedings of Shock Compression of Condensed Matter*, **1998**, 429, 833-836.
- [76] R. L. Hilliard and C. G. Shepherd, "Wide Angle Michelson Interferometer for measuring Doppler line width", *J. Opt. Soc. Am.*, **1966**, 56, 362.
- [77] G. M. B. Bouricious and S. F. Clifford, "An optical interferometer using polarization coding to obtain quadrature phase components", *Rev. Sci. Instrum.*, **1970**, 41, 1800.
- [78] W. F. Hemsing, "Velocity sensing interferometer (VISAR) modification", *Rev. Sci. Instrum.*, **1979**, 50(1), 73.
- [79] D. D. Bloomquist and S. A. Sheffield, "Optically recording interferometer for velocity measurement with subnanosec resolution", *J. Appl. Phys.*, **1983**, 54, 1717.
- [80] P. M. Johnson and T. J. Burgess, "Free surface velocity measurement of an impacted projectile by optical Doppler shift", *Rev. Sci. Instrum.*, **1968**, 39, 1100.
- [81] M. Durand, P. Laharrague, P. Lalle, A. Le Bihan, J. Morvan and H. Pujols, "Interferometric laser technique for accurate velocity measurement in shock wave physics", *Rev. Sci. Instrum.*, **1977**, 48, 275.
- [82] C. F. McMillan, D. R. Goosman, N. L. Parker, L. L. Steinmetz, H. H. Chau, T. Huen, R. K. Whipkey, and S. J. Perry, "Velocimetry of fast surfaces using Fabry-Perot interferometer", *Rev. Sci. Instrum.*, **1988**, 59(1).
- [83] W. L. Seitz and H. L. Stacy, "Fabry-Perot interferometry using an image intensified rotating mirror streak camera", *Proc. of High Speed Photography, Videography & Photonics, Soc. Photo Opt. Instrum. Eng.*, **1983**, 427, 186.
- [84] J. Weng, H. Tan, S. Hu, Y. Ma and X. Wang, "New all fiber velocimeter", *Rev. Sci. Instrum.*, **2005**, 76, 093301.

-
- [85] O. T. Strand, D. R. Goosman, C. Martinez, T. L. Whitworth, and W. W. Kuhlow, “Compact system for high-speed velocimetry using heterodyne techniques”, *Rev. Sci. Instrum.*, **2006**, *77*, 083108.
- [86] J. Weng, X. Wang, Y. Ma, H. Tan, L. Cai, J. Li, and C. Liu “A compact all-fiber displacement interferometer for measuring the foil velocity driven by laser”, , *Rev. Sci. Instrum.*, **2008**, *79*, 113101.
- [87] W. M. Isbell, “Historical overview of hypervelocity impact diagnostic technology”, *Int. J. Impact Engng.*, **1987**, *5*, 389.
- [88] D. H. Kalantar et al., “Direct observation of the α - ϵ transition in shock-compressed iron via nanosecond X-ray diffraction”, *Phys. Rev. Lett.*, **2005**, *95*, 075502.
- [89] S. A. Sheffield, R. L. Gustavsen and R. R. Alcon, “In-situ magnetic gauging technique used at LANL - method and shock information obtained”, *AIP Conf. Proc.*, **2000**, *505*, 1043.
- [90] A. Fenster, J.C. Leblanc, W.B. Taylor and H.E. Johns, “Linearity and Fatigue in Photomultipliers”, *Rev. Sci. Instrum.*, **1973**, *44*, 689-694.
- [91] D.H. Hartman, “Pulse Mode Saturation Properties of Photomultiplier Tubes”, *Rev. Sci. Instrum.*, **1978**, *49*, 1130-1133.
- [92] P.L. Land, “A Discussion of the Region of Linear Operation of Photomultipliers”, *Rev. Sci. Instrum.*, **1971**, *42*, 420-425.
- [93] P.B. Coates, “The Origin of Afterpulses in Photomultipliers”, *J.Phys. D: Appl. Phys.*, **1973**, *6*, 1159-1166.
- [94] R.J. Riley and A.G. Wright, “The Effect of Photomultiplier Afterpulse in Coincidence System”, *J. Phys. E.*, **1977**, *10*, 873-874.
- [95] A.K. Tripathi, S. Akhanjee, K. Arisaka, D. Barnhill, C. D’Pasquale, C. Jillings, T. Ohnuki, and P. Ranin, “A systematic study of large PMTs for the Pierre Auger

-
- Observatory”, *Nuclear Instruments and Methods in Physics Research A*, **2003**, 497, 331-339.
- [96] S.J. Brice *et.al.*, “Photomultiplier tubes in the MiniBooNE experiment”, *Nuclear Instruments and Methods in Physics Research A*, **2006**, 562, 97-109,
- [97] R. Abbasi *et.al.*, “Calibration and characterization of the IceCube photomultiplier tube”, *Nuclear Instruments and Methods in Physics Research A*, **2010**, 618, 139-152.
- [98] Kazuyoshi Itoh, “Analysis of the phase unwrapping algorithm”, *Applied Optics*, **1982**, 21(14), 2470.
- [99] A. Sur, A. S. Rav, K. D. Joshi, S. C. Gupta and K. Roy, “Fringe analysis software: Application to velocity measurement in dynamic compression experiment”, *Annual IEEE India Conference (INDICON)* 10.1109/INDICON.2014.7030619, **2014**, pp. 1-6.
- [100] Tarun Kumar Gangopadhyay, Sivaji Chakravorti, Kesab Bhattacharya and Saibal Chatterjee, “Wavelet analysis of optical signal extracted from a non-contact fibre-optic vibration sensor using an extrinsic Fabry–Perot interferometer”, *IOP Meas. Sci. Technol.*, **2005**, 16, 1075–1082.
- [101] L. Ying, “Phase unwrapping”, In *M. Akay (Ed.), Wiley encyclopedia of biomedical engineering*. New York: Wiley. **2006** DOI: 10.1002/9780471740360.ebs1356.
- [102] S. V. Vaseghi, “Least Square Error Wiener-Kolmogorov Filters”, in *Advanced Digital Signal Processing and Noise Reduction 4th Edition*, John Wiley & Sons Ltd., **2008**, pp. 173-191.
- [103] H. Furuya, S. Eda and T. Shimamura, “Image Restoration via Wiener Filtering in the Frequency Domain”, *WSEAS Transaction on Signal Processing*, **2009**, 5(2), 63-73.
- [104] S. Suhaila and T. Shimamura, “Frequency domain Wiener filter for image denoising: Derivation of a new power spectrum estimation method”, *Journal of Signal Processing*, **2012**, 16(1), 79-85.
-

-
- [105] H. Choi and R. Baraniuk, "Analysis of Wavelet-Domain Wiener Filter", in *Int. Symp. Time-Freq. and Time-Scale Analysis*, **1998**, 613-615.
- [106] P. Moulin, "Wavelet Thresholding Techniques for Power Spectrum Estimation", *IEEE Transaction on Signal Processing*, **1994**, 42(11), 3126-3236.
- [107] P. Sisal, "Wiener Filter ring with Spectrum Estimation by Wavelet Transformation", in *Int. Conf. on Tern. In Comm.*, **2001**, 2, 471-474.
- [108] M. Kazubek, "Wavelet Domain Image Denoising by Thresholding and Wiener Filtering", *IEEE Signal Processing Letter*, **2003**, 10(11), 324-326.
- [109] J. S. Lim, "Image Restoration by Short Space Spectral Subtraction", *IEEE Transaction on Acoustics, Speech and Signal Processing*, **1980**, 28(2), 191-197.
- [110] A. R. Fukane and S. Sahare, "Different Approaches of Spectral Subtraction Method for Enhancing the Speech Signal in Noisy Environments", *International Journal of Scientific and Engineering Research*, **2011**, 2(5), 119-124.
- [111] E. Verteletskaya and B. Simrak, "Noise Reduction Based on Modified Spectral Subtraction Method", *International Journal of Computer Science*, **2011**, 38(1), 82-88.
- [112] M. Berouti and R. Schwartz, J. Makhoul, "Enhancement of Speech Corrupted by Acoustic Noise", in *Proc. ICASSP*, **1979**, 208-211.
- [113] S. F. Boll, "Suppression of Acoustic Noise in Speech using Spectral Subtraction", in *IEEE Int. Conf. on Acou., Speech, and Signal Proc.*, **1979**, 208-211.
- [114] L.M. Barker, "Velocity Interferometer Data Reduction", *Rev. Sci. Instrm.*, **1971**, 42(2), 276.
- [115] D.H. Dolan, "Foundations of VISAR analysis", *Sandia Report*, **2006**, SAND2006-1950.

-
- [116] D. J. Erskine, “Recovering a Short Timescale Signal from a Pair of Long-Delay VISARS”, *APS Shock Comprsn. Cndsnd. Matter Chicago, IL, United States*, **2011**, *LLNL-PROC-486471*.
- [117] Jacob Fraden, “Thermometers; Measurements, Instruments and Sensors Handbook”, *Infrared* edited by *John G. Webster, CRCnetBase* **1999**.
- [118] J.M. Walsh and R.H. Christian, “Equation of State of Metals from Shock Wave Measurements”, *Phys. Rev.*, **1955**, *97*, 1544-1556.
- [119] S.C. Chapra & R.P. Canale, “Numerical Methods for Engineers”, *Fouth Edition, Tata McGraw-Hill Edition*.
- [120] M.I.A. Lourakis, “A brief description of the Levenberg-Marquardt algorithm implemented by levmar”, *Technical Report. Institute of Computer Science, Foundation for Research and Technology - Hellas*, **2005**.
- [121] K. Madsen, N.B. Nielsen, and O. Tingleff, “Methods for nonlinear least squares problems”, *Technical Report. Informatics and Mathematical Modeling, Technical University of Denmark*, **2004**.
- [122] D.W. Marquardt, “An algorithm for least-squares estimation of nonlinear parameters”, *Journal of the Society for Industrial and Applied Mathematics*, **1963**, *11(2)*, 431-441.
- [123] A. Grinenko, Ya. E. Krasik, S. Eflmov, A. Fedotov, V.Tz. Gurovich and V.I. Oreshkin, “Nanosecond time scale, high power electrical wire explosion in water”, *Physics of Plasmas*, **2006**, *13*, 042701-14.
- [124] Amit Rav, K.D. Joshi, Kallol Roy and T.C. Kaushik, “Velocity Interferometer signal de-noising using modified Wiener filter”, *Meas. Sci. Technol.* **2017**, *28(5)*, <https://doi.org/10.1088/1361-6501/aa5d49>.
-

-
- [125] S. V. Vaseghi, "Signal Enhancement via Spectral Amplitude Estimation", in *Advanced Digital Signal Processing and Noise Reduction 4th Edition*, John Wiley & Sons Ltd., **2008**, 321-339.
- [126] N. Niklolaev, Z. Nikolov, A. Gotchev and K. Egiazarian, "ECG Signal De-noising using Wavelet Domain Wiener Filtering", in *IEEE Int. Conf. on Acou., Spee. and Sig. Proces.*, **2000**, 6, 3578-3581.
- [127] D. L. Donoho and J. M. Johnstone, *Biometrika*, "Ideal Spatial adaptation by Wavelet Shrinkage", **1994**, 81(3), 425-455.
- [128] D. L. Donoho and J. M. Johnstone, "Adapting to unknown smoothness via wavelet shrinkage", *JASA*, **1995**, 90(432), 1200-1224.
- [129] Roman Frigg and Julian Reiss, "The philosophy of simulation: hot new issues or same old stew?", *Synthese*, **2009**, vol. 169, 593-613.
- [130] S.W. Smith, "The Scientist and Engineer's Guide to Digital Signal Processing", *2nd edition*, **1999**.
- [131] J.G. Proakis and D.M. Manolakis, "Digital Signal Processing: Principles, Algorithms, and Applications", *3rd edition*, **2000**.
- [132] "Measuring Signal Similarities", *MathWorks Document Center*.
- [133] P C Hansen, "Discrete Inverse Problem: Insight and Algorithms", *ISBN-13: 978-0898716962*.
- [134] Richard C. Aster, Brian Borchers, and Clifford H. Thurber, "Parameter Estimation and Inverse Problems", *ISBN: 0-12-065604-3*.
- [135] Maule M and A. L. Beling da Rosa, "Wiener Filter Applied to De-convolution" *Universidade Federal do Rio Grande do Sul, Porto Alegre, Brazil*, **2011**.
- [136] E. Sekko, G. Thomas and A. Boukrouche, "A deconvolution technique using optimal Wiener filtering and regularization", *Elsevier Signal Processing*, 72, **1999**, 23-32.
-